Investigation Of Static And Dynamic Magnetic Properties Of Two-Dimensional Magnonic Crystals

THESIS SUBMITTED FOR THE DEGREE OF
DOCTOR OF PHILOSOPHY (SCIENCE)
IN

NANO SCIENCE

BY
RUMA MANDAL

CENTRE FOR RESEARCH IN NANOSCIENCE AND NANOTECHNOLOGY
UNIVERSITY OF CALCUTTA
2015

Dedicated to…

Baba and Maa

Acknowledgements

The final outcome of this thesis received a lot of guidance and assistance from many people and I am extremely fortunate to have got these all along the completion of my Ph.D. *study. There is too little room to accommodate all of you on this piece of paper, but be sure that there is always room in my heart and in my memory to cherish all those gold strings of bright moments that will be connecting us forever.*

First and foremost, I would like to express my great admiration and gratitude to my supervisor, ***Prof. Anjan Barman*** *for his precious teachings, guidance, personal dedication and the many interesting discussions, which have been of great help to me and also for his strong support in every moment of my research activity in these years. One fine morning I received one email from him allowing me to pursue* Ph.D. *under his supervision. From that very beginning he provided me unflinching encouragement and support in various ways. Working in his laboratory was a pleasant experience and I will forever cherish the valuable time I have spent with him. Prof. Barman taught me that every mistake is a learning opportunity, and I am grateful to him for his patience and encouragement as I made my way slowly up to the learning curve in the lab. He has an excellent sense of humor and it was a pleasure to talk to him about any random topic, Physics or not. I have learned enormous things from my supervisor. I hope that this is only the starting point of my future career. Thank you, Sir, for giving me the privilege to work in your research lab.*

I would like to express my deepest gratitude to Prof. Arup Kumar Roychaudhuri, Department of Condensed Matter Physics and Material Sciences, S. N. Bose National Center for Basic Sciences for his kind support that he provided during the course of this research work. I convey my sincere gratitude to Professor Yoshichika Otani, University of Tokyo for accommodating me in his laboratory at RIKEN, Japan as a Visiting Technician. These collaborative visits gave me enough opportunity to develop scientific skills as well as mental strength to fight against failures. I am also grateful to Dr. Saswati Barman who taught me the LLG Micromagnetic Simulator and helped me a lot in the simulation works. I would like to thank Dr. Kaustuv Das who helped me during sample fabrication using Focused Ion Beam Lithography. I would like to

acknowledge my project supervisor Prof. Shyamal Kr. Bhadra and M.Sc. project supervisor Prof. Indra Dasgupta for their inspirations that guided me to choose basic scientific research as my career.

I am also grateful to all my respected teachers involved throughout my academic career for their proper guidance and influential teaching which helped me to achieve my goals. Specially, I should mention about my most favourite Physics teacher, Mr. Ashoktaru Biswas who developed my interest in physics.

Special thanks go to my great lab colleagues who helped me to continue my research in a friendly atmosphere. I started my learning process, from experimental work to lab duties, at the very first day of my Ph.D. *study from one of my dearest colleagues Bivas. I am also thankful to Dheeraj for developing the Dotmag software. I relished the time spent with Sabareesan Da, Feroz Da, Rabindranath Da, Pinaki Da, Arabinda Da, Jaivardhan Da, Semanti, Milan, Bipul, Susmita, Arnab, Debanjan, Kallol, Chandrima, Samiran, Kaushik, Sucheta, Santanu, Nikita, Anita, Avinash, Neeraj, Sourabh and Neha.*

During my Ph.D. *I have spent some quality time with some of my good friends, Mahasweta Di, Sanghamitra Di, Abhinav Bhaiya, Rajiv Bhaiya, Ruma, Saikat, Basudev, Sishir, Soma, Anuradha and Tamisra who helped me to tackle all the difficulties, stood beside me and gave all kinds of support. I am sure there are some I may have missed, but they are no less appreciated!*

I would like to acknowledge all the office, administration and technical staffs of S.N.B.N.C.B.S. for their kind help.

The person who encouraged me to enter in this field and understood all my problems from both personal and scientific point of views is my husband Dr. Arghya Dutta. He is the only person with whom I can argue on personal and as well as on scientific issues. He stood beside me during every ups and downs of my life during my Ph.D.. *Without his mental support this work would not have been completed.*

Last, but not the least, I thank my parents for the great gift of life in this beautiful world full of so nice things and challenging tasks. I will forever remain indebted to their unconditional love, encouragement and support to pursue my interests. The

toughest time came when I lost my father while I was taking care of our collaborative research work in Japan. The biggest loss, which can never be compensated, made me more determined to achieve my goal and to fulfill my father's dream. My mother is like a big banyan tree where I can take shelter at every moment in my life. Thanks to my two cute and sweet elder sisters acting as teacher, friend and guide since my childhood. I would like to thank the two junior most members of our family Papa and Tubu for their love and blind support. I convey my gratitude to my father-in-law, mother-in-law, all other relatives in-laws' house and late grand parents for their belief in me, endless encouragements and well wishes. I gratefully acknowledge my parents and other family members for their encouragement, support and sacrifice for making my research possible.

I gratefully acknowledge Department of Science and Technology and Japan Science and Technology Agency Strategic International Cooperative Program for giving the financial assistance as well as Satyendra Nath Bose National Centre for Basic Sciences for providing me this platform to accomplish my work.

Ruma Mandal
S. N. Bose National Centre for Basic Sciences
Salt Lake, Kolkata, India.

List of Publications

Papers Included in this Thesis

1. Optically Induced Tunable Magnetization Dynamics in Nanoscale Co Antidot Lattices
   R. Mandal, S. Saha, D. Kumar, S. Barman, S. Pal, K. Das, A. K. Raychaudhuri, Y. Fukuma, Y. Otani and A. Barman
   ACS Nano **6**, 3397 (2012)

2. Effect of Antidot Shape on the Spin Wave Spectra of Two-Dimensional $Ni_{80}Fe_{20}$ Antidot Lattices
   R. Mandal, P. Laha, K. Das, S. Saha, S. Barman, A. K. Raychaudhuri and A. Barman
   Appl. Phys. Lett. **103**, 262410 (2013)

3. Tunable Spin Wave Spectra in Two-Dimensional $Ni_{80}Fe_{20}$ Antidot Lattices with Varying Lattice Symmetry
   R. Mandal, S. Barman, S. Saha, Y. Otani and A. Barman
   *J. App. Phys. (*Accepted)

Papers Not Included in this Thesis

1. Tunable Configurational Anisotropy in Collective Magnetization Dynamics of $Ni_{80}Fe_{20}$ Nanodot Arrays with Varying Dot Shapes
   B. K. Mahato, S. Choudhury, **R. Mandal**, S. Barman, Y. Otani and A. Barman
   J. App. Phys. **117**, 213909 (2015)

2. Tunable Magnonic Spectra in Two-Dimensional Magnonic Crystals with Variable Lattice Symmetry
   S. Saha, **R. Mandal**, S. Barman, D. Kumar, B. Rana, Y. Fukuma, S. Sugimoto, Y. Otani and A. Barman
   Adv. Funct. Mater. **23**, 2378 (2013)

3. Configurational Anisotropic Spin Waves in Cross-Shaped $Ni_{80}Fe_{20}$ Nanoelements
   B. K. Mahato, B. Rana, **R. Mandal**, D. Kumar, S. Barman, Y. Fukuma, Y. Otani and A. Barman
   Appl. Phys. Lett. **102**, 192402 (2013)

4. Time-resolved Measurement of Spin Wave Spectra in CoO capped $[Co(t)/Pt(7Å)]_{n-1}$ Co(t) multilayer systems
   S. Pal, B. Rana, S. Saha, **R. Mandal**, O. Hellwig, J. Romero-Vivas, S. Mamica, J. W. Klos, M. Mruczkiewicz, M. L. Sokolovskyy, M. Krawczyk and A. Barman
   J. App. Phys. **111**, 07C507 (2012)

5. Anisotropy in Collective Precessional Dynamics in Arrays of $Ni_{80}Fe_{20}$ Nanoelements
   B. Rana, D. Kumar, S. Barman, S. Pal, **R. Mandal**, Y. Fukuma, Y. Otani, S. Sugimoto and A. Barman
   J. Appl. Phys. **111**, 07D503 (2012)

ABSTRACT

Periodically arranged nanomagnets are important candidates for modern and future technologies based on magnetism including nonvolatile magnetic memory, magnetic data storage, magnetic recording heads, spin logic devices, spin torque nano-oscillators and magnonic crystals. Magnonic crystals are spatially modulated patterned magnetic media acting as a medium for propagation of spin waves. Those crystals are analogous to photonic or phononic crystals but work in the microwave regime. Among different kinds of magnonic crystals ferromagnetic antidot lattices are most promising as these are exchange coupled continuous magnetic medium with periodic arrangement of antidots (holes) and have larger propagation velocity (steeper dispersion) than ferromagnetic dot lattices.

We have studied the dynamic magnetic properties of lithographically patterned two dimensional anitdot lattices. The ultrafast magnetization dynamics is studied by an all-optical time-resolved magneto-optical Kerr effect microscope with collinear pump-probe geometry. The ferromagnetic resonance in frequency domain is studied by broadband ferromagnetic resonance spectrometer based on a vector network analyzer. The experimental results are explained with the aid of numerical micromagnetic simulations.

We have fabricated arrays of finite blanket Co or $Ni_{80}Fe_{20}$ thin films using a combination of photolithography and electron beam evaporation techniques. The thickness/width ratio of these films are very low so that the edge demagnetization effect is negligible. The time-domain magnetization dynamics of the thin films show a single resonant mode of uniform precessional dynamics. With the aid of focused ion beam lithography we fabricated high quality square arrays of Co antidots of antidot diameter 100 nm and varying lattice constants (S) from 200 to 500 nm. For the sparsest lattice, we observed two bands of precessional modes with a band gap, which increases substantially with the decrease in lattice constant down to 300 nm. At S = 200 nm, four distinct bands with significant band gap appear. The numerically calculated mode profiles show various localized and extended modes with the propagation direction perpendicular to the bias magnetic

field. We have numerically demonstrated some composite antidot structures with very rich magnonic spectra spreading between 3 and 27 GHz based upon the above experimental observation.

We further demonstrate that optically induced spin wave spectra of nanoscale $Ni_{80}Fe_{20}$ antidot lattices can be tuned by changing the antidot shape. The spin wave spectra also show an anisotropy with the variation of the in-plane bias field orientation. Analyses show this is due to various quantized and extended modes, whose nature changes with the antidot shape and bias field orientation as a result of the variation of the internal magnetic field profile. We further studied the effect of lattice symmetry on the spin wave dynamics in two-dimensional nanoscale $Ni_{80}Fe_{20}$ antidot lattices by using a broadband ferromagnetic resonance technique. The experimental and simulation results show distinct differences in the frequencies and spatial nature of the resonant modes. For square and rectangular lattices extended spin wave mode appears in addition to standing spin wave modes. But for hexagonal, honeycomb and octagonal lattices all modes are either localized or standing waves. In addition, the honeycomb and octagonal lattices showed two different types of modes confined within the honeycomb (octagonal) units and between two such consecutive units. Simulated internal magnetic fields confirm the origin of such a wide variation in the frequency and spatial nature of the spin wave modes.

The tunability of spin waves with the variation of lattice constant, shape of antidots and lattice symmetry and also the anisotropic behavior of spin waves in two-dimensional antidot lattices are important for the design of future magnetic data storage and magnonic devices.

List of Contents

List of Figures

List of Tables

List of symbols

α	: Damping constant
γ	: Gyromagnetic ratio
λ	: Wavelength
τ	: Time constant
M	: Magnetization
M_s	: Saturation magnetization
H_{ext}	: Applied bias magnetic field
H_{eff}	: Effective magnetic field
H_k	: Anisotropy field
A	: Exchange stiffness constant
f	: Frequency

Chapter 1

Introduction

Magnetism is a very well known and old fundamental research topic of science. It was invented due to the human curiosity back in about 600 BC[1]. From the early stage of its discovery, magnetism has benefited the human society starting from its use in surgery to the use of compass for navigation. Over a long period of time from electromagnetic industry to miniaturized solid state devices, magnetism initiated the discovery of many fundamental phenomena and took an important role in modern science and technology. From nineteenth century, modern magnetism originated with some pioneering contributions by Oersted, Ampere, Gauss, Biot-Savart, Faraday and Lorentz. Now-a-days, a new topic of research known as "nanomagnetism" has emerged based on the discovery of new nanoscale magnetic materials coupled with new ideas and new technologies. The growing interest in nanomagnetism is due to its huge acceptability in modern and future technologies. Nanomagnetism can play an important role in different multidisciplinary branches of applications such as magnetic data storage[2-4], nonvolatile magnetic memory[5-7], magnetic logic[8-12], magnetic resonance imaging[13], magnetic recording heads[14], magnonics[15-18], microwave communication[19-21], biomedicine and biotechnology[22, 23].

In the year of 1900, Danish engineer Valdemar Poulsen[24] first demonstrated the principle of magnetic recording. Then the researchers in IBM, in 1956, first developed the magnetic data storage device with storage capacity of 5 MB. Now in modern disk drives, the storage capacity has increased by more than 20 million-fold in the quest to increase the storage density and to reduce the market cost. Conventionally, longitudinal media such as a thin single layered granular film was used for recording device by the industry for five decades. But with the increase in storage capacity, the magnetization of microscopic magnetic grains becomes unstable due to the "superparamagnetic effect"[25, 26]. This effect occurs due to the reduction in size of the magnetic grains as it loses the magnetic orientation due to random thermal vibrations at room temperature. Antiferromagnetically Coupled Media (AFC) is one solution to

the above problem that can obstruct the superparamagnetic effect and can achieve higher storage density. AFC media consists of two magnetic layers antiferromagnetically coupled through a thin nonmagnetic layer[27, 28]. In this kind of media, stability is optimized by controlling the thickness of the layers. Some scientists found that, magnetic materials with high magnetic anisotropy are better candidates than the AFC media. In all the above recording media, a number of grains are used as a single bit[29, 30], whereas in patterned magnetic media each bit consists of a lithographically patterned island, having larger volume than a single grain. So the thermal stability is higher in patterned magnetic media than that in the granular media.

In ferromagnetic/nonmagnetic/ferromagnetic conductive thin film layers Giant Magnetoresistance (GMR) was observed[31, 32]. Here current flows parallel to the thin film layers (CIP geometry)[14]. Modern recording head of a hard-disk drives (HDD) works based on this phenomenon. If a thin insulating nonmagnetic layer is sandwiched between two ferromagnetic thin film layers then it is called Magnetic Tunnel Junction (MTJ) and it can produce large signal at room temperature[33] due to large tunnel-magnetoresistance[34, 35] (TMR) ratio, which can help to make read-head sensors and magnetoresistive random access memory (MRAM)[24]. The randomly used conventional solid state memories such as Dynamic Random Access Memory (DRAM) and Static Random Access Memory (SRAM) are volatile in nature[5]and commonly used popular non-volatile memory is electronic FLASH memory. Ferroelectric RAM (FeRAM)[5, 7] and MRAM[36]are growing alternative non-volatile memory technologies but they currently suffer from lower storage densities and higher cost than FLASH. However, extensive research is ongoing to overcome these difficulties and to develop competitive or better memory technologies based on FeRAM and MRAM.

The concept of conventional logic devices is mainly based on transistors. The continuous increment of the number of devices per unit area needs shrinkage of metal-oxide-semiconductor field effect transistor (MOSFET). This will cause the power dissipation problem and will increase the difficulties in interconnection wiring. A new innovative field “Spintronics” rapidly evolved in contemporary science and technology as an alternative route of solution to this problem. Spintronics may replace the world of electronics[37-40]. This new idea came in 1980s by Albert Fert[31] and Peter

Grunberg[41]. Conventional electronics is based upon the electronic charge whereas the spintronics consists of both spin and charge of an electron. Here both the charge and spin are used for logic and memory operations.

In magnetic-recording industry[42], the designing of spin logic device was a challenging task[38]. Just after the invention of GMR, Dutta and Das[43] proposed an electron spin based field effect transistor (Spin-FET), where the electric field at gate controls the orientation of spins. Spin FET has some advantages over electronic FET. It can be used for fast reprogrammable logic devices with their own memory and can eliminate the time delay between the reading data from magnetic memories and processing it with the semiconductor based electronics. Recently they have been realized experimentally[44, 45]; however their functioning at ambient conditions is questionable.

Spintronic devices can show high-speed and nonvolatile operations with low power consumptions[37, 46]. A number of works have been published on magnetic logic devices[47-49]. One approach demonstrated the development of a logic device based on domain walls[8] while Kostylev *et al*.[50] also reported the spin wave based logic device in the same year. The main difficulty to realize the magnon spintronic[26-28, 30, 51, 52] circuits arises due to the conversion of the electronic signal to the spin wave signal and *vice-versa*, and to manipulate or control the spin wave signal by some external means. Spin wave interference can be used in Mach-Zehnder type current controlled spin wave interferometer. Spin wave amplitude[53, 54] and phase[55] have been used to demonstrate a range of spin wave logic gates.

Spin waves[56-59] are collective excitations of magnetic moments in magnetically ordered materials. In 1930, Bloch first demonstrated the concept of spin waves. Magnons are the quasiparticles of spin waves. They are capable of carrying the spin current (spin angular momentum) and can be used as possible carrier of information. In comparison with photons, spin waves have some disadvantages like slower group velocities and higher attenuation. However, the miniaturization of device compensates this issue and makes fast processing and modulation, the most valuable features of spin wave circuitry.

Magnetic materials with periodically modulated properties (superlattice, dipolar coupled dot/stripe arrays, antidot arrays, *etc.*) can be considered as a propagating medium of magnons (spin waves) and are known as magnonic crystals[15, 18, 60-63]. This is an artificial crystal and is analogous to photonic crystal where light or photon plays a role as carrier. With this new artificial crystal, a new and young research field has been evolved known as "Magnonics"[15-18, 64, 65]. The aim of this field is to control and manipulate spin waves in a ferromagnetic material.[17] The frequency of magnons can be tuned by varying the magnetic material and the externally applied bias magnetic field. A broad range (1~100 GHz) of frequency can be covered using a range of materials. The spatial periodicity (translational symmetry) of magnonic crystals determines their band structures analogous to crystals in solid or other artificial crystals such as photonic, plasmonic and phononic crystals[19, 66]. The spectrum of magnons splits into so called bands, *i.e.*, energy regions in which magnon propagation is allowed and there also exist band gaps where the magnon propagation is forbidden. In magnonic crystals, presence of defects and impurities can further lead to a local modification of magnetic properties such as anisotropy, exchange stiffness and saturation magnetization and also can modify the magnonic band structures. The dispersion of magnonic frequency with the wave vector depends strongly upon various magnetic energies including exchange, magnetostatic, demagnetization and Zeeman energies. It can be tuned by various physical and material parameters and as well as the magnetic field. The periodicity of physical arrangement of the lattice in these artificial crystals determines the magnonic band structure. This may also arise due to the complex internal magnetic field of the lattice.

Ordered arrays of ferromagnetic nanodots, nanoparticles, nanostripes are potential candidates of magnonic crystals. Recently ferromagnetic antidot lattices, *i.e.*, periodic array of holes fabricated onto a continuous magnetic film have drawn the attention of researchers. These arrays of holes have attracted an increasing interest from both fundamental and technological points of view[67]. Magnetic antidots have also been considered as candidates for ultrahigh density data storage devices[68] where, the memory bit could be trapped between the consecutive holes along the intrinsic hard axis of the antidot nanostructure[69]. The antidots have some advantages at the deep nanoscale dimensions due to the absence of any small magnetic entity, and they do not suffer from the superparamagnetic bottleneck. Magnetic antidot lattices are

exchange-coupled magnetic systems and offer high propagation velocity (steeper frequency vs. wave vector dispersion) and longer propagation length for the magnons as opposed to magnetostatically coupled nanodot lattices.

Spin wave generation with their controlled propagation and the detection is the key to the success in future technology. At some particular frequency, generation of controlled spin wave is not an easy task. There are different ways to generate spin waves such as by picosecond magnetic field pulses either launched from a photoconductive switch[70] or pulsed electric field[71] or harmonic magnetic field[72]. Ultrashort laser pulses[73, 74] is also used to generate spin waves. A new phenomenon known as Spin Transfer Torque (STT) is being used to excite the spin waves with the help of spin polarized current[75]. Our future technology demands different new spin wave based nanoscale microwave components and devices such as spin wave amplifier[76], phase shifter[77], splitter, filter[21] and interferometer[54]. During last few decades, scientists made some studies both theoretically and experimentally on different properties of spin waves such as reflection and refraction[78-81], interference and diffractions[82-85], tunneling[86, 87] and focusing and self-focusing[88-91].

The most challenging problem in the field of magnonics is the successful synthesis or fabrication of high quality magnetic materials or ordered arrays of nanomagnets to fulfill all the technological applications. So in recent years, scientific community pays a huge attention for the nanofabrication and investigation of the magnetization dynamics of ordered arrays of nanostructures[92-102]. According to the technological demand, fabrication of magnetic ultrathin films and multilayers with high surface and interface qualities and nanomagnets with narrow size dispersion in ordered arrays over a macroscopic length scale is required. These will lead us to the development of a number of ‘top-down’ and ‘bottom-up’ approaches in nanofabrication methods and more recently a combination of the two. The bottom-up approach mainly relies upon solution phase colloidal chemistry[103] and electrochemistry using different templates such as track-etched polymer[104], anodic alumina[105] and di-block copolymer membranes[106]. On the other hand the top-down approach relies mainly on physical processes, which include different kinds of lithographic techniques such as photolithography[107], electron beam lithography (EBL)[108], deep ultraviolet lithography (DUV)[109], x-ray lithography[110], interference or holographic lithography (IL)[111], nano-imprint lithography (NIL)[112], and ion beam lithography (IBL)[113]. Scanning probe

lithography[114], step growth methods[115], laser or ion irradiation[116], shadow masks[117] are also very important techniques.

The quasistatic and ultrafast magnetization dynamics of magnetic nanostructures are different from their bulk or thin film properties. The static magnetization state forms the basis for studying the magnetization dynamics of a sample. The static magnetization state depends on various material parameters such as exchange stiffness constant, saturation magnetization, magnetocrystalline anisotropy and also on the physical structures of the arrays including shape, size, inter-element separation and lattice symmetry. It also depends on external parameters such as the strength and direction of the applied magnetic field. In last few decades lots of sophisticated and sensitive characterization techniques[118]have been developed to study the quasistatic and ultrafast dynamic magnetic properties. Magnetic force microscopy (MFM)[119] and Lorentz force microscopy[120] are now very common and are extensively used microscopic systems to map the gradient of the stray magnetic field and the sample magnetization, respectively. Both of the techniques can serve us to obtain a spatial resolution better than 10 nm. In MFM the contrast of image arises from the magnetic force between the scanning magnetic tip and the stray magnetic field gradient from the sample. However, in Lorentz Force Microscopy the deflection of the accelerated electrons initiated by Lorentz force after transmitting through thin magnetic specimens creates the magnetic contrast of the image. However, extraction of the quantitative information directly from each of these imaging techniques is non-trivial. The amplitude and phase information of spin configuration and stray magnetic field can be mapped by another imaging technique, named electron holography[121], based upon the electron interference with a very high spatial resolution down to 2 nm. For mapping the sample magnetization a popular technique *viz.*, Magneto-Optical Kerr Effect (MOKE)[122]is being used for a long time and its spatial resolution is in sub-μm scale. The Photoemission Electron Microscopy (PEEM)[123] is a form of x-ray microscopy and it has a far better spatial resolution than visible light imaging. Spin polarized low energy electron microscopy (SPLEEM)[124], scanning electron microscopy with polarization analysis (SEMPA)[125], spin polarized scanning tunneling microscopy (SP-STM)[126] and ballistic electron microscopy (BEMM)[127] are some very important and high quality imaging techniques, which give excellent spatial resolution of 10 nm or better. To get the image contrast, these techniques use the spin dependent

transmission, scattering or tunneling of electrons. Although all these techniques have very good spatial resolutions, but they suffer from the lack of high temporal resolution.

Subsequently, for studying the high speed magnetization dynamics, different experimental techniques have been discovered in the frequency, wave vector and time-domains. The frequency domain techniques are the conventional ferromagnetic resonance (FMR)[128] and vector network analyzer based broadband ferromagnetic resonance (VNA-FMR)[129] spectrometer. Both the techniques are efficient to measure the high frequency magnetic resonance, permeability and loss from MHz to tens of GHz regime limited only by the instrumental bandwidth with a very good spectral resolution. Later Tamaru *et al.* developed the spatially resolved FMR[130] for imaging the resonant mode profiles of confined magnetic elements. To study the GHz frequency spin waves in the wave vector domain Brillouin Light Scattering (BLS)[131, 132]is extensively used and it is based upon the inelastic light scattering from spin waves and other quasiparticles. By the help of this technique one can measure the dispersion of the frequency of spin waves with its wave vector by varying the angle of incidence of light *with respect to* the sample plane. Recently space and time-resolved BLS techniques have been developed to get sub-μm spatial resolution and few ns temporal resolution[132]. Although the best spatio-temporal resolution is obtained from time-resolved magneto-optical Kerr effect (TRMOKE) microscope[133, 134]. This technique is used to probe the ultrafast magnetization dynamics in time-domain and it can achieve tens of femtosecond temporal resolution limited only by the pulse-width of the laser. There are other time-domain techniques for studying the magnetization dynamics including pulse inductive magnetometry[135], magnetoresistive methods[136] and x-ray microscopy[137]. However, they can offer similar spatio-temporal resolution like TRMOKE. Time-resolved scanning Kerr microscopy (TRSKM)[138-140] is a variant of TRMOKE, which is used to image the time evolution of magnetization excited by a time-dependent magnetic field.

This thesis is focused on the study of static and dynamic magnetization properties of two-dimensional magnonic crystals. Here we chose to investigate two-dimensional antidot lattices, which are one of the most promising candidates for two-dimensional magnonic crystals. A number of parameters of the antidot lattices can be varied to

tune the spin wave properties. These include antidot shape, antidot size, lattice constant, lattice symmetry and the base materials. In addition, the strength and orientation of the external bias magnetic field can also be varied to actively control the spin wave spectrum in this system. During last few decades significant amount of works have been done on the ferromagnetic antidot lattices. Initial studies on the dynamics of ferromagnetic antidot lattices showed pattern induced splitting of surface and volume modes[141], localization, confinement, and field-controlled propagation of spin waves[142, 143] and observation of dispersive and entangled spin waves between the antidots[144]. Later, anisotropic propagation and damping of spin waves were observed due to magnetic field controlled spin wave guiding in a network of interconnected nanowires[145]. Field independent localized modes[146], effects of lattice symmetry[147] and diameters of the antidots on spin waves[148], formation of magnonic mini-bands[149], and tunable meta-material response in $Ni_{80}Fe_{20}$ antidot lattices[150] also attracted great interests.

In chapter 2, we will introduce the background theory of the topics presented in this thesis. We will discuss the basic principles of different experimental techniques used in this thesis. In chapter 3, we will discuss about the fabrication techniques used to prepare the samples investigated in this thesis. This is followed by some basic characterization techniques used to characterize the structure and morphology of the samples and as well as the static magnetic behavior of the samples. In chapter 4, we will describe the time-resolved magneto-optical Kerr effect microscope and the broadband ferromagnetic resonance spectrometer used for the measurements of the magnetization dynamics in time- and frequency-domains. The basics of the numerical methods used in this thesis will be presented in chapter 5. Chapters 6 to 9 present the research work performed in this thesis. Chapter 6 presents the fabrication and characterization of the base material *i.e.*, the Co and $Ni_{80}Fe_{20}$ continuous thin films and patterned 10×10 μm^2 films. This is important as the magnetic parameters extracted from this study will be further used for investigation of the magnetization dynamics of Co and $Ni_{80}Fe_{20}$ antidot lattices as presented in Chapters 7 to 9.

Chapter 7 presents the time-domain measurements of optically induced precessional dynamics in a series of Co antidot lattices with fixed antidot diameter of 100 nm and with varying lattice constants (S) between 200 and 500 nm. For the sparsest lattice, we observe two bands of precessional modes with a bandgap, which increases

substantially with the decrease in *S* down to 300 nm. At *S* = 200 nm four distinct bands with significant bandgaps appear. The numerically calculated mode profiles show various localized and extended modes with the propagation direction perpendicular to the bias magnetic field. We numerically demonstrate some composite antidot structures with very rich magnonic spectra spreading between 3 and 27 GHz based upon the above experimental observations. Chapter 8 presents an experiment and simulation work which shows that the optically induced spin wave spectra of nanoscale $Ni_{80}Fe_{20}$ antidot lattices can be tuned by changing the antidot shape. The spin wave spectra also show an anisotropy with the variation of the in-plane bias field orientation. Analyses show this is due to various quantized and extended modes, whose nature changes with the antidot shape and bias field orientation as a result of the variation of the internal magnetic field profile. The observed variation and anisotropy in the spin waves with the internal and external parameters are important for their applications in magnonic devices. Chapter 9 presents the investigation of the variation in spin wave spectrum in two-dimensional nanoscale $Ni_{80}Fe_{20}$ antidot lattices with lattice symmetry. By varying the bias magnetic field values in a broadband ferromagnetic resonance spectrometer, we observed a stark variation in the spin wave spectrum with the variation of lattice symmetry. The simulated mode profiles showed further difference in the spatial nature of the modes between different lattices. While for square and rectangular lattices extended modes are observed in addition to standing spin wave modes; all modes in the hexagonal, honeycomb and octagonal lattices are either localized or standing waves. In addition, the honeycomb and octagonal lattices showed two different types of modes confined within the honeycomb(octagonal) units and between two such consecutive units. Simulated internal magnetic fields confirm the origin of such a wide variation in the frequency and spatial nature of the spin wave modes. The tunability of spin waves with the variation of lattice symmetry is important for the design of future magnetic data storage and magnonic devices. Chapter 10 summarizes the results and discusses the future perspectives of the works presented in this thesis from both fundamental and application perspectives.

Bibliography

[1] M. Fowler, "Historical Beginnings of Theories of Electricity and Magnetism," (1997).

[2] T. Thomson, G. Hu and B. D. Terris, *Phys. Rev. Lett.* **96**, 257204 (2006).

[3] B. D. Terris, T. Thomson and G. Hu, *Microsyst Technol* **13**, 189 (2007).

[4] O. Hellwig, A. Berger, T. Thomson, E. Dobisz, Z. Z. Bandic, H. Yang, D. S. Kercher and E. E. Fullerton, *Appl. Phys. Lett.* **90**, 162516 (2007).

[5] S. Tehrani, E. Chen, M. Durlam, M. DeHerrera, J. M. Slaughter, J. Shi and G. Kerszykowski, *J. Appl. Phys.* **85**, 5822 (1999).

[6] J. Åkerman, *Science* **308**, 508 (2005).

[7] R. C. Sousa and I. L. Prejbeanu, *C. R. Physique* **6**, 1013 (2005).

[8] D. A. Allwood, G. Xiong, C. C. Faulkner, D. Atkinson, D. Petit and R. P. Cowburn, *Science* **309**, 1688 (2005).

[9] A. Imre, G. Csaba, L. Ji, A. Orlov, G. H. Bernstein and W. Porod, *Science* **311**, 205 (2006).

[10] D. B. Carlton, N. C. Emley, E. Tuchfeld and J. Bokor, *Nano Lett.* **8**, 4173 (2008).

[11] R. P. Cowburn, D. K. Koltsov, A. O. Adeyeye, M. E. Welland and D. M. Tricker, *Phys. Rev. Lett.* **83**, 1042 (1999).

[12] T. Shinjo, T. Okuno, R. Hassdorf, K. Shigeto and T. Ono, *Science* **289**, 930 (2000).

[13] S. H. Chung, A. Hoffmann, S. D. Bader, C. Liu, B. Kay, L. Makowski and L. Chen, *Appl. Phys. Lett.* **85**, 2971 (2004).

[14] J. R. Childress and R. E. Fontana Jr, *C. R. Physique* **6**, 997 (2005).

[15] S. Neusser and D. Grundler, *Adv. Mater.* **21**, 2927 (2009).

[16] V. Kruglyak and R. Hicken, *J. Magn. Magn. Mater.* **306**, 191 (2006).

[17] V. V. Kruglyak, S. O. Demokritov and D. Grundler, *J. Phys. D: Appl. Phys.* **43**, 264001 (2010).

[18] B. Lenk, H. Ulrichs, F. Garbs and M. Münzenberg, *Phys. Rep.* **507**, 107 (2011).

[19] Y. Au, M. Dvornik, O. Dmytriiev and V. V. Kruglyak, *Appl. Phys. Lett.* **100**, 172408 (2012).

[20] J. W. Kłos, D. Kumar, J. Romero-Vivas, H. Fangohr, M. Franchin, M. Krawczyk and A. Barman, *Phys. Rev. B* **86**, 184433 (2012).

[21] S.-K. Kim, K.-S. Lee and D.-S. Han, *Appl. Phys. Lett.* **95**, 082507 (2009).

[22] M. Arruebo, R. Fernández-Pacheco, M. R. Ibarra and J. Santamaría, *Nano Today* **2**, 22 (2007).

[23] A. K. Gupta and M. Gupta, *Biomaterials* **26**, 3995 (2005).

[24] E. D. Daniel, C. D. Mee and M. H. Clark, "Magnetic Recording: The First 100 Years," *IEEE Press*, (1998).

[25] S. H. Charap, L. Pu-Ling and H. Yanjun, *IEEE Trans. Magn.* **33**, 978 (1997).

[26] D. Weller and A. Moser, *IEEE Trans. Magn.* **35**, 4423 (1999).

[27] E. N. Abarra, A. Inomata, H. Sato, I. Okamoto and Y. Mizoshita, *Appl. Phys. Lett.* **77**, 2581 (2000).

[28] E. E. Fullerton, D. T. Margulies, M. E. Schabes, M. Carey, B. Gurney, A. Moser, M. Best, G. Zeltzer, K. Rubin, H. Rosen and M. Doerner, *Appl. Phys. Lett.* **77**, 3806 (2000).

[29] M. Todorovic, S. Schultz, J. Wong and A. Scherer, *Appl. Phys. Lett.* **74**, 2516 (1999).

[30] G. F. Hughes, *IEEE Trans. Magn.* **36**, 521 (2000).

[31] M. N. Baibich, J. M. Broto, A. Fert, F. N. Van Dau, F. Petroff, P. Etienne, G. Creuzet, A. Friederich and J. Chazelas, *Phys. Rev. Lett.* **61**, 2472 (1988).

[32] S. S. P. Parkin, Z. G. Li and D. J. Smith, *Appl. Phys. Lett.* **58**, 2710 (1991).

[33] J. S. Moodera, L. R. Kinder, T. M. Wong and R. Meservey, *Phys. Rev. Lett.* **74**, 3273 (1995).

[34] M. Julliere, *Phys. Lett.* **54A**, 225 (1975).

[35] D. Wang, C. Nordman, J. M. Daughton, Z. Qian and J. Fink, *IEEE Trans. Magn.* **40**, 2269 (2004).

[36] J. M. Daughton, *Thin Solid Films* **216**, 162 (1992).

[37] S. A. Wolf, D. D. Awschalom, R. A. Buhrman, J. M. Daughton, S. von Molnár, M. L. Roukes, A. Y. Chtchelkanova and D. M. Treger, *Science* **294**, 1488 (2001).

[38] I. Žutić, J. Fabian and S. Das Sarma, *Rev. Mod. Phys.* **76**, 323 (2004).

[39] S. D. Bader and S. S. P. Parkin, *Anl. Rev. Cond. Matt. Phys.* **1**, 71 (2010).

[40] H. Ohno, *Nat. Mater.***9**, 952 (2010).

[41] G. Binasch, P. Grünberg, F. Saurenbach and W. Zinn, *Phys. Rev. B* **39**, 4828 (1989).

[42] S. Wolf, D. Treger and A. Chtchelkanova, *MRS Bulletin* **31**, 400 (2011).

[43] S. Datta and B. Das, *Appl. Phys. Lett.* **56**, 665 (1990).

[44] H. C. Koo, J. H. Kwon, J. Eom, J. Chang, S. H. Han and M. Johnson, *Science* **325**, 1515 (2009).

[45] C. Betthausen, T. Dollinger, H. Saarikoski, V. Kolkovsky, G. Karczewski, T. Wojtowicz, K. Richter and D. Weiss, *Science* **337**, 324 (2012).

[46] G. A. Prinz, *Science* **282**, 1660 (1998).

[47] R. P. Cowburn and M. E. Welland, *Science* **287**, 1466 (2000).

[48] R. Richter, H. Boeve, L. Bär, J. Bangert, G. Rupp, G. Reiss and J. Wecker, *Solid State Electron.* **46**, 639 (2002).

[49] A. Ney, C. Pampuch, R. Koch and K. H. Ploog, *Nature* **425**, 485 (2003).

[50] M. P. Kostylev, A. A. Serga, T. Schneider, B. Leven and B. Hillebrands, *Appl. Phys. Lett.* **87**, 153501 (2005).

[51] A. Moser, K. Takano, D. T. Margulies, M. Albrecht, Y. Sonobe, Y. Ikeda, S. Sun and E. E. Fullerton, *J. Phys. D: Appl. Phys.* **35**, R157 (2002).

[52] S.-i. Iwasaki, *J. Magn. Magn. Mater.* **235**, 227 (2001).

[53] K. S. Lee and S. K. Kim, *J. Appl. Phys.* **104**, 053909 (2008).

[54] T. Schneider, A. A. Serga, B. Leven, B. Hillebrands, R. L. Stamps and M. P. Kostylev, *Appl. Phys. Lett.* **92**, 022505 (2008).

[55] A. Khitun, M. Bao and K. L. Wang, *J. Phys. D: Appl. Phys.* **43**, 264005 (2010).

[56] F. Bloch, *Z. Phys.* **61**, 206 (1930).

[57] A. I. Akhiezer, V. G. Bar'yakhtar, S. V. Peletminskii, S. Chomet, S. Doniach and A. Ilitch, "Spin Waves," *North-Holland Publishing Company*, (1968).

[58] G. A. Gurevich and A. G. Melkov, "Magnetization Oscillations and Waves," *CRC Press*, (1996).

[59] P. A. and D. D. Stancil, "Spin Waves: Theory and Applications," *Springer*, (2009).

[60] L. J. Heyderman and R. L. Stamps, *J. Phys.: Condens. Matter* **25**, 363201 (2013).

[61] H. Puszkarski and M. Krawczyk, *Solid State Phenom.* **94**, 125 (2003).

[62] G. P. Srivastava, "The Physics of Phonons," *CRC Press*, (1990).

[63] S. Nikitov, P. Tailhades and C. Tsai, *J. Magn. Magn. Mater.* **236**, 320 (2001).

[64] A. A. Serga, A. V. Chumak and B. Hillebrands, *J. Phys. D: Appl. Phys.* **43**, 264002 (2010).

[65] S. O. Demokritov and A. N. Slavin, "Magnonics: From Fundamentals to Applications," *Springer*, (2013).

[66] R. P. Cowburn, A. O. Adeyeye and J. A. C. Bland, *Appl. Phys. Lett.* **70**, 2309 (1997).

[67] O. Martyanov, V. Yudanov, R. Lee, S. Nepijko, H. Elmers, R. Hertel, C. Schneider and G. Schönhense, *Phys. Rev. B* **75**, 174429 (2007).

[68] L. Torres, L. Lopez-Diaz and O. Alejos, *J. Appl. Phys.* **87**, 5645 (2000).

[69] C. C. Wang, A. O. Adeyeye and N. Singh, *Nanotech.* **17**, 1629 (2006).

[70] M. R. Freeman, R. R. Ruf and R. J. Gambino, *IEEE Trans. Magn.* **27**, 4840 (1991).

[71] S. Tamaru, J. A. Bain, R. J. M. van de Veerdonk, T. M. Crawford, M. Covington and M. H. Kryder, *Phys. Rev. B* **70**, 104416 (2004).

[72] R. W. Damon and H. van de Vaart, *Phys. Rev. Lett.* **12**, 583 (1964).

[73] A. V. Kimel, A. Kirilyuk, F. Hansteen, R. V. Pisarev and T. Rasing, *J. Phys.: Condens. Matter* **19**, 043201 (2007).

[74] G. M. Müller, G. Eilers, Z. Wang, M. Scherff, R. Ji, K. Nielsch, C. A. Ross and M. Münzenberg, *New J. Phys.* **10**, 123004 (2008).

[75] S. I. Kiselev, J. C. Sankey, I. N. Krivorotov, N. C. Emley, R. J. Schoelkopf, R. A. Buhrman and D. C. Ralph, *Nature* **425**, 380 (2003).

[76] Y. Acremann, X. W. Yu, A. A. Tulapurkar, A. Scherz, V. Chembrolu, J. A. Katine, M. J. Carey, H. C. Siegmann and J. Stohr, *Appl. Phys. Lett.* **93**, 102513 (2008).

[77] R. Hertel, W. Wulfhekel and J. Kirschner, *Phys. Rev. Lett.* **93**, 257202 (2004).

[78] F. Goedsche, *Physica Status Solidi B* **39**, 1 (1970).

[79] J. Gouzerh, A. A. Stashkevich, N. G. Kovshikov, V. V. Matyushev and J. M. Desvignes, *J. Magn. Magn. Mater.* **101**, 189 (1991).

[80] Y. I. Gorobets and S. A. Reshetnyak, *Tech. Phys.* **43**, 188 (1998).

[81] A. V. Vashkovsky and E. H. Lock, *Phys. Usp.* **49**, 389 (2006).

[82] V. K. Dugaev, P. Bruno, B. Canals and C. Lacroix, *Phys. Rev. B* **72**, 024456 (2005).

[83] S. K. Choi, K. S. Lee and S. K. Kim, *Appl. Phys. Lett.* **89**, 062501 (2006).

[84] K. Perzlmaier, G. Woltersdorf and C. H. Back, *Phys. Rev. B* **77**, 054425 (2008).

[85] D. R. Birt, B. O'Gorman, M. Tsoi, X. Li, V. E. Demidov and S. O. Demokritov, *Appl. Phys. Lett.* **95**, 122510 (2009).

[86] S. O. Demokritov, A. A. Serga, A. André, V. E. Demidov, M. P. Kostylev, B. Hillebrands and A. N. Slavin, *Phys. Rev. Lett.* **93**, 047201 (2004).

[87] A. Kozhanov, D. Ouellette, M. Rodwell, S. J. Allen, A. P. Jacob, D. W. Lee and S. X. Wang, *J. Appl. Phys.* **105**, 07D311 (2009).

[88] F. Morgenthaler, *IEEE Trans. Magn.* **8**, 550 (1972).

[89] M. Bauer, C. Mathieu, S. O. Demokritov, B. Hillebrands, P. A. Kolodin, S. Sure, H. Dötsch, V. Grimalsky, Y. Rapoport and A. N. Slavin, *Phys. Rev. B* **56**, R8483 (1997).

[90] R. Khomeriki, *Eur. Phys. J. B* **41**, 219 (2004).

[91] V. E. Demidov, S. O. Demokritov, K. Rott, P. Krzysteczko and G. Reiss, *Phys. Rev. B* **77**, 064406 (2008).

[92] C. Elachi, *IEEE Trans. Magn.* **11**, 36 (1975).

[93] J. Jorzick, S. O. Demokritov, B. Hillebrands, B. Bartenlian, C. Chappert, D. Decanini, F. Rousseaux and E. Cambril, *Appl. Phys. Lett.* **75**, 3859 (1999).

[94] R. L. Stamps and R. E. Camley, *Phys. Rev. B* **60**, 12264 (1999).

[95] S. Jung, B. Watkins, L. DeLong, J. B. Ketterson and V. Chandrasekhar, *Phys. Rev. B* **66**, 132401 (2002).

[96] A. Barman, V. V. Kruglyak, R. J. Hicken, J. Scott, A. Kundrotaite and M. Rahman, *J. Appl. Phys.* **95**, 6998 (2004).

[97] V. V. Kruglyak, A. Barman, R. J. Hicken, J. R. Childress and J. A. Katine, *Phys. Rev. B* **71**, 220409(R) (2005).

[98] L. Giovannini, F. Montoncello and F. Nizzoli, *Phys. Rev. B* **75**, 024416 (2007).

[99] G. Gubbiotti, S. Tacchi, G. Carlotti, N. Singh, S. Goolaup, A. O. Adeyeye and M. Kostylev, *Appl. Phys. Lett.* **90**, 092503 (2007).

[100] A. Barman and S. Barman, *Phys. Rev. B* **79**, 144415 (2009).

[101] J. M. Shaw, T. J. Silva, M. L. Schneider and R. D. McMichael, *Phys. Rev. B* **79**, 184404 (2009).

[102] S. Tacchi, M. Madami, G. Gubbiotti, G. Carlotti, H. Tanigawa, T. Ono and M. P. Kostylev, *Phys. Rev. B* **82**, 024401 (2010).

[103] A. L. Rogach, D. V. Talapin, E. V. Shevchenko, A. Kornowski, M. Haase and H. Weller, *Adv. Funct. Mater.* **12**, 653 (2002).

[104] W. D. Williams and N. Giordano, *Phys. Rev. B* **33**, 8146 (1986).

[105] H. Masuda, H. Yamada, M. Satoh, H. Asoh, M. Nakao and T. Tamamura, *Appl. Phys. Lett.* **71**, 2770 (1997).

[106] Y. Kamata, A. Kikitsu, H. Hieda, M. Sakurai and K. Naito, *J. Appl. Phys.* **95**, 6705 (2004).

[107] J. Aizenberg, J. A. Rogers, K. E. Paul and G. M. Whitesides, *Appl. Phys. Lett.* **71**, 3773 (1997).

[108] P. B. Fischer and S. Y. Chou, *Appl. Phys. Lett.* **62**, 2989 (1993).

[109] N. Singh, S. Goolaup and A. O. Adeyeye, *Nanotech.* **15**, 1539 (2004).

[110] F. Rousseaux, D. Decanini, F. Carcenac, E. Cambril, M. F. Ravet, C. Chappert, N. Bardou, B. Bartenlian and P. Veillet, *J. Vac. Sci. Technol. B* **13**, 2787 (1995).

[111] E. F. Wassermann, M. Thielen, S. Kirsch, A. Pollmann, H. Weinforth and A. Carl, *J. Appl. Phys.* **83**, 1753 (1998).

[112] J. Moritz, S. Landis, J. C. Toussaint, R. Bayle-Guillemaud, B. Rodmacq, G. Casali, A. Lebib, Y. Chen, J. P. Nozires and B. Dieny, *IEEE Trans. Magn.* **38**, 1731 (2002).

[113] D. Parikh, B. Craver, H. N. Nounu, F. Fu-On and J. C. Wolfe, *J. Microelectromechanical Sys.* **17**, 735 (2008).

[114] K. Bessho, Y. Iwasaki and S. Hashimoto, *J. Appl. Phys.* **79**, 5057 (1996).

[115] A. Dallmeyer, C. Carbone, W. Eberhardt, C. Pampuch, O. Rader, W. Gudat, P. Gambardella and K. Kern, *Phys. Rev. B* **61**, R5133 (2000).

[116] T. Devolder, C. Chappert, Y. Chen, E. Cambril, H. Bernas, J. P. Jamet and J. Ferre, *Appl. Phys. Lett.* **74**, 3383 (1999).

[117] F. Marty, A. Vaterlaus, V. Weich, C. Stamm, U. Maier and D. Pescia, *J. Appl. Phys.* **85**, 6166 (1999).

[118] M. R. Freeman and B. C. Choi, *Science* **294**, 1484 (2001).

[119] Y. Martin and H. K. Wickramasinghe, *Appl. Phys. Lett.* **50**, 1455 (1987).

[120] J. N. Chapman, *J. Phys. D: Appl. Phys.* **17**, 623 (1984).

[121] M. S. Cohen, *J. Appl. Phys.* **38**, 4966 (1967).

[122] B. E. Argyle and J. G. McCord, *J. Appl. Phys.* **87**, 6487 (2000).

[123] J. Stohr, Y. Wu, B. D. Hermsmeier, M. G. Samant, G. R. Harp, S. Koranda, D. Dunham and B. P. Tonner, *Science* **259**, 658 (1993).

[124] H. Pinkvos, H. Poppa, E. Bauer and J. Hurst, *Ultramicroscopy* **47**, 339 (1992).

[125] K. Koike and K. Hayakawa, *Jpn. J. Appl. Phys.* **23**, L187 (1984).

[126] M. Johnson and J. Clarke, *J. Appl. Phys.* **67**, 6141 (1990).

[127] W. H. Rippard and R. A. Buhrman, *Appl. Phys. Lett.* **75**, 1001 (1999).

[128] S. V. Vonsovskii, "Ferromagnetic Resonance: The Phenomenon of Resonant Absorption of a High-Frequency Magnetic Field in Ferromagnetic Substances," 4, (1966).

[129] V. P. Denysenkov and A. M. Grishin, *Rev. Sci. Instrum.* **74**, 3400 (2003).

[130] S. Tamaru, J. A. Bain, R. J. M. van de Veerdonk, T. M. Crawford, M. Covington and M. H. Kryder, *J. Appl. Phys.* **91**, 8034 (2002).

[131] J. V. Harzer, B. Hillebrands, R. L. Stamps, G. Güntherodt, D. Weller, C. Lee, R. F. C. Farrow and E. E. Marinero, *J. Magn. Magn. Mater.* **104**, 1863 (1992).

[132] S. O. Demokritov, B. Hillebrands and A. N. Slavin, *Phys. Rep.* **348**, 441 (2001).

[133] A. Barman and A. Haldar, *Solid State Phys.* **65**, 108 (2014).

[134] A. Barman, S. Wang, J. D. Maas, A. R. Hawkins, S. Kwon, A. Liddle, J. Bokor and H. Schmidt, *Nano Lett.* **6**, 2939 (2006).

[135] T. J. Silva, C. S. Lee, T. M. Crawford and C. T. Rogers, *J. Appl. Phys.* **85**, 7849 (1999).

[136] I. N. Krivorotov, N. C. Emley, J. C. Sankey, S. I. Kiselev, D. C. Ralph and R. A. Buhrman, *Science* **307**, 228 (2005).

[137] Y. Acremann, J. P. Strachan, V. Chembrolu, S. D. Andrews, T. Tyliszczak, J. A. Katine, M. J. Carey, B. M. Clemens, H. C. Siegmann and J. Stöhr, *Phys. Rev. Lett.* **96**, 217202 (2006).

[138] W. K. Hiebert, A. Stankiewicz and M. R. Freeman, *Phys. Rev. Lett.* **79**, 1134 (1997).

[139] Y. Acremann, C. H. Back, M. Buess, O. Portmann, A. Vaterlaus, D. Pescia and H. Melchior, *Science* **290**, 492 (2000).

[140] A. Barman, V. V. Kruglyak, R. J. Hicken, A. Kundrotaite and M. Rahman, *Appl. Phys. Lett.* **82**, 3065 (2003).

[141] S. McPhail, C. M. Gürtler, J. M. Shilton, N. J. Curson and J. A. C. Bland, *Phys. Rev. B* **72**, 094414 (2005).

[142] S. Neusser, B. Botters and D. Grundler, *Phys. Rev. B* **78**, 054406 (2008).

[143] S. Neusser, B. Botters, M. Becherer, D. Schmitt-Landsiedel and D. Grundler, *Appl. Phys.Lett.***93**, 122501 (2008).

[144] M. Kostylev, G. Gubbiotti, G. Carlotti, G. Socino, S. Tacchi, C. Wang, N. Singh, A. O. Adeyeye and R. L. Stamps, *J. Appl. Phys.* **103**, 07C507 (2008).

[145] S. Neusser, G. Duerr, H. Bauer, S. Tacchi, M. Madami, G. Woltersdorf, G. Gubbiotti, C. Back and D. Grundler, *Phys. Rev. Lett.* **105**, 067208 (2010).

[146] H. Ulrichs, B. Lenk and M. Münzenberg, *Appl. Phys. Lett.* **97**, 092506 (2010).

[147] S. Tacchi, M. Madami, G. Gubbiotti, G. Carlotti, A. O. Adeyeye, S. Neusser, B. Botters and D. Grundler, *IEEE Trans. Magn.* **46**, 1440 (2010).

[148] J. Ding, D. Tripathy and A. O. Adeyeye, *J. Appl. Phys.* **109**, 07D304 (2011).

[149] S. Neusser, G. Duerr, S. Tacchi, M. Madami, M. Sokolovskyy, G. Gubbiotti, M. Krawczyk and D. Grundler, *Phys. Rev. B* **84**, 094454 (2011).

[150] S. Neusser, H. G. Bauer, G. Duerr, R. Huber, S. Mamica, G. Woltersdorf, M. Krawczyk, C. H. Back and D. Grundler, *Phys. Rev. B* **84**, 184411 (2011).

Chapter 2

Theoretical Background

2.1 Ferromagnetism

A ferromagnetic material has a spontaneous magnetic moment even in zero applied magnetic fields. The existence of a spontaneous magnetic moment suggests that electron spin and magnetic moments are arranged in an ordered manner. For a simple ferromagnet the order of spin arrangement should be parallel to each other. This ferromagnetic material has a spontaneous magnetic moment called saturation moment.

Now, a ferromagnetic material placed within a magnetic field *H*, may create a non-zero magnetic moment. Magnetic moment per unit volume is known as magnetization and conventionally it is represented by the symbol of *M*. Magnetic susceptibility χ is defined[1] as the ratio of magnetization *M* to the magnetic field *H*:

$$M \equiv \chi H \tag{2.1}$$

The relation between magnetic susceptibility χ and magnetic field *H* determines the magnetic ordering of a material. These criteria classify the diamagnetic, paramagnetic, ferromagnetic, antiferromagnetic or ferrimagnetic material. Langevin's classical theory of diamagnetism uses the electron's orbital angular momentum to adequately explain why the diamagnetic susceptibility χ_d (typically of the order of 10^{-6} cm^3/mol) is always negative and independent of changes to temperature or the magnetic field *H*. The diamagnetic susceptibility χ_d for an *N* number. of atoms per unit volume is expressed as:

$$\chi_d = -\frac{Ne^2}{6mc^2}\sum_{i=1}^{Z}\langle r^2\rangle r_i \tag{2.2}$$

Here *Z* is the number. of electrons within each atom, *m* is the mass of an electron and *c* is the speed of light.

The Curie-Weiss law-Paramagnetic Behavior:

To describe the spontaneous alignment of the magnetic moment in a ferromagnetic material, Weiss introduced an internal field[2](Weiss field) proportional to the magnetization ~ $\lambda_W M$, where $\lambda_W$is a constant. In 1895 Curie[3] reported that some materials possessed a temperature-dependent and field-independent susceptibility and it is given by

$$\chi_{para} = \frac{C}{T} \tag{2.3}$$

Where C is the Curie constant. Using the above equation 2.3 and writing the total magnetic field as $H + \lambda_W M$, equation 2.1 becomes

$$M = \frac{C}{T}(H + \lambda_W M) \tag{2.4}$$

Then solving for M

$$M\left(1 - \frac{C\lambda_W}{T}\right) = \frac{CH}{T} \tag{2.5}$$

And recovering the form of equation 2.1

$$M = \frac{CH}{(T - C\lambda_W)} = \frac{CH}{(T - T_C)} \tag{2.6}$$

Where the magnetic susceptibility is given by

$$\chi = \frac{C}{(T - T_C)} \tag{2.7}$$

The Curie-Weiss law describes the susceptibility of ferromagnetic materials for $T>T_C$, in which case the material exhibit paramagnetic behavior. For $T<T_C$ the material is ferromagnetic and exhibits a spontaneous magnetization. T_C is called the Curie temperature.

The Heisenberg theory establishes that this molecular field comes from the quantum mechanical exchange interaction. Pauli's exclusion principle dictates that the two electronic wavefunctions of a hydrogen molecule must combine anti-symmetrically. Using separation of variables, the wavefunction ψ (r_i, s_i) of an electron can be expanded as

$$\psi(r_i, s_i) = \rho(r_i)\sigma(s_i) \tag{2.8}$$

where ρ and σ are functions of electron's position r_i and spin s_i, respectively. Now, the anti-symmetric wavefunctions can be expressed as either of equations. 2.9 or 2.10.

$$\psi_s = \rho_{sym}(r_1, r_2)\sigma_{anti}(s_1, s_2) \tag{2.9}$$

$$\psi_T = \rho_{anti}(r_1, r_2)\sigma_{sym}(s_1, s_2) \tag{2.10}$$

Here, $\psi_S$and $\psi_T$represent the singlet and the triplet states, respectively. They can be expanded as

$$\psi_s = A[\rho_a(r_1)\rho_b(r_2) + \rho_a(r_2)\rho_b(r_1)]\big[\sigma_\alpha(s_1)\sigma_\beta(s_2) - \sigma_\alpha(s_2)\sigma_\beta(s_1)\big] \tag{2.11}$$

and

$$\psi_T = B[\rho_a(r_1)\rho_b(r_2) - \rho_a(r_2)\rho_b(r_1)]\begin{bmatrix}\sigma_\alpha(s_1)\sigma_\alpha(s_2)\\ \sigma_\alpha(s_1)\sigma_\beta(s_2) + \sigma_\alpha(s_2)\sigma_\beta(s_1)\\ \sigma_\beta(s_1)\sigma_\beta(s_1)\end{bmatrix} \tag{2.12}$$

Spins are antiparallel in the singlet state with a total spin quantum number S = 0. However, in the triplet state, the total spin quantum number S = 1 allows for a degeneracy of (2S + 1) = 3 states. The energies for singlet (E_S) and triplet (E_T) states can be written as

$$E_s = A^2(K_{12} + J_{12}) \tag{2.13}$$

$$E_T = B^2(K_{12} - J_{12}) \tag{2.14}$$

Here, K_{12} and J_{12} denote the Coulomb interaction and exchange integral, respectively. They can be expressed by the following two integrals:

$$K_{12} = \int \rho_a^*(r_1)\rho_b^*(r_2)\,\mathcal{H}_{12}\rho_a(r_1)\rho_b(r_2)d\tau_1 d\tau_2 \tag{2.15}$$

$$J_{12} = \int \rho_a^*(r_1)\rho_b^*(r_2)\,\mathcal{H}_{12}\rho_a(r_2)\rho_b(r_1)d\tau_1 d\tau_2 \tag{2.16}$$

Here, $\mathcal{H}_{12} = \frac{e^2}{r_{ab}} + \frac{e^2}{r_{12}} - \frac{e^2}{r_{1b}} - \frac{e^2}{r_{a2}}$: $r_{ij} = |r_i - r_j|$, is the Hamiltonian for electron 1 and 2 in a hydrogen molecule with nuclei *a* and *b*.

A positive J_{12} favours the triplet state – and the parallel arrangement of spins – as E_T decreases. This is the case with ferromagnets, where the interatomic spacing r_{ab} is larger as compared to the radii of the *d* and *f* electronic orbitals. J_{12} becomes negative in antiferromagnetic materials leading to an antiparallel arrangement of neighboring spins. This results in a zero net magnetism. In the case of ferrimagnets the antiparallel magnetic moments do not have the same magnitude. This is due to the presence of two sub-lattices hosting twotypes of ions with differing magnetic moments. This bestows ferrimagnets with some net magnetization at low temperatures. Analogous to the Curie temperature for ferromagnets, there exists a Ne´el temperature for

antiferromagnets and ferrimagnets above which the thermal energy overcomes the energy of the magnetic ordering and a paramagnetic behavior unfolds.

2. 2 Magnetic Energies

In presence of an external magnetic field, the total free energy (E_{total}) of a ferromagnetic material is the vector sum of four different free energies. It can be written as:

$$E_{total} = E_z + E_d + E_e + E_k \tag{2.17}$$

where, $E_z$is the Zeeman energy, E_d is the demagnetization energy, E_e is the exchange energy and E_K is the magnetocrystalline energy. In the following subsections we will discuss about those different energy terms and their dependence on the magnetization *M*.

2.2.1 Zeeman Energy

In presence of external field *H*, the interaction of *H* and magnetization *M* produces the energy of a magnetic system, which is known as Zeeman energy, and it can be expressed as;

$$E_z = -\int \boldsymbol{M}.\boldsymbol{H}\, dv\,, \tag{2.18}$$

Zeeman energy will become minimum when the magnetization will be aligned parallel to the applied magnetic field.

2.2.2 Demagnetization Energy

The demagnetization energy is sometimes known as self-magnetostatic energy. This energy term emanates from the interaction between the magnetization configurations with the magnetic field generated by itself. From the fundamental Maxwell's equation we know,

$$\begin{aligned} \nabla.\boldsymbol{B} &= 0 \\ \Rightarrow \nabla.(\boldsymbol{H} + 4\pi\boldsymbol{M}) &= 0 \\ \Rightarrow \nabla.\boldsymbol{H} &= -4\pi(\nabla.\boldsymbol{M}) \end{aligned} \tag{2.19}$$

So the stray magnetic field can be expressed as the divergence of magnetization. The demagnetizing energy is expressed as

$$E_d = -\frac{1}{2}\int \boldsymbol{M}.\boldsymbol{H}_d \, d^3r \tag{2.20}$$

where $\boldsymbol{H}_d$ is the stray magnetic field, which can be expressed as

$$\boldsymbol{H}_d = -\boldsymbol{N}.\boldsymbol{M} \tag{2.21}$$

Here, *N* is the demagnetization tensor. When the magnetization is uniform demagnetization tensor (*N*) becomes diagonal and can be expressed as a constant. So the demagnetizing energy (E_d) turns to a simplified version and it is written as

$$E_d = \frac{1}{2}\int NM^2 \, d^3r \tag{2.22}$$

The stray field energy term is also associated with the volume (ρ_v) and surface (σ_s) charge densities. The volume and surface charges can be expressed as

$$\begin{aligned} \rho_v &= -\nabla.\boldsymbol{M} \\ \text{and} \quad \sigma_s &= \boldsymbol{M}.\boldsymbol{n} \end{aligned} \tag{2.23}$$

Here, *n* is the normal direction to the surface. The potential energy associated with the stray field is given by[4]

$$U_d(\boldsymbol{r}) = \frac{M_s}{4\pi}\left(\int_V \frac{\rho_v(\boldsymbol{r}')}{|\boldsymbol{r}-\boldsymbol{r}'|}d^3\boldsymbol{r}' + \int_s \frac{\sigma_s(\boldsymbol{r}')}{|\boldsymbol{r}-\boldsymbol{r}'|}d^2\boldsymbol{r}'\right) \tag{2.24}$$

So the stray field or demagnetizing field can be determined by

$$\boldsymbol{H}_d(\boldsymbol{r}) = -\nabla U_d(\boldsymbol{r}) \tag{2.25}$$

With the help of volume charge and surface charge densities, the demagnetizing field can be written as[4]

$$\boldsymbol{H}_d(\boldsymbol{r}) = \frac{1}{4\pi}\left(\int_V \frac{\rho_v(\boldsymbol{r}')(\boldsymbol{r}-\boldsymbol{r}')}{|\boldsymbol{r}-\boldsymbol{r}'|^3}d^3r' + \int_s \frac{\sigma_s(\boldsymbol{r}')(\boldsymbol{r}-\boldsymbol{r}')}{|\boldsymbol{r}-\boldsymbol{r}'|^3}d^2r'\right) \tag{2.26}$$

Finally the demagnetizing energy becomes

$$E_d(\boldsymbol{r}) = \mu_0 M_s\left(\int_V \rho_v(\boldsymbol{r})U_d(\boldsymbol{r})d^3\,\boldsymbol{r} + \int_S \sigma_s(\boldsymbol{r})U_d(\boldsymbol{r})d^2\,\boldsymbol{r}\right) \tag{2.27}$$

2.2.3 Exchange Energy

From the history of magnetism we know that Weiss first assumed that in a ferromagnetic material the coherence of spin direction basically depends on a magnetic field called molecular field. Then Heisenberg established that this molecular field was due to spin-spin interaction, which is now known as exchange interaction. Pauli's exclusion principle and Coulomb's interaction are the quantum origin of this interaction. Indeed, both position and motion of electrons are conditioned by their

spin states because two electrons cannot be in exactly the same quantum state at the same place. Due to this a spin correlation occurs between first neighbors. In metals, electronic band structures have to be taken into account. In insulators, this interaction between first neighbors exists but mainly due to the overlap between localized electron wave function.

If we consider two pair of spins let us say *i* and *j* then the exchange Hamiltonian H_{ex} can be written as[5]

$$H_{ex} = -2J_{ij} \sum_{i,j}{}' \boldsymbol{s}_i . \boldsymbol{s}_j \tag{2.28}$$

where $J_{i,j}$ is the exchange interaction parameter between spin *i* and *j*. For an isotropic crystal $J_{i,j}$ can be replaced by J_e. The value of J_e is positive for ferromagnets and negative for anti-ferromagnets for the first neighbors. In the continuum limit, the exchange energy of a magnetic volume *V* may be expressed as:

$$E_x = \frac{A}{M_S^2} \int_V \left(\vec{\nabla} . \vec{M}\right)^2 dV \tag{2.29}$$

where *A* is the exchange energy which depends on *J* and the crystal structure, *M* is the magnetization, M_s is the saturation magnetization and $\vec{\nabla}$ is the nabla operator.

2.2.4 Magnetocrystalline Anisotropy Energy

Magnetocrystalline energy is the effect of spin-orbit interaction between the electrons orbitals and the crystal lattice. This coupling takes place as the electron orbits tend to deform along the crystallographic axes and the spin show this effect *i.e.*, a spin-orbit interaction, favouring directions related to the structure of the material. These preferential directions are known as easy axes, and the anisotropy energy of a material is expressed by an energy density *K*, which may be the sum of multiple contributions, associated to the structures of the material.

Magnetocrystalline anisotropy can be distinguished in uniaxial, cubic or a higher odd order depending on the terms used to describe the energy surface and it is associated to an equivalent number of preferred crystallographic axes for the magnetization.

For hexagonal crystal, the anisotropy energy density is expressed as a function of angle (θ) between the magnetization with the *c*-axis, known as uniaxial anisotropy. The expression of this anisotropy is[5]

$$E_k = K_1 \sin^2\theta + K_2 \sin^4\theta \tag{2.30}$$

where K_1 and K_2 are constants and also functions of temperature.

For cubic anisotropy, the anisotropy energy can be expressed by direction cosines α_1, α_2 and α_3 of the direction of magnetization with the cube edges[5]

$$E_k = K_1'(\alpha_1^2\alpha_2^2 + \alpha_2^2\alpha_3^2 + \alpha_3^2\alpha_1^2) + K_2'\alpha_1^2\alpha_2^2\alpha_3^2 \quad (2.31)$$

The value of various K factors are measured by taking the differences in energy between a configuration with the magnetization aligned with one of these easy axes and a configuration with the magnetization aligned perpendicularly to it, and their values may depend strongly on temperature.

2.3 Magnetic Domains

A ferromagnetic specimen is composed of small regions known as domains, within each of which the local magnetization is saturated. The exchange energy is almost 10^3 times greater than the dipolar energy and it is a short range interaction (decays exponentially with distance) whereas the dipolar energy is a long range interaction ($\infty 1/r^3$). For a large ferromagnetic sample there will be a competition between these two interactions, which leads to the formation of magnetic domains. In a single domain the exchange interaction is dominating, however for a multi-domain ferromagnetic specimen each domain is separated by domain walls and here dipolar interaction dominates over exchange interaction over longer lengthscale. The directions of magnetization of different domains need not to be parallel rather they tend to form flux closure configuration to minimize the total magnetic energy of the system.

Two neighbouring domains are separated by a domain wall where the direction of magnetic moment changes gradually to minimize the total energy associated with the domain wall. The thickness of a domain wall can be expressed by the following relation[6]:

$$\delta = \sqrt{\frac{J_e\pi^2S^2}{Ka}} \quad (2.32)$$

Where, $J_e$is the exchange integral, K is the anisotropy constant and a is the lattice constant. Among different kinds of domain walls Bloch and Néel walls are most common and well studied.

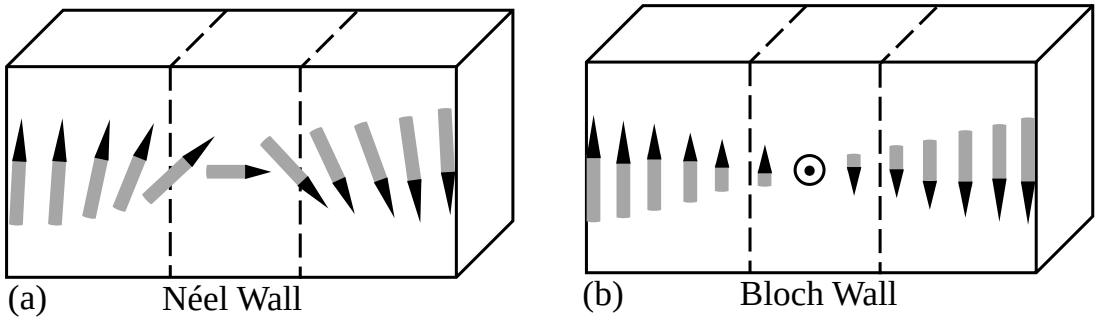

Figure 2.1: (a) Néel wall and (b) Bloch wall are shown between two domains.

Bloch wall (named after the physicist Felix Bloch) is a narrow transition region at the boundary between magnetic domains, over which the magnetization rotates through the plane of the domain wall *i.e.*, along the axis perpendicular to the plane of the wall shown in Figure 2.1(b). Bloch domain walls generally appear in bulk materials, *i.e.*, when sizes of magnetic material are considerably larger than domain wall width.
In case of Néel wall (named after the physicist Louis Néel) the magnetization rotates along an axis parallel to the plane of the wall shown in Figure 2.1(a). Néel walls are the common magnetic domain wall type in very thin films where the exchange length is large compared to the thickness. The typical domain wall width for Co, Ni and $Ni_{80}Fe_{20}$ are about 10 nm, 60 nm and 57 nm[7, 8].

2.4 Magnetization Dynamics

2.4.1 Landau-Lifshitz-Gilbert Equation

The dynamic characteristic of spin can be expressed by an equation of motion. This equation of motion can also be derived from quantum theory[4, 9]. The time evolution of a spin observable S can be derived by its commutation with the Hamiltonian operator H and the relation will be as below:

$$i\hbar \frac{d}{dt} S = [S, \mathrm{H}] \tag{2.33}$$

The Hamiltonian operator basically describes the interaction between the spin and the external magnetic field, which mainly produces its flux *B* and expressed as:

$$\mathrm{H} = -\frac{g\mu_B}{\hbar}\boldsymbol{S}.\boldsymbol{B}\,, \tag{2.34}$$

where μ_B is the Bohr magneton and g is the gyromagnetic factor for a free electron. With the help of the commutation rules for spin operators

$$[S_i, S_j] = i\hbar\varepsilon_{ijk}S_k \tag{2.35}$$

And from equations (2.33), (2.34) and (2.35) we get

$$\frac{d}{dt}\langle \boldsymbol{S}\rangle = \frac{g\mu_B}{\hbar}\,\boldsymbol{S}\times\boldsymbol{B} \tag{2.36}$$

This above equation corresponds to the motion of a single spin. According to macrospin model the magnetization *M* is uniform throughout the sample and so the relation between the *S* and *M* becomes

$$\boldsymbol{M} = \frac{g\mu_B}{\hbar}\langle \boldsymbol{S}\rangle \tag{2.37}$$

As a result the equation of motion of magnetization in presence of an external magnetic field will be

$$\frac{d\boldsymbol{M}}{dt} = -\frac{g\mu_B}{\hbar}(\boldsymbol{M}\times\boldsymbol{H})$$
$$\text{or,}\frac{d\boldsymbol{M}}{dt} = -\gamma\,(\boldsymbol{M}\times\boldsymbol{H}) \tag{2.38}$$

Equation(2.38) is known as Landau-Lifshitz equation where damping term is not included and here $\gamma = \frac{g\mu_B}{\hbar}$ which is called as the gyromagnetic ratio.

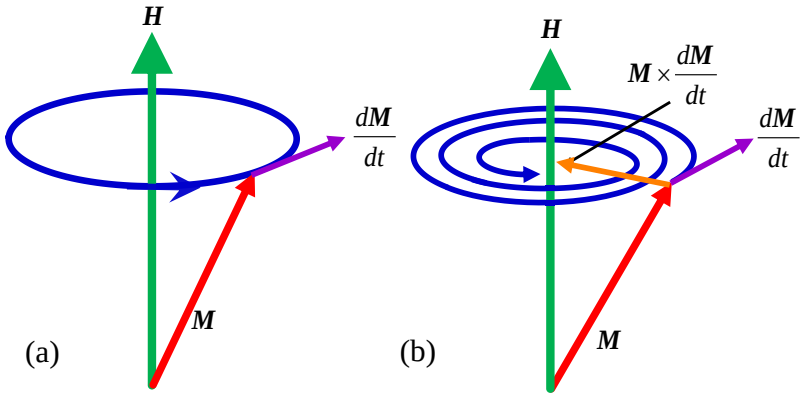

Figure 2.2: Magnetization precession around the applied magnetic field (*H*) (a) in absence of damping term and (b)in presence of a damping term.

Equation (2.38) will become more general if we replace *H* by H_{eff}. The physics behind this equation is that the tip of magnetization vector precesses *with respect to* the effective magnetic field in a circular orbit as shown in Figure 2.2(a) for infinitely long time with an angular frequency $\omega = \gamma H_{eff}$. In a real system with the passage of time the precession amplitude of magnetization decreases and the tip of magnetization vector tends towards the center of equilibrium following a spiral path (Figure 2.2(b)). So due to this effect a damping term of magnetization should be added with Landau-Lifshitz equation[10].

So one can write,

$$\frac{d\boldsymbol{M}}{dt} = -\gamma(\boldsymbol{M} \times \boldsymbol{H}_{eff}) + R\left(\boldsymbol{M}, \boldsymbol{H}_{eff}\right) \tag{2.39}$$

The term *R* is the damping term, which depends on the magnetization and effective magnetic field.

For the damping term Landau-Lifshitz suggested[11]

$$R = -\frac{\lambda}{M_s^2}\boldsymbol{M} \times \left(\boldsymbol{M} \times H_{eff}\right) \tag{2.40}$$

and Gilbert proposed[12, 13]

$$R = \frac{\alpha}{M_s}\left(\boldsymbol{M} \times \frac{d\boldsymbol{M}}{dt}\right) \tag{2.41}$$

Taking in account Gilbert's proposal the equation of motion of magnetization vector in presence of damping can be expressed as

$$\frac{d\boldsymbol{M}}{dt} = -\gamma\left(\boldsymbol{M} \times \boldsymbol{H}_{eff}\right) + \frac{\alpha}{M_s}\left(\boldsymbol{M} \times \frac{d\boldsymbol{M}}{dt}\right) \tag{2.42}$$

This is the well-known form of Landau-Lifshitz-Gilbert (LLG) equation. α is the Gilbert damping constant.

2.4.2 Time Scales of Magnetization Processes

Over a wide range of time scales from μs to fs magnetization dynamics can occur. The time scale of magnetization dynamics is shown in Figure 2.3 This time scale (τ) is determined by the interaction energies (*E*) via Heisenberg relation $\tau = \frac{h}{E}$. From the time scale we can see that fundamental exchange interaction is the fastest process and

domain wall motion is the slowest process. The fundamental exchange interaction occurs within 10 fs whereas the typical time scale of domain wall motion is few ns to hundreds of μs. The spin-orbit coupling and spin-transfer torque occurs in the time scale of 10 fs-1 ps. Laser induced ultrafast demagnetization occurs within few hundreds of fs. The fast remagnetization time following the ultrafast demagnetization covers the time scale of 1-10 ps. The magnetic writing process done via reversal of spin and it exists along a time scale of few ps to few hundreds of ps, whereas the vortex core switching occurs form few tens of ps to ns time scale. Precession of magnetization covers few ps to few hundreds of ps time scale whereas the Gilbert damping associated with the magnetization precession occurs from sub-ns to tens of ns time scale. The spin waves in ferromagnetic material can propagate in a time scale of few hundreds of ps to tens of ns before it dies out.

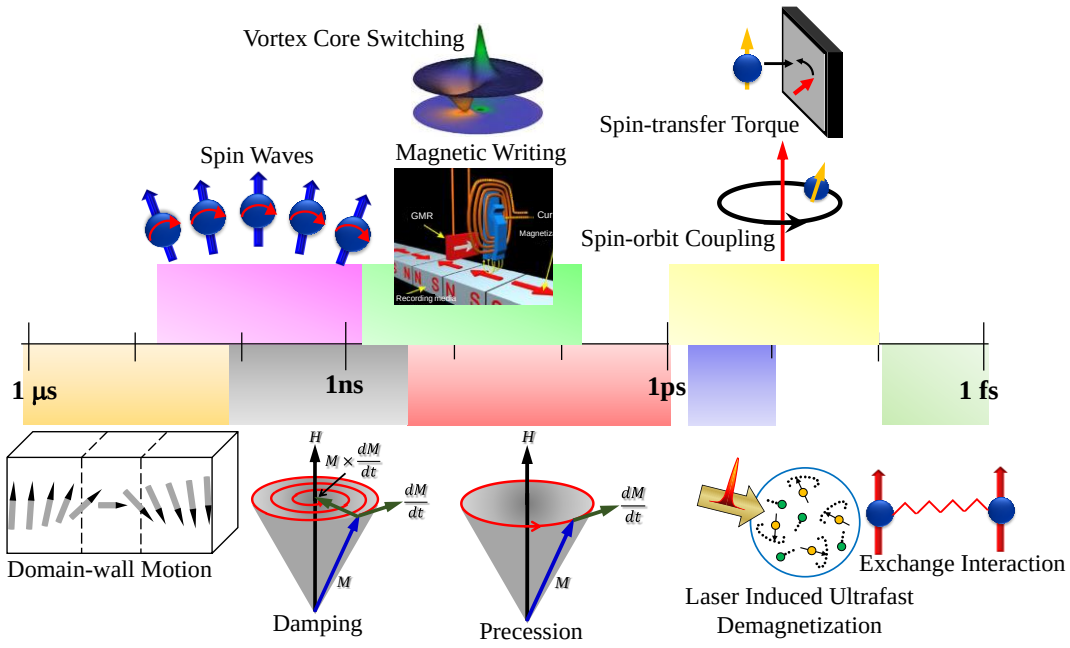

Figure 2.3: Time scales for various kinds of magnetization processes.

2.4.3 Femto and Picosecond Magnetization Dynamics

When an ultrafast laser pulse falls upon a ferromagnetic material then the after effect of the interaction between the laser pulse and the ferromagnetic material is a quite interesting topic of research. The path breaking research in this topic started by the pioneering work by Beaurepaire *et al*. in 1996[14]. They found that a nickel thin film can be demagnetized in sub-picosecond time scales after the excitation with a sub 100

fs pulsed laser beam. After that a lot of studies over all elementary ferromagnetic transition metals (Co, Ni, Fe) and several alloys confirmed the above result[15]. Then an important question came in mind that how the magnetic moment of system can be quenched so quickly, while its total angular momentum is conserved? Before the laser excitation, the angular momentum is mainly carried by the aligned electron spins. So, a transfer of angular momentum to another degree of freedom, such as electrons or lattice, is required to compensate the loss of magnetic order[16]. Figure 2.4 describes the sequence of phenomena happens when a ferromagnetic material interacts with ultrashort laser pulses and below the underlying mechanism are discussed by considering the transfer of angular momentum among different degrees of freedom.

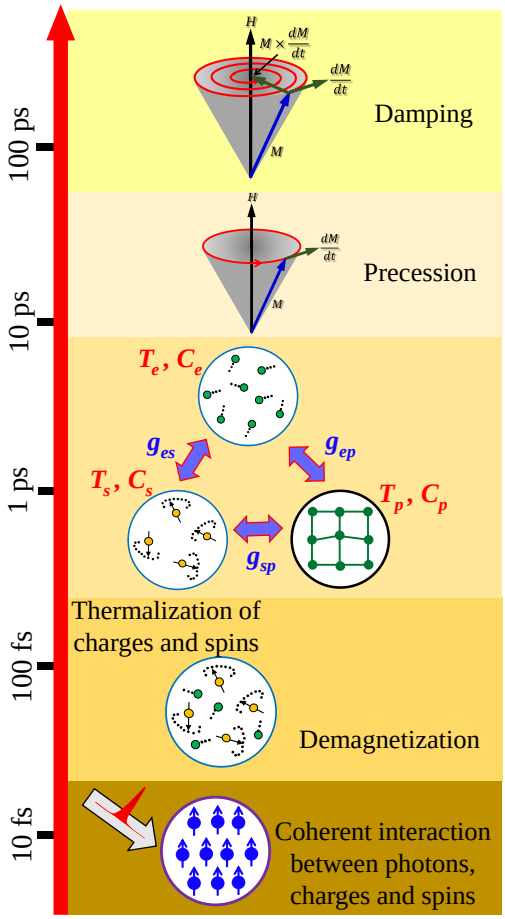

Figure 2.4: Schematic diagram of different stages of mechanisms in ultrafast magnetization dynamics.

A number of processes occur when a femtosecond laser pulse interacts with an ordered ferromagnetic material. At first the photon field of the laser beam interacts with spin degrees of freedom of electrons. The angular momentum of light is

modified nonlinearly within first 50 fs. Initially the electronic distribution is not thermalized. The electrons are excited above the Fermi level because of electron–electron scattering[17]. The excited electrons are called 'hot electrons'[18]. In this time the electronic temperature may be increased up to 10^3K[17]. Shortly after that, the thermalization of spin population occurs as the 'hot electrons' excite the spins by electron-magnon interaction[16, 19]. So, there is a difference between the thermalization times of charges (τ_e) and spins (τ_s). During the thermalization of charges and spins, the electronic wave function loses its phase memory (incoherent process) *with respect to*the excitation, which leads to the demagnetization of the ferromagnet. However, the underlying mechanism of demagnetization is a subject of intense debate. Most of the scientists in magnetism community believe that during the excitation and thermalization of the electrons, Stoner pairs with a large kinetic energy are excited in ferromagnetic metals like Ni or Co[17]. Therefore, most of the published reports on the ultrafast demagnetization state that ultrafast spin-flip scatterings play important role for demagnetization. The first one is the Elliott-Yafet type of scattering, which says that an electron flips its spin due to the influence of impurity centers and phonons and emits or absorbs a phonon[20, 21].Other kinds of scattering processes such as electron-magnon spin-flip scattering[22], Coulomb exchange spin-flip scattering[23] and relativistic electromagnetic radiation induced spin-flip scattering[24] have also claimed to be responsible for the ultrafast demagnetization. However, few reports also claim that other kinds of physical mechanisms like spin-orbit coupling[25], the coupling with the electromagnetic field via a terahertz emission[26] are responsible for ultrafast demagnetization. Moreover, some recent reports show that the superdiffusive spin transport rather than spin-flip plays the major role in magnetic processes in the femtosecond time scale[27, 28].

After the demagnetization, the electronic charges and spins start to relax. This relaxation occurs in two different time scales (few ps and hundreds of ps). Therefore, the reflectivity (depends on the population of charges above the Fermi level) and also magnetization of the system decays bi-exponentially. The faster relaxation time (τ_1) of the hot electrons and spins occurs, because they exchange energy with the lattice and this is mediated by the electron–phonon interaction. $\tau_1$may vary from sub-ps to several ps depending on the electron–phonon coupling and also on the specific heat of the electrons and phonons[23, 28, 29]. The relaxation time also depends on the density of

laser excitation[28, 29] and magneto- crystalline anisotropy[23] to some extent. In this time scale, the thermodynamic quantities such as specific heat and temperature come into play. Therefore, one may talk about phenomenological three temperature model (3TM)[14, 29]. In 3TM, heat capacities and temperatures are assigned to the reservoirs of electron charge (*e*), spin (*s*) and lattice/phonon (*p*) as ($C_e;T_e$), ($C_s;T_s$) and ($C_p;T_p$), respectively.

Furthermore, coupling constants between charge-spin, spin-lattice, charge-lattice are defined as g_{es},g_{sp},g_{ep}. They describe the rate of energy exchange between the participating sub-systems. Thus, the overall dynamics is phenomenologically described by a set of three coupled differential equations. By exchanging heats, spins come to an equilibrium temperature with charge and lattice. Therefore, the lattice temperature also changes. The magnetocrystalline anisotropy, which is a function of lattice temperature also changes rapidly. This rapid change in magnetocrystalline anisotropy acts as an internal pulsed magnetic field and triggers the precession of magnetization. The second or longer relaxation time (τ_2) corresponds to the diffusion of electron and lattice heat to the surroundings (such as substrate)[28, 29]. In this time scale, the precession of magnetization also starts to damp out. These mechanisms can be described by the Landau-Lifshitz-Gilbert formalism.

2.5 Ferromagnetic Resonance: Theory

Griffiths first observed the Ferromagnetic Resonance (FMR) phenomenon in 1946. A theory of this phenomenon was developed by Kittel in 1948[30, 31]. In principle, the electron spin resonance at microwave frequency for a ferromagnetic material and nuclear spin resonance is similar. When a microwave signal passes through a ferromagnetic material then the magnetic moment of the ferromagnetic material will start to precess either uniformly or non-uniformly about the direction of the applied static magnetic field (H_{ext}). The microwave power will be strongly absorbed when the frequency of the radio frequency transverse field (H_f) is equal to the precessional frequency of the moments.

2.5.1 Uniform Mode: Kittel Formula

From quantum mechanics the proportionality relationship between magnetic spin momentum μ and angular momentum L of electrons can be expressed as:

$$\mu = -\gamma L \tag{2.43}$$

Here γ is the gyromagnetic ratio. We know another important relation between rate of change of the angular momentum L and the applied static magnetic field H_{ext} and it can be expressed as:

$$\frac{dL}{dt} = \mu \times H_{ext} \tag{2.44}$$

Using equation (2.43) equation (2.44) can be rewritten as:

$$\frac{d\mu}{dt} = -\gamma\mu \times H_{ext} \tag{2.45}$$

Now if the volume average is taken in account, then the equation (2.45) can be expressed as:

$$\frac{1}{dV_r}\frac{d\sum_j \mu_j}{dt} = -\gamma \frac{\sum_j \mu_j}{dV_r} \times H_{ext} \tag{2.46}$$

By considering the definition of magnetization $= d\sum_j \frac{\mu_j}{dV_r}$, the continuum gyromagnetic precession model can be easily deduced as:

$$\frac{\partial M}{\partial t} = -\gamma M \times H_{ext} \tag{2.47}$$

The H_{ext} is usually replaced by the effective field H_{eff} which includes the external applied field and the anisotropy field in the nanostructures. So, the equation is written as:

$$\frac{\partial M}{\partial t} = -\gamma M \times H_{eff} \tag{2.48}$$

Let us consider an ellipsoid with principal axes parallel to the *X*, *Y* and *Z* axes to explain the resonance frequency for a general nanostructure. The external applied field H_x is along *X*-axis, while the r.f field H_y is along the *Y*-axis. The demagnetizing factors for the ellipsoid are N_x. N_y and N_z along *X*, *Y* and *Z* axes, respectively. The H_{eff} can be divided into the effective values for different directions as:

$$\begin{aligned} H_{eff-x} &= H_x - N_x M_x \\ H_{eff-y} &= H_y - N_y M_y \\ H_{eff-z} &= -N_z M_z \end{aligned} \tag{2.49}$$

The component equations of equation (2.48) can be obtained by substituting the H_{eff} with the $H_{eff\text{-}x}$, $H_{eff\text{-}y}$, $H_{eff\text{-}z}$ in equation (2.49):

$$\frac{dM_x}{dt} = -\gamma\left[\left(N_y - N_z\right)M_y - H_y\right]M_z \cong 0$$

$$\frac{dM_y}{dt} = -\gamma[H_x - (N_z - N_x)M_x]M_z$$

$$\frac{dM_z}{dt} = -\gamma\left[M_x H_y - \left(N_y - N_x\right)M_x M_y - M_y H_x\right] \tag{2.50}$$

The susceptibility χ_y can be obtained by solving these equations with time dependence $e^{i\omega t}$.

$$\chi_y = \frac{\chi_0}{1 - \left(\frac{\omega}{\omega_0}\right)^2} = \frac{M_y}{H_y} \tag{2.51}$$

in which,

$$\chi_0 = \frac{M_x}{H_x + \left(N_y - N_x\right)M_x}$$

and the resonance frequency is given by:

$$\omega_0 = \gamma\left\{[H_x + (N_z - N_x)4\pi M_x] \times \left[H_x + \left(N_y - N_x\right)4\pi M_x\right]\right\}^{1/2} \tag{2.52}$$

It can also be written in the unit of Hertz:

$$f_0 = \frac{\gamma}{2\pi}\left\{[H_x + (N_z - N_x)4\pi M_x] \times \left[H_x + \left(N_y - N_x\right)4\pi M_x\right]\right\}^{1/2} \tag{2.53}$$

This equation is the well-known Kittel's equation, which can be used to calculate ferromagnetic resonance frequency in ferromagnetic structures. The resonant frequency and their demagnetizing factor for few standard shapes are given in the list below[10, 31].

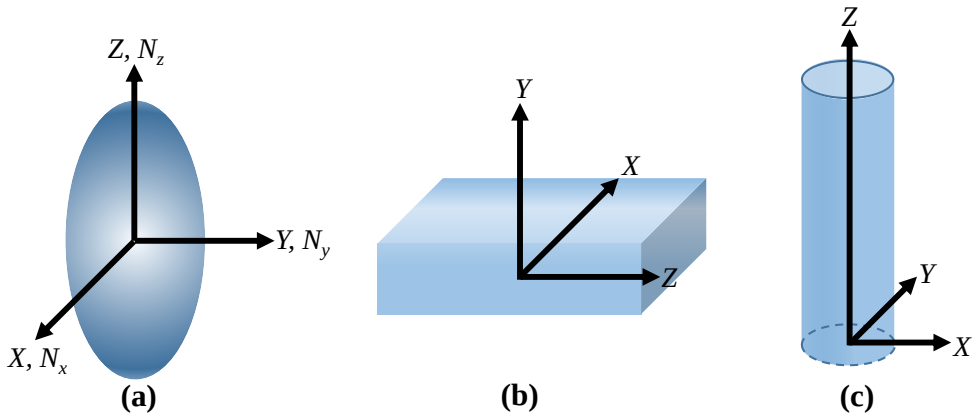

Figure 2.5: Co-ordinate systems for (a) an ellipsoid, (b) a plane and (c) a cylinder.

Table 1: Eigen frequencies for some standard shapes.

Shape	Magnetization direction	Demagnetizing Factors			Eigen Frequencies
		N_x	N_y	N_z	
Infinite Plane	Tangential	0	4π	0	$\omega_0 = \gamma[H_z(H_z + 4\pi M_z)]^{1/2}$
	Normal	0	0	4π	$\omega_0 = \gamma[H_z - 4\pi M_z]$
Infinite thin cylinder	Tangential	2π	2π	0	$\omega_0 = \gamma[H_z(H_z + 2\pi M_z)]^{1/2}$
	Normal	2π	0	2π	$\omega_0 = \gamma[H_z(H_z - 2\pi M_z)]^{1/2}$
Sphere	-	4π/3	4π/3	4π/3	$\omega_0 = \gamma H_z$

2.6 Spin Waves

2.6.1 Introduction

Spin waves are propagating disturbances in the ordered magnetic materials. Bloch first introduced this concept in the year of 1930. Suppose an array of spin is connected with each other by exchange interaction. If the system is then locally perturbed by some external perturbation, the disturbance will propagate as a wave and this phenomenon is known as the spin wave. This wave will generate due to the collective phase coherent precession of magnetization or spins in a ferromagnetic medium. The quanta of spin waves are also called as magnons. Like other physical waves, spin wave can exhibit different phenomena like resonance[30, 31], reflection[32-37], dispersion[38], interference and diffraction[39-41], Doppler effect[42-44] and formation of envelop solitons. Magnons are identified as bosons[45, 46]. Bose-Einstein condensation of magnons has also been observed in different magnetic systems[47-49]. Next, we will discuss about the exchange dominated and dipole dominated spin wave dispersion relations.

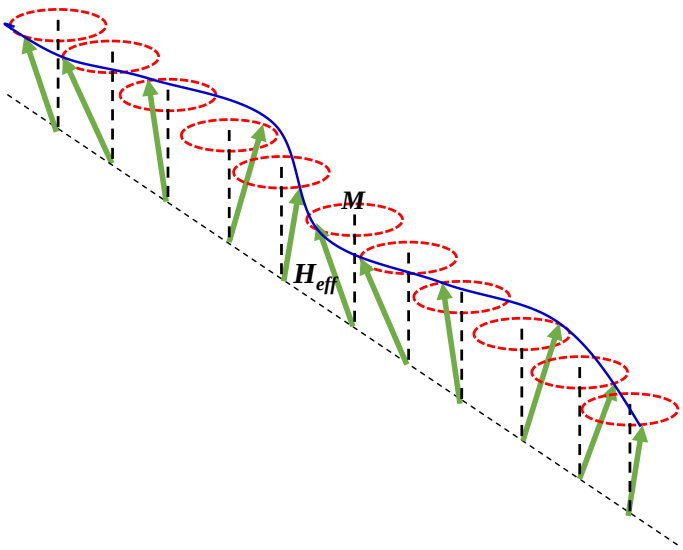

Figure 2.6: Precession of magnetization vector (***M***) around the effective field vector (***H***$_{eff}$) shows the propagation of spin wave.

2.6.2 Exchange Dominated Spin Wave

When the wavelength (λ) of a spin wave become very short (*i.e.*, the wave vector (k) is very large), then the spin wave is dominated by exchange interaction. Here we will derive the dispersion relation of a purely exchange spin wave. In the ground state all the spins are parallel to each other. Let us consider a chain of N spins and each of them has the magnitude 'S'. Considering Heisenberg interaction, the exchange interaction energy of p^{th} spin will be[47]

$$-2J\boldsymbol{S}_p \,.\, (\boldsymbol{S}_{p-1} + \boldsymbol{S}_{p+1}) \tag{2.54}$$

So the magnetic moment of p^{th} spin will be $\boldsymbol{\mu}_p = -g\mu_B \boldsymbol{S}_p$.

Substituting the value of magnetic moment into equation 2.54, we get the energy of the p^{th} spin

$$-\boldsymbol{\mu}_p \left[\left(-\frac{2J}{g\mu_B}\right)(\boldsymbol{S}_{p-1} + \boldsymbol{S}_{p+1})\right] = -\boldsymbol{\mu}_p . \boldsymbol{B}_p \tag{2.55}$$

where, $\boldsymbol{B}_p = \left(-\frac{2J}{g\mu_B}\right)(S_{p-1} + S_{p+1})$ is the total exchange field on thep^{th} spin. The torque on the p^{th} spin can be written as

$$\hbar \frac{d\boldsymbol{S}_p}{dt} = \boldsymbol{\mu}_p \times \boldsymbol{B}_p$$

$$\Rightarrow \quad \frac{d\boldsymbol{S}_p}{dt} = -\frac{g\mu_B}{\hbar}\boldsymbol{S}_p \times \left[\left(-\frac{2J}{g\mu_B}\right)(\boldsymbol{S}_{p-1} + \boldsymbol{S}_{p+1})\right]$$

$$= \left(\frac{2J}{\hbar}\right)\left(\boldsymbol{S}_p \times \boldsymbol{S}_{p-1} + \boldsymbol{S}_p \times \boldsymbol{S}_{p+1}\right) \tag{2.56}$$

For small amplitude of excitation $S_p^x, S_p^y << S$ and $S_p^z \cong S$. Neglecting the product of small terms, the linearized equations can be written as

$$\begin{aligned} \frac{dS_p^x}{dt} &= \left(\frac{2JS}{\hbar}\right)\left(2S_p^y - S_{p-1}^y - S_{p+1}^y\right) \\ \frac{dS_p^y}{dt} &= -\left(\frac{2JS}{\hbar}\right)\left(2S_p^x - S_{p-1}^x - S_{p+1}^x\right) \\ \frac{dS_p^z}{dt} &= 0 \end{aligned} \tag{2.57}$$

Let the solutions are of sinusoidal type *i.e.*,

$$S_p^x = me^{[i(pka-\omega t)]}; S_p^y = ne^{[i(pka-\omega t)]} \tag{2.58}$$

Substituting these in the above equations (equation2.57)

$$\begin{aligned} -i\omega m &= \left(\frac{2JS}{\hbar}\right)\left(2 - e^{-ika} - e^{ika}\right)n \\ -i\omega m &= \left(\frac{2JS}{\hbar}\right)\left(2 - e^{-ika} - e^{ika}\right)n \\ &= \left(\frac{4JS}{\hbar}\right)(1 - \cos ka)n \end{aligned} \tag{2.59}$$

And

$$\begin{aligned} -i\omega n &= \left(\frac{2JS}{\hbar}\right)\left(2 - e^{-ika} - e^{ika}\right)m \\ &= \left(\frac{4JS}{\hbar}\right)(1 - \cos ka)m \end{aligned} \tag{2.60}$$

The determinant of coefficients of equations 2.59 and 2.60 should be zero to have solution for *m* and *n*.

$$\begin{vmatrix} i\omega & \left(\frac{4JS}{\hbar}\right)(1 - \cos ka) \\ -\left(\frac{4JS}{\hbar}\right)(1 - \cos ka) & i\omega \end{vmatrix} = 0 \tag{2.61}$$

This gives

$$\hbar\omega = 4JS(1 - \cos ka) \tag{2.62}$$

At long wavelength limit, $ka \ll 1$.

Then,

$$\hbar\omega = (2JSa^2)k^2 \tag{2.63}$$

The dispersion of the spin wave frequency (ω) with the wave vector (k) is quadratic in nature for long wavelength limit *i.e.*, in the small k limit. The dispersion of the exchange spin wave is isotropic.

2.6.3 Magnetostatic Spin Wave Modes in Thin Films

Let us consider an infinite ferromagnetic thin film. Now if we apply an in-plane magnetic field in that thin film, then the magnetic moments will be aligned in the plane of the film. The wavelengths of excited spin waves depend upon the characteristic length scale of uniformity of the internal magnetic field. Due to the uniformity in magnetization and internal field, large wavelength spin waves ($\lambda \geq 1$ μm) are observed for such thin films. The spin waves observed in this case mainly come from dipolar interaction. The dispersion relations of dipolar modes can be calculated numerically by solving the Landau-Lifshitz equation (equation 2.38) after considering Maxwell's equations in magnetostatic limit:

$$\nabla \times \boldsymbol{H} = 0$$
$$\nabla . (\boldsymbol{H} + 4\pi \boldsymbol{M}_s) = 0 \tag{2.64}$$

The magnetization can be written as[50]

$$\boldsymbol{M}(\boldsymbol{r}, t) = \boldsymbol{M_s} + \boldsymbol{m}(\boldsymbol{r}, t) \tag{2.65}$$

In the above equation $\boldsymbol{M_S}$ is saturation magnetization and $\boldsymbol{m}$ is the small variation of magnetization due to the precession of magnetization. For small angle precession $m << M_S$. In this case $\boldsymbol{m}(\boldsymbol{r}, t)$ can be written as a sum of a series of plane waves.

$$\boldsymbol{m}(\boldsymbol{r}, t) = \sum_k \boldsymbol{m}_k e^{i(\omega t - \boldsymbol{k}.\boldsymbol{r})} \tag{2.66}$$

Using this condition, the nonlinear Landau-Lifshitz equation can be linearized and solved. The dispersion relation of a dipole-exchange spin wave in an infinite ferromagnetic material can be written by Herrings-Kittel formula[51]

$$\omega = \gamma \left[\left(H + \frac{2A}{M_s} k^2 \right) \left(H + \frac{2A}{M_s} k^2 + 4\pi M_s sin^2 \theta_k \right) \right]^{1/2} \tag{2.67}$$

where θ_k is the angle between k and M_S. Due to broken translational symmetry, for a thin film (of thickness d) this dispersion relation will be modified. Now let us assume that the Zeeman field is applied along the z-axis, the plane of the film and x-axis is normal to the direction of the film. Under this situation Damon and Eshbach calculated the dispersion relation for dipolar modes of this magnetic thin film[52]. They

found two kinds of modes: surface or Damon-Eshbach (DE) mode and volume mode. The surface modes can persist upto an angle (called the critical angle θ_c) *with respect to* the perpendicular direction of magnetization. The critical angle θ_c can be expressed as:

$$\theta_c = \tan^{-1}\sqrt{\frac{4\pi M_s}{H}} \tag{2.68}$$

The amplitude of the surface mode decays exponentially away from the surface and most of the power in this mode is distributed in the vicinity of the film surface (2.7(a)).The penetration depth (δ) decreases with the increase in θ and becomes exactly zero at $\theta=\theta_c$. At this angle the surface mode is localized strictly at the surface.

Penetration depth is also proportional to the wave vector along that direction[53]. If $k_y \rightarrow 0$ then the penetration depth $\delta \rightarrow \infty$, so the surface mode will transfer to Kittel mode. When the penetration depth will become comparable to the film thickness then DE mode will convert into bulk mode. If the surface mode propagates along the perpendicular direction of magnetization then the mode is known as magnetostatic surface wave (MSSW) mode. The dispersion relation of the MSSW mode is expressed[54] as (considering negligible anisotropy):

$$\omega_{DE} = \gamma[H(H + 4\pi M_s) + (2\pi M_s)^2(1 - e^{-2kd})]^{1/2} \tag{2.69}$$

At $k = 0$, the DE mode becomes

$$(\omega_{DE})_{k=0} = \gamma[H(H + 4\pi M_s)]^{1/2} \tag{2.70}$$

The above frequency is same as the frequency of Kittel mode or uniform mode.

At $k \rightarrow \infty$, the MSSW becomes

$$(\omega_{DE})_{k=\infty} = \gamma(H + 2\pi M_s) \tag{2.71}$$

The frequencies of MSSW always remain in between two frequency values as described by equations 2.71 and 2.72.

There is a manifold of volume or bulk modes. Along the thickness of the magnetic thin film each volume mode form standing spin wave pattern and each mode corresponds to a mode number. This mode has a degeneracy along the propagation direction perpendicular to $\boldsymbol{M}$. The degeneracy is lifted when $\boldsymbol{k}$ becomes parallel to $\boldsymbol{M}$. When $\boldsymbol{k}$ is perpendicular to $\boldsymbol{M}$ then volume mode becomes dispersion-less, while for other directions, negative dispersion is observed. When the direction of $\boldsymbol{M}$ and $\boldsymbol{k}$ are in same plane then the spin wave is called as backward volume magnetostatic

(BWVMS) mode and the dispersion of this mode[50, 54] is expressed as (considering negligible anisotropy):

$$\left(\frac{\omega_B}{\gamma}\right)^2 = H\left[H + 4\pi M_s\left(\frac{1-e^{-2kd}}{kd}\right)\right] \tag{2.72}$$

The negative slope of dispersion implies that the phase velocity and group velocity are in opposite direction. At $k \to 0$, the frequency of BWVMS becomes the same as that of Kittel mode (equation 2.71).

Now we will discuss about the forward volume magnetostatic (FWVMS) mode. This mode generates when the magnetization is along the perpendicular direction to the film and the propagation direction is in the plane of the film. In the long magnetostatic limit, the dispersion relation of the FWVMS mode can be expressed after neglecting anisotropy as

$$\left(\frac{\omega_F}{\gamma}\right)^2 = (H - 4\pi M_s)\left[H - 4\pi M_s\left(\frac{1-e^{-kd}}{kd}\right)\right] \tag{2.73}$$

Here, the exchange interaction is generally neglected. This is a valid approximation for the materials with a very weak exchange stiffness constant such as Yttrium Iron Garnet (YIG).

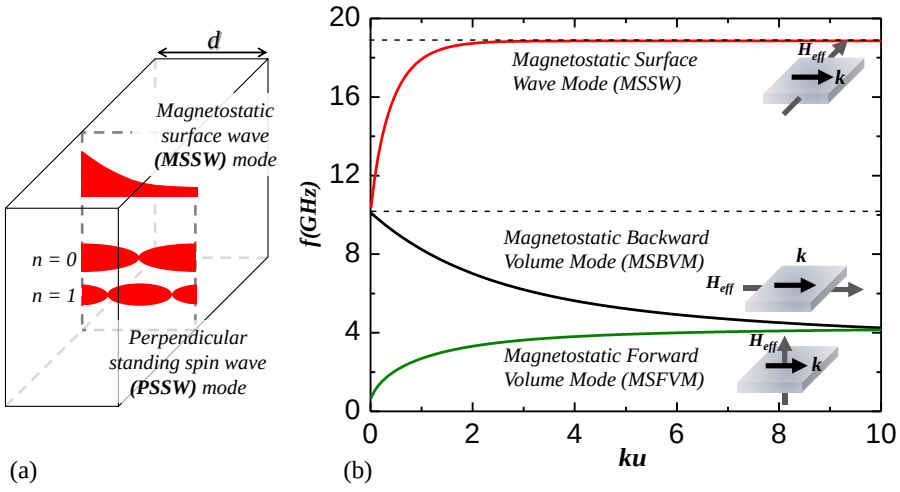

Figure 2.7: (a) Schematic diagram of PSSW and MSSW modes for a ferromagnetic thin film. (b) The dispersion curve of different magnetostatic spin wave modes.

2.7 Magneto-Optical Kerr Effect (MOKE)

In the year of 1845, Michael Faraday first observed that when a linearly polarized light propagated through a material, which is placed within a magnetic field applied along the propagation axis, then the polarization axis of the light was rotated. He noticed it in a piece of glass placed in between two magnetic pole pieces. This angle of rotation depended on the distance traveled in the medium and the strength of the applied field. This is the well-known Faraday Effect. This effect is also the first observed magneto-optical effect. Then in 1877 the same effect was found by John Kerr in reflection geometry through a polished metallic pole of an electromagnet. This phenomenon is called Kerr effect[55] and the corresponding rotation of plane of polarization is called as the Kerr rotation. These two effects are similar in their origins and both are linearly proportional to the magnetization. Both the effects are sensitive to the components of the magnetization that are parallel to the propagation direction of the light. After the discovery of this effect, magneto-optical Kerr effect (MOKE) is recognized as a very efficient technique to probe the magnetization dynamics at different time scales and can image the magnetic domains. In MOKE, the interaction between the ferromagnetic material and the linearly polarized light will produce an orthogonal component in the electric field vector of the reflected light both in-phase and out-of-phase to that of the reflected light. Both of these components contain some information *i.e.*, the in-phase component gives the information about the Kerr rotation whereas the out-of-phase component responsible for the Kerr ellipticity.

2.7.1 Physical Mechanism of Magneto-Optical Kerr Effect

The Zeeman effect in the theory of dispersion can explain the origin of the magneto-optical effect. In an oscillating electric field, if we consider a system of harmonically bound electrons with a static magnetic field along *z*-axis then the equation of motion for each electron will be expressed as:

$$m\ddot{\boldsymbol{r}} + b\dot{\boldsymbol{r}} + k\boldsymbol{r} = -e\boldsymbol{E_0}e^{j\omega t} - e\mu_0\dot{\boldsymbol{r}} \times \boldsymbol{H} \tag{2.74}$$

Where b is the damping coefficient and m is the electronic mass. $(k/m)^{1/2} = \omega_0$ is the natural frequency of the electron. The last term in this equation is the Lorentz force. This equation of motion can be solved easily. The amplitude of the electric dipole

moment ($-er_0$) is a linear function of electric field E_0. This proportionality tensor is known as the polarizability tensor. So for an assembly of N such oscillators the probability is,

$$\chi_{xx} = \chi_{yy} = \frac{Ne^2}{\epsilon_o m} \frac{\omega_0^2 - \omega^2 + j\omega\gamma}{(\omega_0^2 - \omega^2 + \omega\gamma)^2 - 4\omega^2\omega_L^2}$$
$$\chi_{xy} = -\chi_{yx} = \frac{Ne^2}{\epsilon_o m} \frac{-2j\omega\omega_L}{(\omega_0^2 - \omega^2 + \omega\gamma)^2 - 4\omega^2\omega_L^2} \quad (2.75)$$

Where $\gamma = b/m$ denotes the width of resonance and $\omega_L = e\mu_0 H/2m$ is the Larmor precession frequency. In an isotropic medium χ is symmetric and a scalar quantity. So the off-diagonal term of dielectric tensor will become zero. Anisotropy may be occurred in the medium from the magnetic field or the magnetization of the ferromagnetic material. The polarizability of a circularly polarized is expressed as[55]

$$\chi_{\pm} = \chi_{xx} \pm \chi_{xy} = \frac{Ne^2}{\varepsilon_0 m} \frac{(\omega_0^2 - \omega^2 + j\omega\gamma) \pm 2\omega\omega_L}{(\omega_0^2 - \omega^2 + j\omega\gamma)^2 - 4\omega^2\omega_L^2}$$
$$\approx \frac{Ne^2}{\varepsilon_0 m} \frac{1}{{\omega_0}^2 - (\omega \pm \omega_L)^2 + j\omega\gamma} \quad (2.76)$$

The upper sign refers to right-circularly polarized light (RCP) and the lower sign to the left circularly polarized light (LCP). According to Larmor's theorem in absence of magnetic field if the refractive index of the medium is denoted as $n(\omega)$ then in presence of a field the refractive index can be written as:

$$n_{\pm}(\omega) = n(\omega \pm \omega_L) \quad (2.77)$$

So if magnetic field is present then the refractive index of RCP and LCP will be different.

Now we will consider in a circularly birefringent medium a linearly polarized (polarization axis is along $+x$-axis) light is travelling along $+z$ direction then the electric field can be expressed as

$$E = \widehat{e_x} E_0 e^{j(\omega t - kz)} \quad (2.78)$$

Where k is the wave vector and ω is the angular frequency. In a non-birefringent medium the expression for the linearly polarized light will be a linear combination of RCP and LCP and the form will be:

$$E = \frac{E_0}{2}\left(\widehat{e_x} + j\widehat{e_y}\right)e^{j(\omega t - kz)} + \frac{E_0}{2}\left(\widehat{e_x} - j\widehat{e_y}\right)e^{j(\omega t - kz)} \tag{2.79}$$

For a circularly birefringent medium the above expression will be modified as

$$E = \frac{E_0}{2}\left(\widehat{e_x} + j\widehat{e_y}\right)e^{j\left(\omega t - \frac{2\pi n_+ z}{\lambda_0}\right)} + \frac{E_0}{2}\left(\widehat{e_x} - j\widehat{e_y}\right)e^{j\left(\omega t - \frac{2\pi n_- z}{\lambda_0}\right)} \tag{2.80}$$

where λ_0 is the wavelength of the linearly polarized light in vacuum. The above expression can also be written as

$$E = \frac{E_0}{2}e^{j(\omega t - \frac{2\pi \bar{n} z}{\lambda_0})}\left[\widehat{e_x}\cos\frac{\delta}{2} + \widehat{e_y}\sin\frac{\delta}{2}\right] \tag{2.81}$$

where

$$\bar{n} = \frac{1}{2}(n_+ + n_-) \tag{2.82}$$

and

$$\delta = \frac{2\pi(n_+ + n_-)z}{\lambda_0} \tag{2.83}$$

is the phase difference between the components by the birefringence of the medium. From equation 2.81 we can state that the direction of polarization of linearly polarized light is being rotated through an angle of $\delta/2$.

In an absorptive medium $n_\pm$ is a complex quantity and we can write it as

$$n_\pm = N_\pm - jK_\pm \tag{2.84}$$

where $n_\pm$ and $K_\pm$ are real quantities. In this case the linearly polarized light will be converted into an elliptically polarized light with the major axis of the ellipse rotated through an angle

$$\theta_k = \Re\left(\frac{\delta}{2}\right) = \Re\frac{\pi l}{\lambda_0}(n_+ - n_-) \tag{2.85}$$

where l is the distance of propagation.

The ellipticity is expressed as

$$\epsilon_k = -\tan\Im\left(\frac{\delta}{2}\right) = -\tan\Im\left[\frac{\pi l}{\lambda_0}(n_+ - n_-)\right] \tag{2.86}$$

2.7.2 Phenomenological Theory

The optical properties of materials are given by Maxwell's equation and the consecutive relations which express the specific material properties. The equations we need are:

$$\nabla \times \boldsymbol{E} = -\mu_0 \frac{\partial \boldsymbol{H}}{\partial t} \tag{2.87}$$

$$\nabla \times \boldsymbol{H} = \epsilon_0 \frac{\partial \boldsymbol{E}}{\partial t} + \boldsymbol{J} \tag{2.88}$$

Where $\boldsymbol{E}$, $\boldsymbol{H}$, $\boldsymbol{J}$, μ_0, ϵ_0 are electric field, magnetic field, electrical current density, permeability and permittivity, respectively. Now current density can be expressed as

$$\boldsymbol{J} = \varepsilon_o \frac{\partial \boldsymbol{P}}{\partial t} = \chi . \frac{\partial \boldsymbol{E}}{\partial t} \tag{2.89}$$

Where χ is the polarizability. The relation of dielectric constant (κ) and polarizability (χ) is as follows

$$\boldsymbol{k} = 1 + \boldsymbol{\chi} \tag{2.90}$$

$\boldsymbol{\kappa}$and $\boldsymbol{\chi}$ are the tensorial quantities and both depend on the applied magnetic field and magnetization of the material. Those quantities are non-scalar in nature and give rise to the magneto-optical effect. Now suppose a plane propagating wave propagating through a medium then the electric and magnetic fields can be expressed as

$$E = E_0 e^{j(\omega t - k.r)}, H = H_0 e^{j(\omega t - k.r)} \tag{2.91}$$

Taking curl of (2.87) and using (2.88) & (2.90), one can write

$$\left\{ n^2 1 - \frac{kk}{k_0^2} - k \right\} . E_0 = 0 \tag{2.92}$$

Equation 2.92 possesses a nontrivial solution for E_0 only if the determinant of coefficient vanishes. So far magneto-optical effect has not been explained so suppose a cubic crystal with dc magnetic field applied along the *z*-axis. Then, the dielectric constant can be written as a matrix

$$\boldsymbol{k} = \begin{bmatrix} k_1 & k_2 & 0 \\ -k_2 & k_1 & 0 \\ 0 & 0 & k_3 \end{bmatrix} \tag{2.93}$$

In the above matrix, k_2 is the odd function of $\boldsymbol{H}$ or $\boldsymbol{M}$, whereas k_1 and k_3 are even functions. From the matrix form of *k*, the secular determinant for equation2.92 becomes

$$\begin{aligned} & n^4\{k_1 + (k_3 - k_1)\cos\theta'^2\} \\ & \quad - n^2\{(k_1^2 + k_2^2 + k_1 k_3) - (k_1^2 + k_2^2 - k_1 k_3)\cos\theta'\} \\ & \quad + k_3(k_1^2 + k_2^2) = 0 \end{aligned} \tag{2.94}$$

where

$$\cos\theta' = \frac{k_z}{k} = \frac{k_z}{n k_0} \tag{2.95}$$

Now we will consider a homogeneous wave (real and imaginary part of $\boldsymbol{k}$ are parallel) with propagation direction along $\boldsymbol{H}$ or $\boldsymbol{M}$. In this case $\cos\theta' = 1$. So the solutions of (2.94) are

$$n_{\pm} = k_1 \pm jk_2 \tag{2.96}$$

For simplicity, we will now consider the polar Kerr effect at normal incidence. Let k_0, k_1 and k_2 are the incident, reflected and transmitted wave vectors, respectively. The reflected amplitude can be written as

$$r = \frac{E_1}{E_0} = -\frac{n-1}{n+1} \tag{2.97}$$

If the reflectivity will be expressed as

$$r = |r|e^{i\varphi} \tag{2.98}$$

Then

$$\frac{r_+}{r_-} = \left|\frac{r_+}{r_-}\right| e^{i(\varphi_+ - \varphi_-)} \tag{2.99}$$

The above relation implies that the linearly polarized light will be converted to elliptically polarized light due to reflection. This happens because the circular components (RCP & LCP) will have equal amplitudes. Due to the introduction of phase between two circular vibrations the major axis of the ellipse will be rotated from the original direction of polarization of the incident light. The Kerr rotation and ellipticity can be expressed as

$$\theta_k = \frac{1}{2}(\varphi_+ - \varphi_-) \tag{2.100}$$

And

$$\varepsilon_k = -\frac{r_+ - r_-}{r_+ + r_-} \tag{2.101}$$

Now, the complex Kerr rotation can be written as

$$\theta_k = \frac{2}{1-\epsilon}[-(k_- - k_+) + i(n_- - n_+)] \tag{2.102}$$

The real part of the complex Kerr rotation (θ_K) gives the Kerr rotation and imaginary part gives the Kerr ellipticity. The Kerr rotation depends upon the circular dichroism, whereas Kerr ellipticity depends upon the circular birefringence of the medium. It can also be shown qualitatively that the Kerr rotation and Kerr ellipticity both are proportional to the magnetization of ferromagnetic material.

Bibliography

[1] C. Kittel, "Introduction to Solid State Physics," *Seventh edition ed., Wiley India*, (2009).

[2] P. Wiess, *J. Phys. Rad.* **6**, 667 (1907).

[3] P. Curie, *Ann. Chim. Phys* **7**, 289 (1895).

[4] D. M. Kaufmann, "Magnetization Dynamics in All-optical Pump-probe Experiments: Spin-wave Modes and Spin-current Damping," P.hD Thesis, Georg-August-Universität (2006).

[5] H. A. Morrish, "The Physical Principles of Magnetism," *IEEE Press*, (2001).

[6] S. Chikazumi, "Physics of Ferromagnetism," *Oxford University Press*, (1997).

[7] J. Silcox, *Philos. Mag.* **8**, 7 (1963).

[8] T. Suzuki, *J. Phys. Colloques* **32**, C1 134 (1971).

[9] A. T. J. Milat and G. Albuquerque, "Spin dynamics in confined magnetic structures I," *Springer*, (2002).

[10] G. A. Gurevich and A. G. Melkov, "Magnetization Oscillations and Waves," *CRC Press*, (1996).

[11] D. L. Landau and M. E. Lifshitz, *Phys. Zs. der Sowjetunion.* **8**, 153 (1935).

[12] T. L. Gilbert, *Phys. Rev.* **100**, 1243 (1955).

[13] T. L. Gilbert, *IEEE Trans. Magn.* **40**, 3443 (2004).

[14] E. Beaurepaire, J. C. Merle, A. Daunois and J. Y. Bigot, *Phys. Rev. Lett.* **76**, 4250 (1996).

[15] B. Koopmans, "Handbook of Magnetism and Advanced Magnetic Materials " 3, *John Wiley & Sons Ltd.*, (2007).

[16] B. Koopmans, *Nat. Mater.* **6**, 715 (2007).

[17] L. Guidoni, E. Beaurepaire and J.-Y. Bigot, *Phys. Rev. Lett.* **89**, 017401 (2002).

[18] P. M. Oppeneer and A. Liebsch, *J. Phys.:Condens. Matter.* **16**, 5519 (2004).

[19] B. Koopmans, J. J. M. Ruigrok, F. D. Longa and W. J. M. de Jonge, *Phys. Rev. Lett.* **95**, 267207 (2005).

[20] E. Carpene, E. Mancini, C. Dallera, M. Brenna, E. Puppin and S. De Silvestri, *Phys. Rev. B* **78**, 174422 (2008).

[21] M. Krauß, T. Roth, S. Alebrand, D. Steil, M. Cinchetti, M. Aeschlimann and H. C. Schneider, *Phys. Rev. B* **80**, 180407 (2009).

[22] G. P. Zhang, W. Hubner, G. Lefkidis, Y. Bai and T. F. George, *Nat. Phys.* **5**, 499 (2009).

[23] J.-Y. Bigot, M. Vomir and E. Beaurepaire, *Nat. Phys.* **5**, 515 (2009).

[24] G. P. Zhang and W. Hübner, *Phys. Rev. Lett.* **85**, 3025 (2000).

[25] E. Beaurepaire, G. M. Turner, S. M. Harrel, M. C. Beard, J.-Y. Bigot and C. A. Schmuttenmaer, *Appl. Phys. Lett.* **84**, 3465 (2004).

[26] M. Battiato, K. Carva and P. M. Oppeneer, *Phys. Rev. Lett.* **105**, 027203 (2010).

[27] A. Laraoui, V. Halté, M. Vomir, J. Vénuat, M. Albrecht, E. Beaurepaire and J. Y. Bigot, *Eur. Phys. J. D* **43**, 251 (2007).

[28] A. Laraoui, J. Vénuat, V. Halté, M. Albrecht, E. Beaurepaire and J. Y. Bigot, *J. Appl. Phys.* **101**, 09C105 (2007).

[29] B. koopmans, G. Malinowski, F. Dalla Longa, D. Steiauf, M. Fahnle, T. Roth, M. Cinchetti and M. Aeschlimann, *Nat. Mater.* **9**, 259 (2010).

[30] J. Griffiths, *Nature* **158**, 670 (1946).

[31] C. Kittel, *Phys. Rev.* **73**, 155 (1948).

[32] F. Goedsche, *Physica Status Solidi B* **39**, 1 (1970).

[33] J. Gouzerh, A. A. Stashkevich, N. G. Kovshikov, V. V. Matyushev and J. M. Desvignes, *J. Magn. Magn. Mater.* **101**, 189 (1991).

[34] Y. I. Gorobets and S. A. Reshetnyak, *Tech. Phys.* **43**, 188 (1998).

[35] A. V. Vashkovskii and E. H. Lokk, *Phys.Usp.* **47**, 601 (2004).

[36] S.-K. Kim, S. Choi, K.-S. Lee, D.-S. Han, D.-E. Jung and Y.-S. Choi, *Appl. Phys. Lett.* **92**, 212501 (2008).

[37] V. E. Demidov, S. O. Demokritov, D. Birt, B. O'Gorman, M. Tsoi and X. Li, *Phys. Rev. B* **80**, 014429 (2009).

[38] P. A. Fleury, S. P. S. Porto, L. E. Cheesman and H. J. Guggenheim, *Phys. Rev. Lett.* **17**, 84 (1966).

[39] S. Choi, K.-S. Lee and S.-K. Kim, *Appl. Phys. Lett.* **89**, 062501 (2006).

[40] V. K. Dugaev, P. Bruno, B. Canals and C. Lacroix, *Phys. Rev. B* **72**, 024456 (2005).

[41] D. R. Birt, B. O'Gorman, M. Tsoi, X. Li, V. E. Demidov and S. O. Demokritov, *Appl. Phys. Lett.* **95**, 122510 (2009).

[42] E. Vilkov, *Phys. Solid State* **48**, 1754 (2006).

[43] D. D. Stancil, B. E. Henty, A. G. Cepni and J. P. Van't Hof, *Phys. Rev. B* **74**, 060404 (2006).

[44] V. Vlaminck and M. Bailleul, *Science* **322**, 410 (2008).

[45] F. J. Dyson, *Phys. Rev.* **102**, 1217 (1956).

[46] T. Holstein and H. Primakoff, *Phys. Rev.* **58**, 1098 (1940).

[47] C. Rüegg, A. Furrer, D. Sheptyakov, T. Strässle, K. W. Krämer, H. U. Güdel and L. Mélési, *Phys. Rev. Lett.* **93**, 257201 (2004).

[48] S. O. Demokritov, V. E. Demidov, O. Dzyapko, G. A. Melkov, A. A. Serga, B. Hillebrands and A. N. Slavin, *Nature* **443**, 430 (2006).

[49] Y. M. Bunkov and G. E. Volovik, *J. Low Temp. Phys.* **150**, 135 (2008).

[50] S. O. Demokritov, B. Hillebrands and A. N. Slavin, *Phys. Rep.* **348**, 441 (2001).

[51] C. Herring and C. Kittel, *Phys. Rev.* **81**, 869 (1951).

[52] R. W. Damon and J. R. Eshbach, *J. Phys. Chem. Solids* **19**, 308 (1961).

[53] P. A. Grünberg, *Prog. Surf. Sci.* **18**, 1 (1985).

[54] B. Hillebrands and J. Hamrle, "Handbook of Magnetism and Advanced Magnetic Materials," *John Wiley & Sons, Ltd.*, (2007).

[55] M. J. Freiser, *IEEE Trans. Magn.* **4**, 152 (1968).

Chapter 3

Fabrication and Characterization Techniques

3.1 Introduction

Nanofabrication is the basis of nanoscience and nanotechnology. Fabrication of high quality nanostructure is most important for nanodevices. Nanostructures should be identical in shape and monodisperse in size in an ordered array fabricated over macroscopic length scale. The intrinsic static and dynamic magnetic properties significantly depend on the material property *i.e.*, crystallinity, chemical purity and as well as the chemical uniformity of the nanostructure. In case of fabrication one hurdle is the development of cost effective fabrication techniques with a high yield.Various fabrication techniques have been developed to prepare high quality magnetic nanostructures.All of them are not able to produce good quality ordered nanostructures. However, good quality samples are always needed for scientific research, because sample quality plays an important role in the intrinsic properties of material. Depending upon the requirement, different techniques are used for the sample fabrication for different measurements. Also, all the physical properties of the nanostructures need to be studied thoroughly before any application. Among all of them lithographic methods are found to be the best option for precise fabrication of high quality samples in spite of being a slow and expensive method. The nanostructure then should be characterized and after a satisfactory characterization, the samples are used for investigating the ultrafast magnetization dynamics. In this chapter, some important fabrication and characterization techniques are discussed, which were used in the work presented in this thesis[1].

3.2 Fabrication

3.2.1 Optical Lithography

Lithography is a process of patterning fine-scale structures onto a substrate. Generally this system uses radiation to expose the recording medium, known as resist. Different kinds of lithography techniques have been developed over the last few decades based

on the type of exposure radiation such as optical, electron beam, X-ray and ion beam lithography. These lithographic techniques are widely used for fabrication of ordered arrays of nanostructures efficiently and precisely. Optical lithography is composed of four fundamental elements such as (i) illumination system with energy source, (ii) mask containing the pattern to be fabricated, (iii) exposure system to generate an aerial image of the mask pattern and (iv) a medium known as 'photoresist' or resist for recording the image generated by the exposure system. There is a parallel growth of all the nanostructure using photo-mask reducing the fabrication time significantly. Optical lithography has a drawback that it is difficult to fabricate sub-micron nanostructure using this technique due to the resolution limitation by the diffraction of light.

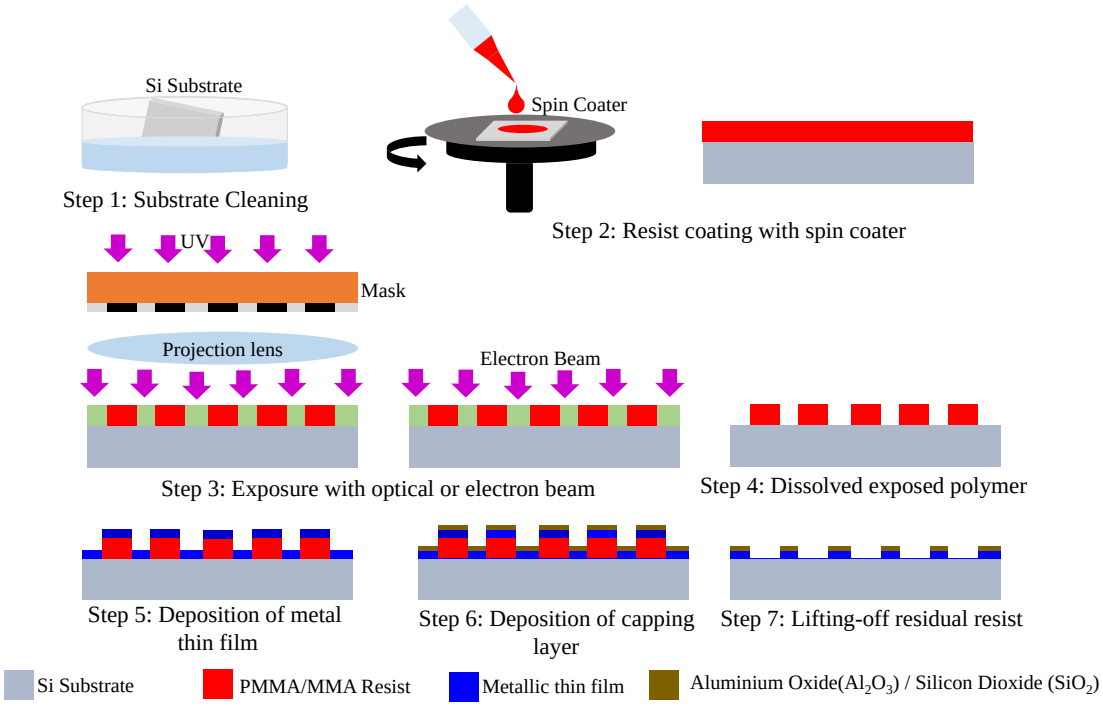

Figure 3.1: Schematic diagram of optical and electron beam lithography.

In our case we have used mask-less photolithography, D-light-DL1000RS Mask-less UV Lithography system where digital mirror devices control the position of laser to fabricate 10 × 10 μm^2 ferromagnetic (Co / $Ni_{80}Fe_{20}$) blanket film[2-4], co-planar waveguide and positioning mark for e-beam lithography. First of all, the Si (100) substrate with a 300 nm silicon-oxide coating was cut into appropriate size, *e.g.*, squares with 20 mm sides and then it was cleaned to remove all the contaminations of inorganic and organic materials before the lithography process is performed. The cleaning process includes three steps. Firstly, the substrates are soaked in acetone and

an ultrasonic bath is used to clean it for 10 min with high power and followed by drying them with a Nitrogen (N_2) gun. Then the substrates are soaked into isopropanol (IPA) and ultrasonicated for more 10 min with high power to remove the residual acetone followed by drying process with N_2 gun. Finally, ultraviolet cleaning of the substrates were performed for 10 min to remove remaining organic materials from the surface.

At first a layer of primer (Figure. 3.1) (1,1,1,3,3,3,-Hexamethyldisilazane, $C_6H_{10}NSi_2$, HDMS) is spin coated at 500 rpm for 5 sec and then 5000 rpm for 40 sec on the cleaned substrate. The substrate is then soft baked in an oven at 80 °C for 5 min. Then a positive photoresist (AZ-1500) is spin-coated on top of the substrate with a 500 rpm for 5 sec and then 5000 rpm for 40 sec. Care is taken to ensure that the photoresist spreads uniformly over the whole surface of the substrate. The substrate is then baked in an oven at 80 °C for 10 min. This process removes the solvent in the photoresist and enhances the adhesion between the photoresist and the substrate. The thickness of the photoresist layer is adjusted to about one micron depending upon the viscosity of the resist and the spinning speed[5]. Then the laser beam is exposed on the substrate surface with a typical energy of 90 mJ/mm^2 to draw the patterns onto the surface. The last step of the UV photolithography process is the development of the exposed substrate. The substrate is developed in developer solution for 50-60 sec followed by a rinsing process in DI water for about 1 min. Finally the substrate is dried off using N_2 gun. Subsequently, the two dimensional pattern was copied onto the resist as a three dimensional structure. This technique provides a fast and simple method to prepare micro-scale patterns on a thick resist layer.

In this thesis all the 10 × 10 μm^2 ferromagnetic blanket thin films and co-planar waveguides are fabricated using this mask-less UV photolithography process.

3.2.2 Electron Beam Lithography (EBL)

Electron beam lithography (EBL) is the second patterning technique used in this thesis. The EBL technique uses an electron beam to expose an electron-sensitive resist to write patterns on the substrate. The resolution of EBL is much higher than that for

optical lithography due to the thinner resist thickness (few nanometer order) and shorter wavelength (on the order of 0.01 nm) of the high energy (keV range) electron beam used in the EBL technique. This gives the possibility to form nanoscale patterns on the EBL resist, which is sensitive to e-beam similar to photo-mask. The basic principle of EBL is very similar with optical lithography. Here, firstly the pre-cleaned substrate is coated with a bi-layer of EBL resist. First a bottom layer of thick 950 PMMA A4 (polymethyl methacrylate) positive photoresist layer is spun onto the substrate at a speed of 5000 rpm for 40 sec and baked at 180 °C for 90 sec. Then the second layer of resist MMA EL9 (methyl methacrylate) is spun at 1500 rpm for 90 sec followed by baking process at 180 °C for 90 sec. The reason behind using a bi-layer resist onto the substrate is to get an undercut edge profile of the resist after development of the pattern onto it. This is because the PMMA layer is developed faster than the MMA layer forming an overhung structure. The e-beam writing process will then be carried out in ELS-7700H (Elionix Inc.) EBL system. A computer aided design (CAD) system is used to prepare the pattern and to control the writing process of the EBL system. The system subsequently scans the drawing regions or patterns with the accelerated e-beam with pre-defined parameters. After e-beam writing, the resist is then developed in water for 1 min and then in IPA diluted MIBK (1:3) solvent for 30 seconds. The substrate is finally rinsed in IPA to remove the remaining developer.

The mask-less feature and high resolution of the EBL technique provide us more freedom to control the experiment. The main disadvantage of this technique is the long processing / writing time compared to the exposure time in other lithographic technique. In this thesis, the electron beam lithography system has been used to prepare array of antidot arranged in different lattice symmetries below the co-planar waveguide (CPW).

3.2.3 Focused Ion Beam (FIB) Lithography

FIB lithography is an efficient technique[6] of ion beam milling for fabricating nano-patterned sample. In ion beam milling, a beam of ions is accelerated and collides with the atoms on a substrate surface under processing. If the beam is sufficiently

energetic, these collisions cause the ejection or sputtering of the atoms from the surface through momentum transfer, resulting in the removal or milling of the material. The ion beam can be easily focused down to a narrow size, using electromagnetic lenses, as small as few nanometers. Once focused, it can also be scanned across a surface with great precision. Hence, focused ion beams can be controlled to mill any computer-defined pattern on a film directly without the need of resists or masks.

In this thesis[2, 4] we have used two different types of ion milling systems. We have used FEI Helios Nanolab™ 600 dual Beam (FIB/ SEM) system to fabricate array of antidots. This system is composed with an extremely high resolution Elstar™ electron column with a Field Emission Gun (FEG) electron source. The capabilities of the FIB for small probe (diameter ~ 5 nm) sputtering are achieved by the liquid metal ion source (LMIS). In this system Ga^+ ion is used as LMIS due to the following advantages including (i) low melting point, (ii) low volatility, (iii) low vapor pressure, (iv) excellent electrical, mechanical and vacuum properties and (v) emission characteristics enabled high angular intensity with a small energy speed. For patterning, we have mounted the sample on the stage and inserted into the chamber. The chamber is then evacuated. Inside the chamber electron pole is placed vertically *with respect to* the chamber but the ion pole is tilted at an angle of 45°to the electron pole/chamber [Figure. 3.2(a)]. When the vacuum is reached to the desired level inside the chamber, the sample stage is tilted to 52° [Figure. 3.2(b)] in steps to reach the eucentricpoint which is basically a particular stage height where the sample image does not move if the stage is tilted. After all this adjustment, the electron and ion source voltages are turned on and the milling process is started. In our case we have used 30 kV voltage and 28 pA beam current for our fabrication presented in this thesis. These parameters are optimized after several test runs. A particular portion of the sample is identified first where the patterning will be done and then it is scanned by the Ga^+ ions. The desired pattern is drawn by varying the X, Y and Z coordinates.

Here the Z coordinate controls the thickness of milling. In FIB ion beam spot size is an important parameter which is also a function of beam current and it need to be optimized not only for creating the repetitive nano-patterns with high fidelity but also to ensure that the material that has been retained after patterning does not have

excessive Ga^+ ion- implantations. Two types of damage may occur in the substrate during the milling process, one is the direct damage that affects the edges of the antidots due to direct beam of finite width and another is the struggling of the ion beam that may cause lateral implantation in the bulk of the film/substrate along the edges.

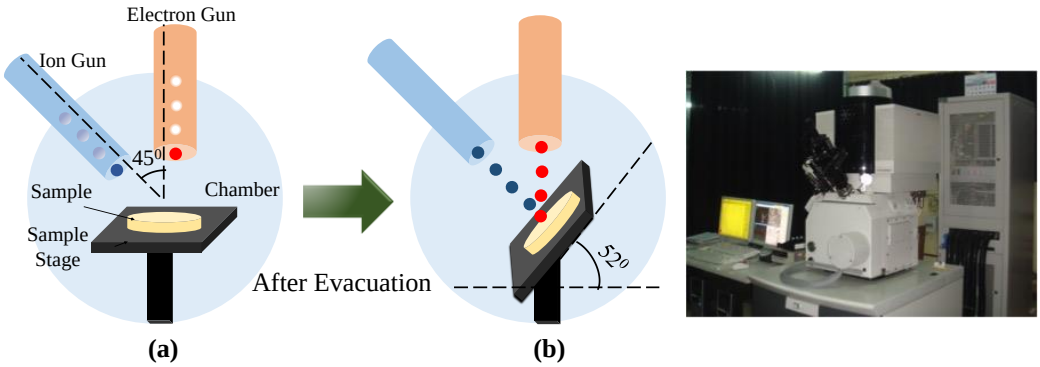

Figure 3.2: Arrangement of the electron gun, ion gun and sample in the chamber (a) before and (b) after the evacuation and the photographs of FIB system in S. N. Bose National Centre for Basic Sciences.

In this thesis[2] the array of antidots with diameter of 100 nm having different lattice constants and different antidot shapes were fabricated using this FIB system.

We have used another ion milling system to fabricate array of antidots arranged in different lattice symmetries. For that purpose we have used Hakuto-NS Argon Ion Milling system. Here the substrate is placed on a rotatable stage inside a vacuum chamber at desired pressure. The sample stage should be placed parallel with the ion source. In presence of argon (Ar) gas the filament starts to dissipate accelerated electrons and it helps to milling process of the substrate. The substrate is rotated on the stage so that the milling should be uniform at all the desired positions where patterning should be done.

3.3 Thin Film Deposition Technique

Lithography technique helps us to fabricate array of nanoscale patterns on the resist, which we have discussed in the previous section. In this section we will focus on the

deposition technique, which we have used to transfer resist pattern to ferromagnetic structures in my thesis. In our case we have used e-beam evaporation system. Here we will discuss about this system followed by the lift-off process for the thin film.

3.3.1 Electron-Beam Evaporation

Eiko ultrahigh vacuum film deposition system was used for ferromagnetic thin film deposition. A load-locked chamber is integrated with the system to transfer samples into the chamber. Electron beam evaporation is the similar process to thermal evaporation *i.e.*, a source material is heated above its boiling/sublimation temperature and evaporated to form a film on the surface of the substrate.

The substrate is loaded on a sample holder, which is mounted with a rotation motor. In order to obtain spatially uniform thin film, the substrate is rotated during the deposition process. The e-beam evaporation can be used to melt both ferromagnetic materials (such as Co, $Ni_{80}Fe_{20}$ and Fe) and nonmagnetic material (such as Au, Ti, Al_2O_3). The different e-beam pockets are fixed on top of a train in which the position can be adjusted from outside without breaking the vacuum in the chamber. Due to the long distance (about 15-20 centimeter) between the substrate and the source, the evaporated material can be considered as deposited on the substrate perpendicularly. This is very important for the deposition of the film on the arrays of structures as it reduces the undesired side-wall coating during the deposition. The lift-off process becomes easy as the solvent can seep easily into the resist layer.

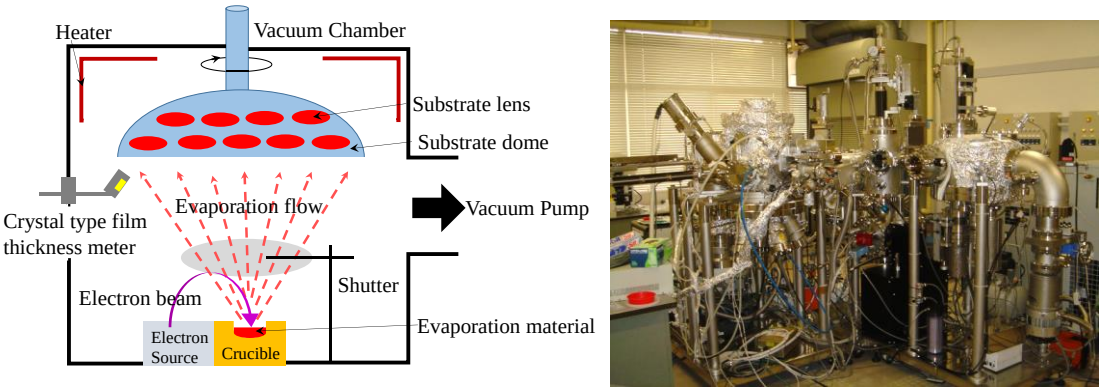

Figure 3.3: Schematic diagram of electron beam evaporation system and the photographs of the deposition system in RIKEN, Japan.

3.3.2 Lift-Off Process

In order to remove excessive magnetic materials from the top of the resist layer, the lift-off process was performed after the deposition process. The substrate is first soaked in a resist soluble solvent like acetone. The substrate is then placed in an ultrasonic bath to assist the removal of resist after immersion in the solution. At last the IPA and DI water rinsing process is performed to clean the substrate after resist removal. SEM imaging is used to verify the lift-off completion. The nanostructure fabrication process is completed after the lift-off process.

3.4 Characterization Techniques

Scanning Electron Microscope (SEM) and Atomic Force Microscope (AFM) was used to characterize the morphology of the fabricated structures. To study the magnetic properties we have used Vibrating Sample Magnetometer (VSM) and Static Magneto-Optical Kerr Effect microscope (SMOKE). Now we will discuss about the above-mentioned characterization techniques except the SMOKE, which we will discuss in next chapter (Chapter 4).

3.4.1 Scanning Electron Microscope (SEM)

Scanning Electron Microscope (SEM) is one of the most popular and commonly used tools for imaging structures ranging from millimeter to nanometer scale[7, 8]. In a typical SEM the stream of electron is emitted from the cathode either by thermionic emission or by electric field. In thermionic emission electron is emitted from an electron gum fitted with a tungsten filament cathode but for field emission there will be a field emission cathode. The second process helps to get better spatial resolution than the first process as it produces narrower beam profile. The energy of the electrons can be varied from few hundreds eV to few tens of keV. After emission, in presence of electric field the electrons get accelerated. The beam goes through two electromagnetic lenses, called condenser lenses (Figure. 3.4). At the end the beam passes through an electromagnetic scanning coil and is focused onto the sample[8]. When deflected by the scanning coil in the X and Y directions (*i.e.*, in the plane of the sample), the beam scans over a rectangular area of the sample surface in a raster fashion. After the interaction of high energetic electron beam with the sample,

different types of electrons including secondary electrons, backscattered electrons and Auger electrons are emitted or scattered from the sample due to the elastic and inelastic collision of accelerated electrons with the electrons present near the sample surface In a typical SEM, the secondary electrons are detected by a detector. The intensity of the secondary electrons is compared with the primary electron beam and the image is constructed which is displayed on a monitor.

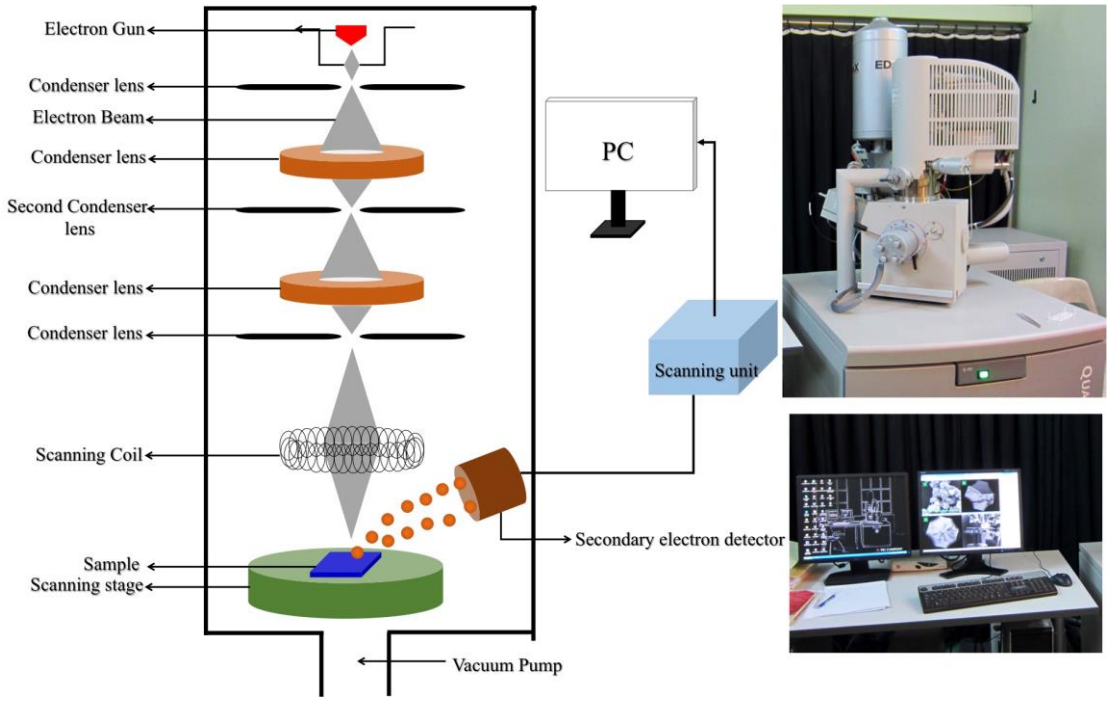

Figure 3.4: Schematic diagram of Scanning Electron Microscope (SEM) and the photographs of SEM in S. N. Bose National Centre for Basic Sciences.

In SEM, due to narrow electron beam the image is formed with large depth of field. Hence, SEM is capable of producing three-dimensional images, which are very useful for understanding the surface structure of a sample. The sample is mounted on a specimen stub with the help of carbon tape so that it will be electrically conductive at the surface and electrically grounded to prevent the accumulation of electrostatic charge at the surface. For our sample characterization we have used “FEI QUANTA 200” and “FEI Helios NanoLab 600” system

3.4.2 Energy Dispersive X-ray (EDX) Analysis

Energy Dispersive X-ray (EDX) analysis is a very powerful tool for elemental analysis or chemical characterization of a sample. In this technique, the sample is stimulated by a high energy beam of charged particles like electrons, protons or sometimes X-rays. At the ground state, every atom contains a number of electrons moving around the nuclei in different shells. The incident charged particles eject out electrons from an inner shell creating a hole. Consequently, electrons from outer shell (with higher energy) jump to the inner shell to fill up the hole and the difference of energy is radiated in the form of X-ray. Since the atomic structure of each element is unique, the energy of the emitted X-rays, which is basically the characteristics of an element's atomic structure is also unique in nature. The energy and number of the X-ray are measured by an energy dispersive spectrometer, which is a Si (Li) detector. The energy values give the identification of elements and the relative heights of the peaks give the atomic percentage of the element. In general the EDX spectrometer is attached to SEM. We have usedan EDX spectrometer from EDAX attached with "FEI QUANTA 200" SEM.

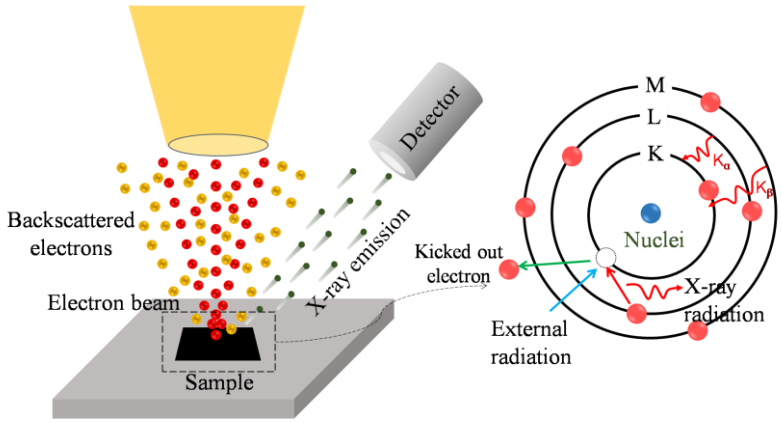

Figure 3.5: Interaction of accelerated electrons with sample and emission of X-rays is shown schematically.

3.4.3 Vibrating Sample Magnetometer (VSM)

Vibrating Sample Magnetometer (VSM) is used to measure the variation of magnetic moment or magnetization (*M*) as a function of applied magnetic field (*H*) or temperature[9]. According to Faraday's law, the change in magnetic flux through a coil

will induce an electromotive force (*emf*) in the coil and mathematically it can be expressed as,

$$\mathrm{E}_{in} = -na\frac{dB}{dt} \tag{3.1}$$

where $\mathrm{E_{in}}$ is the induced *emf*, *a* is the area of coil and *n* is the number of turns in the coil.

Using $\boldsymbol{B} = \boldsymbol{H} + 4\pi\boldsymbol{M}$, we get:

$$\mathrm{E}_{in} = -na\left(4\pi\frac{dM}{dt}\right) \tag{3.2}$$

if $\boldsymbol{H}$ remains unchanged.

Now, if the initial *M* is negligible than the induced magnetization, then the induced *emf* will be proportional to the magnetization of the sample:

$$\mathrm{E}_{in}dt = -na(4\pi M) \tag{3.3}$$

The working principle of VSM is based on the above law. The schematic diagram of the system is shown in Figure. 3.6. Static magnetic properties are measured with this system. The sample is placed inside a uniform magnetic field produced by two pole pieces of an electromagnet (Figure. 3.6). A vertical nonmagnetic plastic/quartz rod is used to mount the sample, which is connected with a piezoelectric transducer assembly located above the magnet. The sinusoidal electric signal generated by an oscillator/amplifier is converted in sinusoidal vertical vibration of the sample rod by the transducer.

As a result, the sample starts to oscillate with the rod in presence of the magnetic field and a voltage proportional to the magnetic moment of the sample will be induced in the stationary pick-up coils located in between the pole pieces. However, this voltage does not depend on the strength of the applied magnetic field, as the magnetic field is stationary. The induced voltage measured through a lock-in-amplifier using the output of the piezoelectric signal as its reference signal. The *M-H*curve of a ferromagnetic material is obtained by measuring the induced voltage as a function of magnetic field (*H*) of an electromagnet.

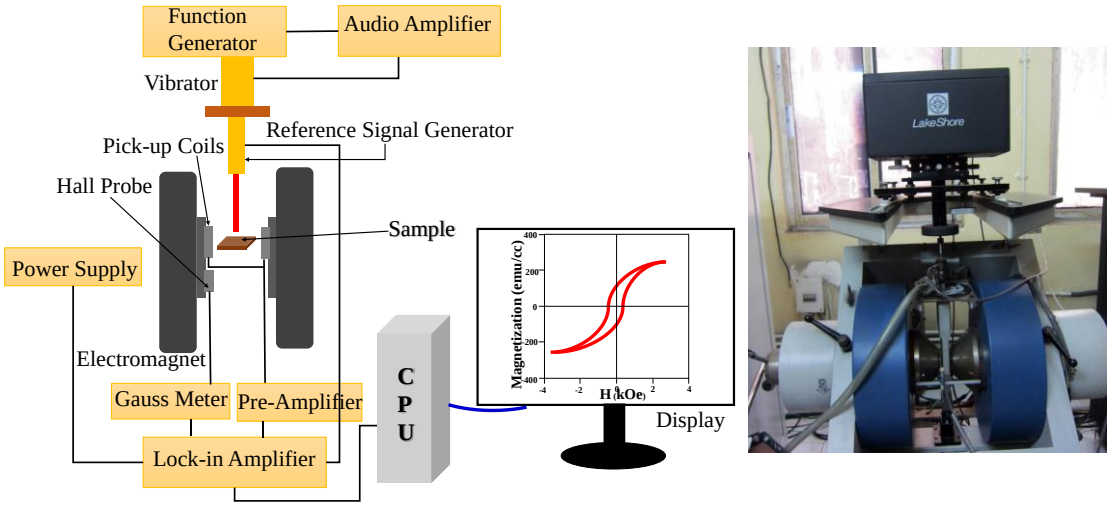

Figure 3.6: Schematic diagram of Vibrating Sample Magnetometer (VSM) with the photograph of VSM in S. N. Bose National Centre for Basic Sciences.

3.4.4 Atomic Force Microscope (AFM)

Atomic force microscope is a high resolution (~ 10 nm) scanning probe microscope[10]. It is basically used to see the topographical image of the surface of any material. A typical AFM consists of a very tiny sharp tip at the end of a cantilever (Figure. 3.7). The cantilever is made of Si or SiN (Silicon Nitride), which has a very low spring constant. The sharp tip with radius of curvature of few nanometersis fabricated usingsemiconductor-processing techniques. The cantilever does a scanning process over the surface in backward and forward movements of the tip. When the tip approaches the sample surface, different types of forces *viz.*, van der Waals forces, capillary and adhesive forces and double layer forces are exerted on the tip. However, van der Waals force is most commonly associated with AFM. The force exerted on the tip varies with the difference in thesurface heightand thus leads to the bending or deflection of the cantilever. According to Hooke's law, the bending is proportional to the force on the tip.To measure the bending or deflection a laser beam is reflected from the top surface of the cantilever head into an array of position sensitive photodiodes. When there is a change in the deflection of the cantilever due to the change in interaction force, the reflected laser beam is also deflected. This causes a change in the signal of the photodiode. The sample is mounted on a piezoelectric tube, which can move the sample in the *z* direction for maintaining a constant force, and the

x and *y* directions for scanning the sample. A feedback mechanism is employed from photodiode to piezoelectric tube to adjust the tip-to-sample distance to maintain a constant force between the tip and the sample.

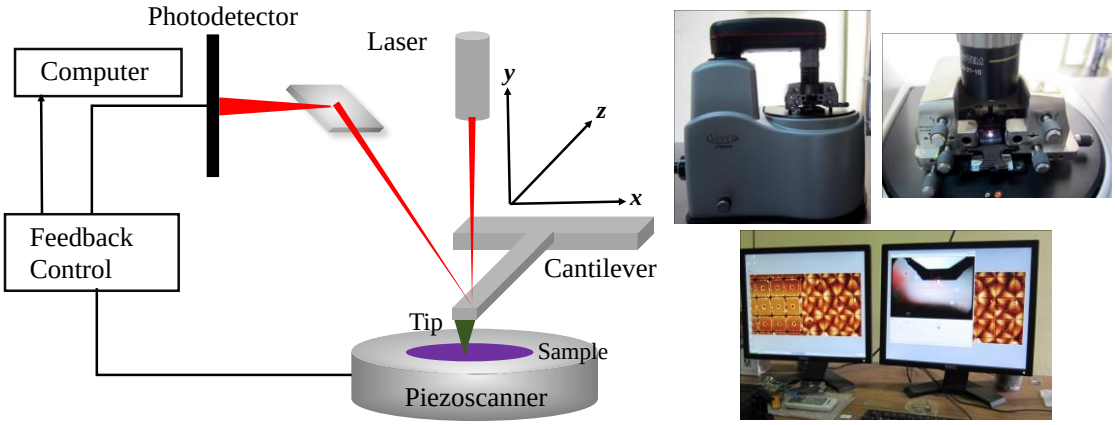

Figure 3.7: Schematic diagram and photographs of Atomic Force Microscope (AFM) in S. N. Bose National Centre for Basic Sciences.

Primarily, there are three modes of operation: contact mode, non-contact mode and tapping mode. Contact mode or repulsive mode is the simplest mode of operation for AFM. This mode of operation involves sideways scanning by the cantilever tip over the sample surface. The tip utilizes repulsive van der Waals force with the sample and the scanner gently traces the tip across the sample. However, contact mode yields very low resolution with large soft samples. In the non-contact mode, the tip experiences an attractive van der Waals force. The cantilever is oscillated at its resonant frequency, where the amplitude of oscillation is typically a few nanometers (< 10 nm) down to a few picometers[11]. The van der Waals forces, which are strongest from 1 nm to 10 nm above the surface, or any other long range force, which extends above the surface acts to decrease the resonance frequency of the cantilever. This decrease in resonant frequency combined with the feedback loop system maintains a constant oscillation amplitude or frequency by adjusting the average tip-to-sample distance. Measuring the tip-to-sample distance at each (*x*,*y*) data point allows the scanning software to construct a topographic image of the sample surface. In tapping mode, the cantilever is driven to oscillate up and down at near its resonance frequency by a piezoelectric element mounted in the AFM tip holder similar to non-contact mode. However, the amplitude of this oscillation is greater than 10 nm, typically 100

to 200 nm. The interaction forces acting on the cantilever when the tip comes close to the surface such asvan der Waals forces, dipole-dipole interactions, electrostatic forces, *etc*., cause the amplitude of this oscillation to decrease or phase to be changed as the tip gets closer to the sample. An electronic servo uses the piezoelectric actuator to control the height of the cantilever above the sample to maintain a set cantilever oscillation amplitude or phase as the cantilever is scanned over the sample.

Bibliography

[1] B. Rana and A. Barman, *SPIN* **3**, 1330001 (2013).

[2] R. Mandal, S. Saha, D. Kumar, S. Barman, S. Pal, K. Das, A. K. Raychaudhuri, Y. Fukuma, Y. Otani and A. Barman, *ACS Nano* **6**, 3397 (2012).

[3] A. O. Adeyeye and N. Singh, *J. Phys. D: Appl. Phys.* **41**, 153001 (2008).

[4] R. Mandal, P. Laha, K. Das, S. Saha, S. Barman, A. K. Raychaudhuri and A. Barman, *Appl. Phys. Lett.* **103**, 262410 (2013).

[5] J. I. Martín, J. Nogués, K. Liu, J. L. Vicent and I. K. Schuller, *J. Magn. Magn. Mater.* **256**, 449 (2003).

[6] L. A. Giannuzzi and F. A. Stevie, *Micron* **30**, 197 (1999).

[7] O. C. Wells, "Scanning Electron Microscopy," *McGraw-Hill*, (1974).

[8] D. McMullan, *Scanning* **17**, 175 (1995).

[9] S. Foner, *Rev. Sci. Instrum.* **30**, 548 (1959).

[10] G. Binnig, C. F. Quate and C. Gerber, *Phys. Rev. Lett.* **56**, 930 (1986).

[11] L. Gross, F. Mohn, N. Moll, P. Liljeroth and G. Meyer, *Science* **325**, 1110 (2009).

Chapter 4

Experimental Measurement Techniques for Magnetization Dynamics

4.1 Introduction:

Magneto-optical Kerr (MOKE) effect is a very old and well-known phenomenon. Since 1877[1], this technique has been efficiently used to measure magnetic hysteresis loop and images of magnetic domains. Later different types of MOKE configuration have been developed in the static and dynamic regimes[2, 3]. In 1991 the first time-resolved MOKE measurements were performed by Freeman et al.[4] and after that lot of important developments in time-resolved MOKE measurements is reported such as introduction of time-resolved scanning Kerr microscope[5], all-optical time-resolved MOKE for measurement of ultrafast demagnetization[6] and coherent spin waves[7], application of time-resolved Kerr effect measurements to samples fabricated on opaque substrate[8, 9], time-resolved cavity enhanced MOKE measurements[10] and more recently a bench-top time-resolved Kerr magnetometer[11, 12]. Within a few years, the time-resolved MOKE has become a very powerful and versatile technique for a non-invasive excitation and probing of ultrafast magnetization dynamics of magnetic thin films, multilayers, arrays of magnetic nanostructures, magnetic nanoparticles and magnetic nanowires in the time-domain with an excellent spatio-temporal resolution and measurement sensitivity.

4.2 MOKE Geometries:

Magneto-Optical Kerr Effect (MOKE) can be categorized by three different geometries, namely the longitudinal, transverse and polar geometries depending upon the direction of the magnetization vector *with respect to* the reflecting surface and the plane of incidence[12].

When the magnetization (***M***) is perpendicular to the reflection surface and parallel to the plane of incidence the effect is called the polar Kerr effect. In contrary, for longitudinal geometry ***M*** lies parallel to the reflection surface and the plane of

incidence. The Kerr rotation can be qualitatively described by considering the interaction of the electric filed (***E***) of the light with the magnetization of the material[2, 13]. In a linearly polarized light (let say *p*-polarized), the electrons in the sample oscillate along the *E*-field of the light. For a *p*-polarized light the oscillation will be in the plane of incidence of the beam and also in the plane of the sample. So, a regularly reflected light experiences a π phase change *with respect to* the incident beam. Therefore, the direction of ***E*** becomes opposite to the direction of the electric field. The Lorentz force on the oscillating electrons (R_k = **-m** × ***E***) (Figure. 4.1 (b)) generates an additional small vibrational component perpendicular to the plane of incidence[2].

The vector sum of original electric field vector and Lorentz field produces the electric field of the reflected light. Figure 4.1 (b) shows that the vector sum of the reflected lights *i.e.*, the resultant electric field of reflected light is rotated due to interaction with the magnetization of the sample. *S*-polarized light (electric field is perpendicular to the plane of incidence) gives similar Kerr rotation for the polar Kerr effect. At normal incidence the cross product of **m** and ***E*** is zero so, no longitudinal Kerr effect is observed. For other incidence angles for both *p*- and *s*-polarized lights longitudinal Kerr effect is observed. The Kerr rotation (θ_k) and ellipticity (ε_k) are related to each other by a relation: $\theta_k + i\varepsilon_k = k/r$, in the limit $k << r$ [14].

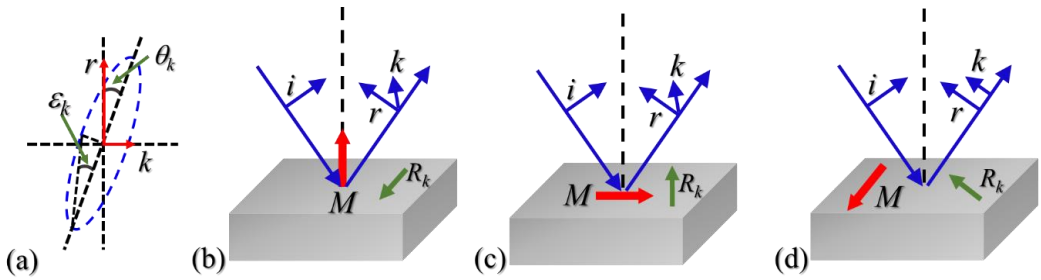

Figure 4.1: (a) The geometry of Kerr rotation (θ_k) and Kerr ellipticity (ε_k) and the schematic diagrams of (b) polar (c) longitudinal and (d) transverse MOKE geometries.

In case of transverse MOKE geometry *M* lies in the plane of the sample, but perpendicular to the plane of the incidence (Figure. 4.1 (d)). Only *p*-polarized light shows transverse Kerr effect. Here the reflected beam remains linearly polarized

without any Ker rotation, but the amplitude is changed as magnetization vector changes sign from + ***M*** to –***M***.

4.3 Static Magneto-Optical Kerr Effect (Static MOKE) Microscope:

The static magneto-optical Kerr effect (Static MOKE) microscope was used to measure the magnetic hysteresis loops from some arrays of magnetic nanostructures. The schematic diagram of the setup is shown in Figure. 4.2. A continuous wave He-Ne laser of wavelength (λ) = 632 nm was used for this measurement. The laser beam passes through a variable attenuator, which is used to control the intensity of the incident beam on the sample. The intensity of the transmitted beam is controlled by moving attenuator perpendicular to the beam with the help of a moving stage.

The beam is linearly polarized with *S*-polarization by passing through a Glan-Thompson polarizer. The linearly polarized beam is then chopped at 1-2 kHz frequency by a chopper controlled by a controller unit. The chopped beam is incident on an extra-long working distance (25 mm) microscope objective (MO) with N.A. = 0.55 and magnification = × 40. The incident point of the beam on the back aperture of the MO is away from the center as shown in Figure. 4.2. In this situation the beam will be incident on the sample at an oblique angle less than 90° with the sample surface. The reflected beam from the sample surface is collected by the front lens assembly of the MO. The beam comes out of the back aperture of the MO through a point diametrically opposite to the point of incidence. The magnetic field is applied in the plane of the sample. Using this geometry the longitudinal Kerr rotation is measured by sending the back-reflected beam to an optical bridge detector (OBD). In absence of any magnetic field, first the balanced condition of the detector is obtained by rotating the axis of the polarized beam splitter (PBS) slightly away from 45°. Calibration of the OBD will be done by rotating the PBS by 1° on both sides of the balanced condition and the dc output of the detector is recorded.

When the magnetic field is applied the detector will no longer be in the balanced condition (*i.e.*, A≠ B). The difference signal A-B, which is proportional to the magnetization of the sample, is measured as a function of the applied bias

magnetic field to obtain the hysteresis loop and is converted to Kerr rotation by multiplying it with the calibration factor. The output signal is measured in a phase-sensitive manner by using a lock-in-amplifier with a reference signal from the chopper. For the measurement of the hysteresis loops from an array of blanket film the laser spot is carefully placed at a desired position on the array by using scanning *x-y-z* stage.

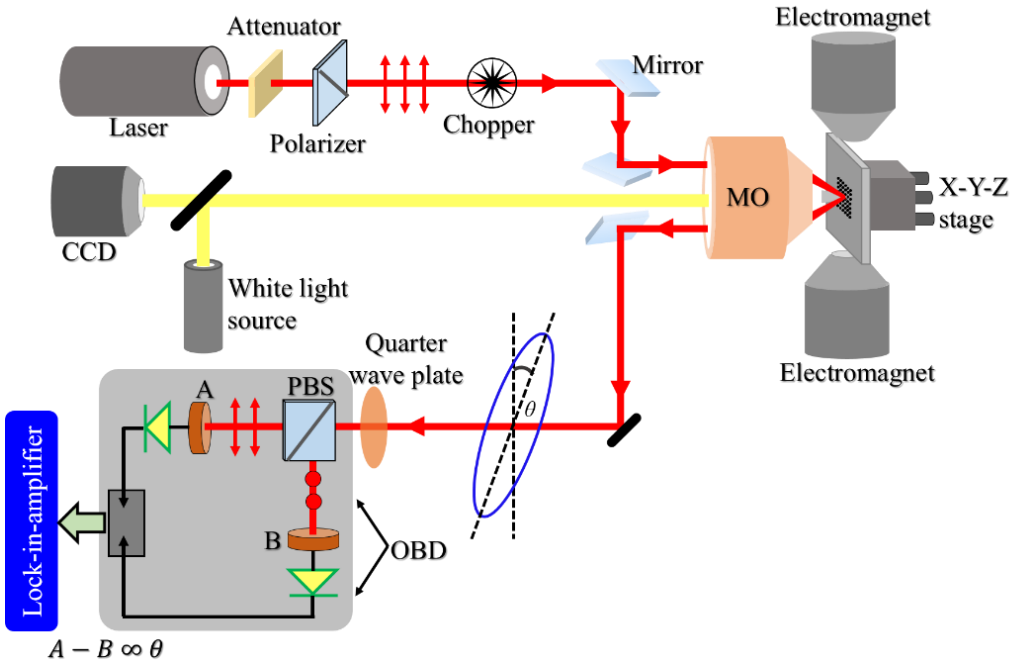

Figure 4.2: The schematic diagram of static magneto-optical Kerr effect (Static MOKE) microscope.

4.4 All-Optical Time-Resolved Magneto-Optical Kerr Effect (TRMOKE) Microscope:

All-optical TRMOKE setup is the most efficient technique for the measurement of time-domain magnetization dynamics of magnetic nanostructures. The results on time-domain magnetization dynamics presented in this thesis are all measured by the TRMOKE setup in our laboratory. The photograph of this setup is shown in Figure 4.3. In the photograph some important components are labeled. Here we given the complete list of components required for the development of this set-up.

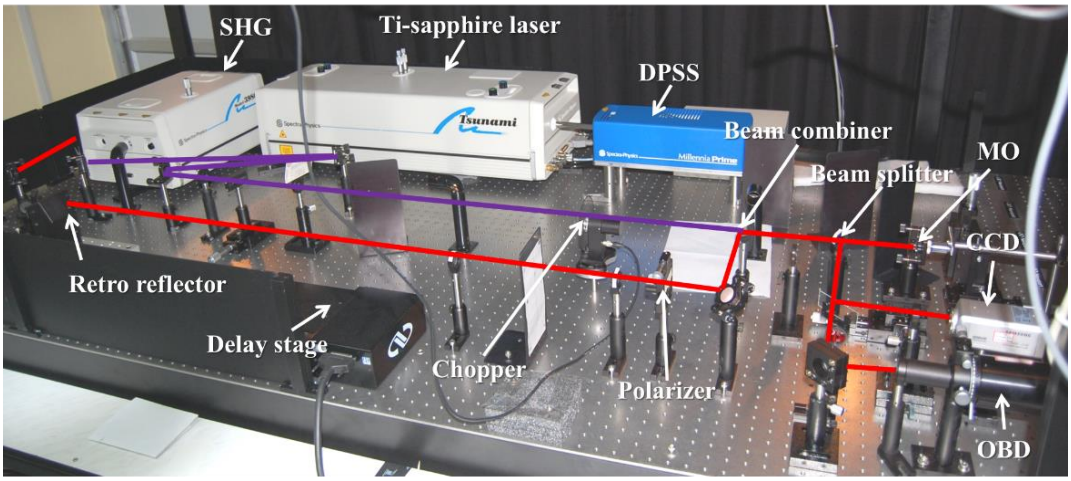

Figure 4.3: The photograph of the all-optical time-resolved magneto-optical Kerr effect (TRMOKE) microscope in our laboratory at the S. N. Bose National Centre for Basic Sciences. The important components of the set-up are marked by arrows.

4.4.1 Components

Table 2: List of components of all-optical time-resolved magneto-optical Kerr microscope (TRMOKE).

Sl. Number	Name	Company	Model
1	Optical Table	Newport	RS 4000^{TM}
2	Optical Table Enclosure	Custom Mode	-
3	Diode Pumped Solid State (DPSS) Laser	Spectra Physics	Millennia Pro 10s (with diode laser: model J80)
4	Ti-sapphire Laser	Spectra Physics	Tsunami
5	Second Harmonic Generator	Spectra Physics	3980
6	Retro-reflector	Newport	UBBR1-2S
7	Delay Stage	Newport	(M-)IMS series
8	Delay Stage Motion controller	Newport	EPS301
9	Optical chopper and it's controller	Thorlabs	MC2000

10	Polarizer	Thorlabs	GTH5M
11	Microscope Objective (MO)	Newport	M-40X
12	Piezo Electric x-y-z stage and it's controller	Thorlabs	MC2000
13	CCD Camera and Monitor	Samsung	SDC-313B
14	Optical Bridge Detector (OBD)	Neoark Corporation	NDT-40110GTP
15	Dielectric Mirrors	Thorlabs	BB1-E02 BB1-E03
16	Dielectric Filters	Thorlabs	FGB37 FGL610
17	Attenuators, Neutral density filters	Thorlabs	NE40B NDL-10C-4
18	Beam Splitters (Non-polarized)	Thorlabs	EBS1 (50:50) EBP1 (70:30)
19	Lenses	Thorlabs	LA1608 LA1708
20	Lock-in Amplifiers	Stanford Research Laboratory	SR830
21	Mirror Mounts	Thorlabs	KS1, KM100
22	Lens Mounts	Thorlabs	LMR1/M
23	Polarizer Mounts	Holmarc	PMC-25
24	Linear Stage	Holmarc	TS-90-Mu10-01
25	Manual X-Y Stages	Holmarc	TS-90-Mu10-02
26	Oscilloscope	Agilent	DS05032A
27	Digital Multimeter	Rishabh	RISH Multi 15S
28	Spectrometer	Ocean Optics	USB4000
29	IR Viewer	Newport	IRV2-1700
30	Beam Height	Home Made	-
31	Beam Block	Home Made	-

32	Power Meter	Newport, Coherent	407A, FieldMate

4.4.2 Description of Lasers

Three lasers and a second harmonic generator (SHG) are used to build our TRMOKE setup. The diode pumped solid state lasers (DPSS) is used to pump the Ti-saphire oscillator (Tsunami) for the production of mode locked laser pulse. This DPSS is pumped by an array of solid state lasers. In the following we will discuss about the working principles of these lasers[15-19].

❖ **Diode Lasers**

The diode laser used here is specially designed for generating high power with a smaller mode volume. It produces a continuous wave (CW) output with a power of upto 10 W (adjustable). It consists of twenty diode laser bars, each of which is made of single monolithic piece of semiconductor. These twenty laser bars are collimated with a cylindrical microlens of high numerical aperture and which produce a highly asymmetric output beam coupled into a fiber bundle by the well-known *FCbar* technology. This technology is very efficient for coupling of the output of diode laser in fiber. This fiber bundle is made from several multimode fibers. Typically 85-90% light of diode laser is coupled into the fiber bundle. The fiber bundle is directly connected to the DPSS (Millennia)[17].

❖ **Diode Pumped Solid State Lasers or MILLENNIA**

1. *Working Principle:*

Yttrium Vanadate crystalline matrix (Nd:YVO_4) doped with Nd^{3+} ions is the gain medium of Millennia. The Nd^{3+} doped ion is a four level system having a principle absorption band in red and near infrared regime. The excited electrons move from the lower energy levels to upper energy level and suddenly fall down to the $^4F_{3/2}$ level. This is a metastable state and the upper level of lasing transition (Figure.4.4 (a)). As a result for the transition of $^4F_{3/2}$ level to $^4I_{1/2}$ level a 1064 nm laser beam is emitted. Electrons are quickly relaxed to their ground state from $^4I_{1/2}$ state. A population inversion is built up in between the energy levels $^4F_{3/2}$ level to $^4I_{1/2}$. Though there are

also transitions at 1319, 1338 and 946 nm, but at room temperature we have the lower gain along with a higher threshold value than the 1064 nm transition. Those factors and the wavelength selection optics limit the oscillation to 1064 nm. The monochromatic output of the diode laser is shown in Figure 4.4 (b) which is overlapping with the absorption spectra of the Nd^{3+} ion. So the Millennia is pumped by the diode laser. The efficiency of Millennia can be improved by focusing the diode laser output on a volume in the active medium of the Millennia in such a way that it matches with the radius of TEM_{00} mode of Millennia (mode matching) (Figure. 4.5 (a)). An arrangement of a beam splitter and a photodiode and a feedback from the photodiode to the pump laser provides a constant output in power mode operation. The shutter is placed outside the cavity (Figure. 4.5 (b)) which will act as a beam blocker. This shutter is opened by a controller. The 90° polarization rotation aligns the polarization axis of the output beam vertically.

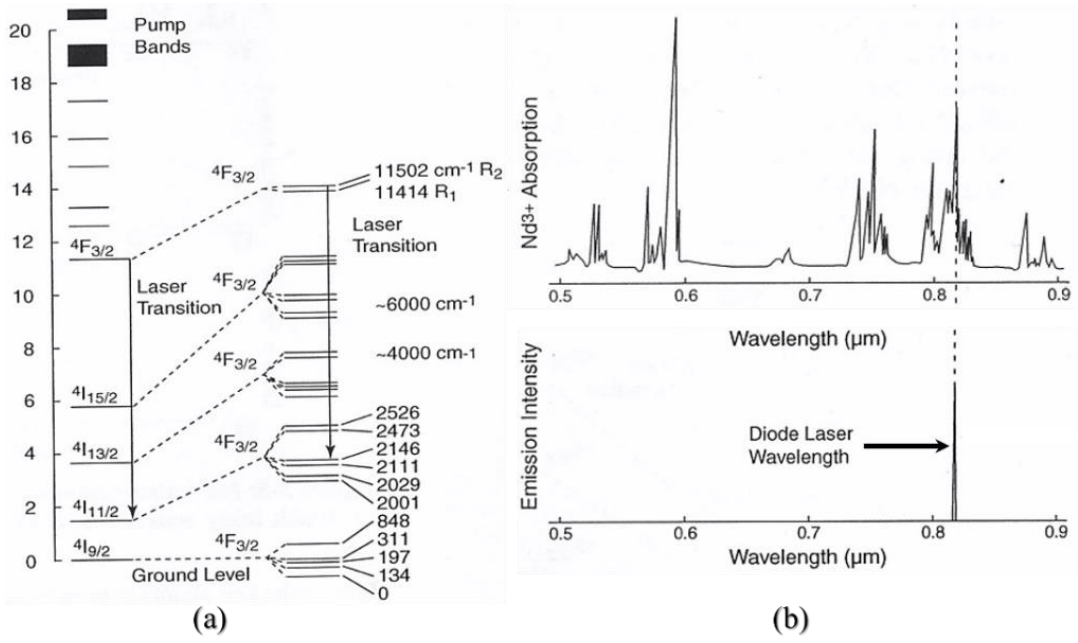

Figure 4.4: (a) Energy bands and various emission spectra for Nd^{3+} ion. (b) The absorption spectrum of Nd^{3+} ion is compared with the emission spectrum of the diode laser.

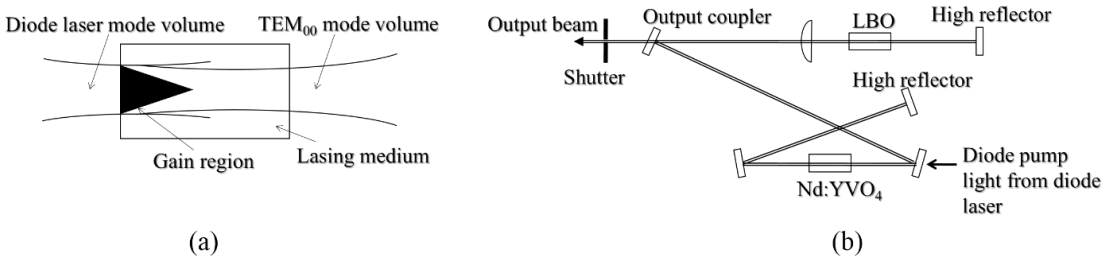

Figure 4.5: (a) The schematic diagram of mode matching between diode laser mode volume and TEM_{00} mode volume of Millennia. (b) Schematic diagram of Millennia laser head.

2. Frequency Doubling:

The output of Millennia is converted from infrared (λ = 1064 nm) to visible light (λ = 532 nm) with the help of a lithium triborate (LBO) nonlinear crystal. The efficiency of this crystal is temperature sensitive, so a temperature regulating oven is used to maintain the crystal at the appropriate phase-matching temperature to keep the output wavelength fixed to 532 nm. This crystal itself keeps the fundamental and the second harmonic beam collinear (non-critically phase-matched), so the alignment of the laser cavity is not required. Again a large acceptance angle makes it insensitive to any slight misalignment within the Millennia. So, in spite of having lower coefficient than other materials, LBO crystal is used for frequency doubling in Millennia.

The expression of the second harmonic power is as follows[17]:

$$P_{2\omega} \infty \frac{d_{eff}^2 P_\omega^2 l^2 [\varphi]}{A} \tag{4.1}$$

Where $d_{eff}$is the effective nonlinear coefficient, P_ω is the fundamental input power, l is the effective crystal length, $[\Phi]$ is the phase matching factor and A is the cross sectional area of the beam in the crystal.

❖ **<u>Mode-Locked Ti-Sapphire Laser or Tsunami:</u>**

3. Working Principle:

Ti-sapphire is a crystalline material which is obtained by doping the sapphire crystal (Al_2O_3) with titanium ions (Ti^{3+}). From Figure 4.6 we can conclude that the absorption transition for this crystal spreads over a broad range of wavelengths from

400 nm to 600 nm. So, this system can be efficiently pumped by the output of the Millennia. The fluorescence band is extended over a broad range from 600 nm to 1000 nm. As a result the short wavelength end of fluorescence and long wavelength end of the absorption spectrum overlap with each other, so the lasing action is possible only for $\lambda > 670$nm.

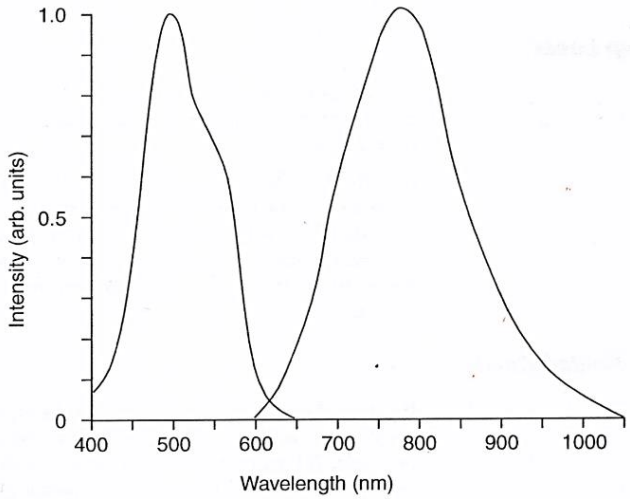

Figure 4.6: Absorption and emission spectra of Ti-sapphire crystal.

4. *Ten-fold Mirror Cavity:*

Tsunami is a mode-locked laser. In this kind of mode-locked laser to get a convenient repetition rate (near 80 MHz) the cavity should be sufficiently longer than that in a CW laser. For this purpose a ten mirror folded cavity is used in Tsunami [Figure. 4.7] to achieve an optimum performance in minimal space. This optimization in space makes the pumping more complex which may cause astigmatism in the beam if the focusing mirror is used at an angle other than the normal incidence. This kind of astigmatism can be virtually eliminated by a proper selection of angles of the cavity focus mirrors and the rod-length at Brewster's angle.

To keep the cavity stable, clean and dry nitrogen gas (purity = 99.999 %) is constantly purged to the laser head to remove dust and water vapor. A chiller unit keeps the Ti-sapphire rod at constant temperature for long term stable performance.

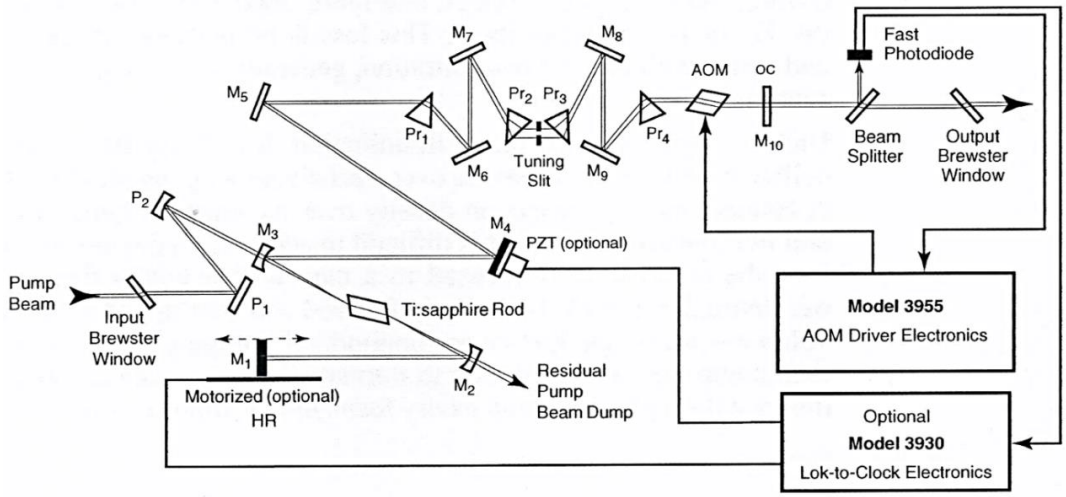

Figure 4.7: A schematic of the beam path inside the folded cavity of Tsunami.

5. *Group Velocity Dispersion and Wavelength Selection*

According to Heisenberg uncertainty principle the product of a pulse of duration Δt_p and bandwidth Δv ($\Delta t_p \times \Delta v$) will always be greater than a constant value. So for shorter pulse, greater difference will be found between lowest to highest frequency within a pulse. Refractive index (n) is a function of frequency, so each frequency in a pulse will experience a slightly different refractive index and hence a slightly different velocity. This causes a time separation between frequencies of a pulse. So the variation of transit time as a function of wavelength will be observed, which is known as the group velocity dispersion (GVD). If the lower frequency branch travels faster than the higher frequency branch then it is known as positive GVD and the corresponding pulse is said to be positively chirped and vice-versa. A non-linear n introduces an intensity dependent index at high intensities.

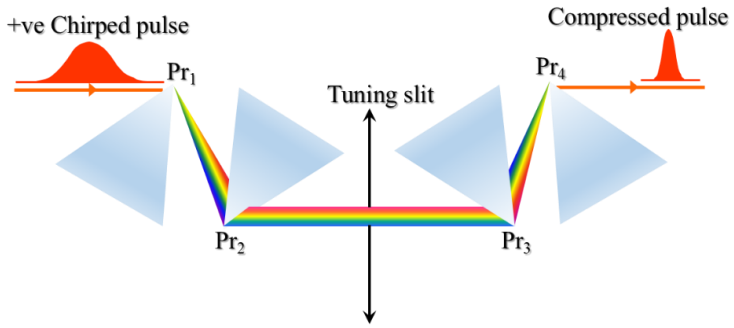

Figure 4.8: The sequence of four prism used for dispersion compensation in Tsunami laser.

Inside the Tsunami laser the arrangement of four prism system is used to compensate positive GVD (Figure. 4.8). The net intercavity GVD is changed by translating prism P_2 and P_3 perpendicular to their bases. This translation can be achieved by using a single micrometer adjustment (not shown in figure). Inside the cavity more optical materials can be added by translating P_2 and P_3 further into the intercavity beam and the net GVD becomes less negative. The different spectral components of the pulse are spatially spread between prism P_2 and P_3. This allows to select the convenient wavelength by moving a slit between these two prisms in the direction of the spectral spread. The output bandwidth and pulsewidth can be controlled by varying the slit width.

❖ Second Harmonic Generator

Second harmonic generator is mainly used to double the frequency of the fundamental beam from the Ti-sapphire laser. A barium beta borate (BBO) crystal is used in SHG for doubling the frequency. This crystal also has a higher conversion efficiency than an LBO crystal. The schematic diagram of SHG[18] and its optical path is shown in Figure. 4.9. From Figure. 4.9 it shows that mirrors M_1 and M_2 direct the output beam while mirror M_3 focuses the beam to a small waist into a critically phase matched (angle used) type I second harmonic crystal. The BBO crystal produces a horizontally polarized second harmonic beam, whereas the residual fundamental beam remains vertically polarized.

The prism P_1 separates out the second harmonic and the residual fundamental beams. The prism P_1 has a high reflective coating at residual fundamental IR wavelength, so the fundamental beam will be reflected but the second harmonic beam will be diffracted to prisms P_2 and P_3. Both P_2 and P_3 have anti-reflection (AR) coating at second harmonic wavelength. Hence, these prism pairs can redirect the second harmonic beam parallel (roughly) to the fundamental beam in addition to compensating for the beam ellipticity.

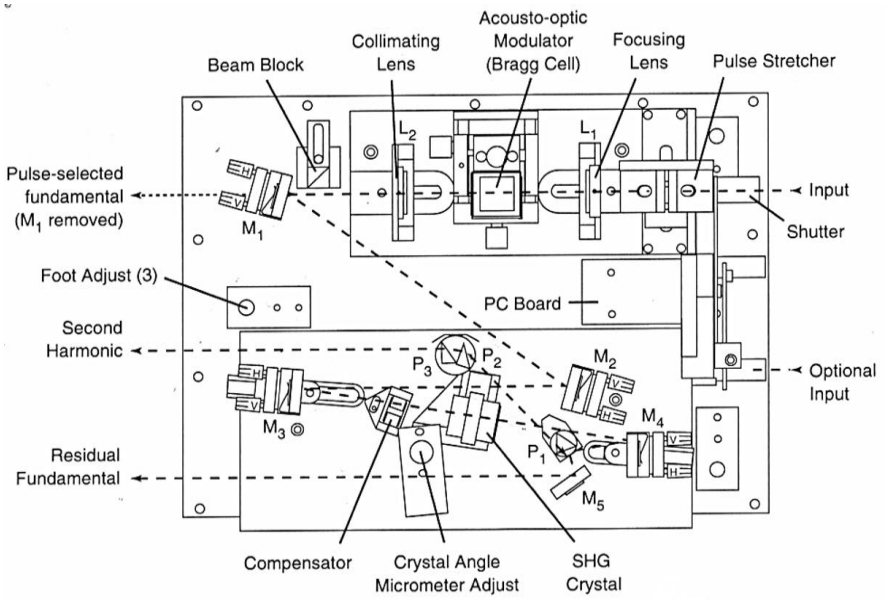

Figure 4.9: The schematic diagram of Second Harmonic Generator (SHG) and its optical path are shown.

The thin BBO crystal is used in the second harmonic generator due to following advantages:

1. Minimizes the pulse broadening problem due to group velocity dispersion (GVD).
2. No compensating crystal is required.
3. Only a single SHG crystal is required to match the phase over the entire tuning range (690 nm to 1090 nm).

From equation 4.4.1 we can observe that the conversion efficiencies of SHG crystal is inversely proportional to the cross sectional area of beam in the crystal. This efficiency can be further increased by reducing the beam waist. The lens pair (L_1 and L_2) helps us to get an optimum beam waist. This combined lens configuration acts as a 1:3:1 beam-expanding telescope. As the BBO crystal is slightly hygroscopic, it is sealed in a small cylinder with AR-coated windows and filled with an index matching fluid.

4.4.3 Description of the set-up

The photograph of the TRMOKE setup in our laboratory is shown in Figure. 4.3. This photograph shows that the entire setup is installed on an L-shaped optical table (two Newport *RS4000 series* tables are joined) with vibration isolation. The optical table is

an essential part of any highly sensitive optical experiment like TRMOKE. In our case the optical table is made of vertically bonded closed cell honeycomb core sandwiched in between two sheets of ferromagnetic material (4.8 mm thick). This allows to increase the stiffness constant of the table and reducing the mass to increase the resonant frequency of the table well above the external mechanical and acoustic vibration frequency. Therefore, any external vibration cannot resonate the table easily. The broadband and tuned hydraulic dampers are used to fill up the cores of the table and also to damp out the vibrations and acoustic modes of the table very quickly. The table is placed on top of vibration isolations in floating condition. So the table is isolated from the mechanical vibrations originates from the ground. The flatness of the table surface is ± 0.1 mm over 600 × 600 mm^2 area. The square array of circular holes with 25 mm grid enables mounting of the laser, optics and detectors.

A schematic diagram of the TR-MOKE microscope is shown in Figure. 4.10. A solid state laser (DPSS) is pumped by an array of diode lasers to produce a maximum output power 10 W (adjustable) and wavelength λ = 532 nm. The output of the DPSS is used to pump the Ti-sapphire laser. Regenerative mode locking mechanism produces a train of laser pulses with ~ 70 fs pulse width and maximum average power of 2 W at a repetition rate of 80 MHz (25 nJ/pulse). Though, the output wavelength can be tuned from 690 nm to 1080 nm, the output is kept fixed at around 800 nm in our experiments for stable operation and better sensitivity of the Si based detectors at that wavelength.The output beam (red beam) from the Ti-sapphire oscillator is vertically polarized and has a spot size of ~ 2 mm. This beam is split into two parts (70:30) by a beam splitter (B_1). The intense part is frequency doubled (λ = 400 nm) by passing through a second harmonic generator (SHG) with pulse width ~ 100 fs which is used to pump the magnetization dynamics of the sample whereas the linearly polarized fundamental beam is used for probing. The pump beam travels through a variable attenuator (A_2) and a mechanical chopper after getting reflected from three highly reflecting mirrors (M_{b1}, M_{b2} and M_{b3}). The attenuator is coated with a reflecting material such as the reflectivity of the material changes gradually from one end to other end. The transmitted pump fluence can be controlled by moving the attenuator horizontally.The chopper is used to modulate the intensity of the pump beam at 1-2 kHz frequency, which is used as the reference signal for lock-in detection. The pump path is kept fixed. The fundamental or probe beam is guided

through a fixed optical path by using a set of highly reflecting mirrors (M_{r1}, M_{r2}, M_{r3} and M_{r4}). A variable attenuator (A_1) is also placed in the probe path to adjust its fluence. The probe beam is then reflected back from a retro reflector placed on a motorized delay line. The retro-reflector reflects the incident beam in such a way that the reflected beam becomes antiparallel to the incident beam. The probe path can be varied by moving the retro-reflector back and forth on the delay stage. This is generally done by a motion controller and a PC interfaced with the delay stage through GPIB connection (Figure. 4.10). The beam is then passed through a pair of lenses L_1 (f_1 = 75 mm) and L_2 (f_2 = 200 mm) arranged in a telescopic arrangement, which collimates the beam and increased the beam diameter to ~ 5 mm so that it fills the back-aperture of the microscope objective. The beam is then passed through a Glan-Thompson polarizer with extinction coefficient of 100,000:1, which refines the polarization state of the probe beam to a very high quality.

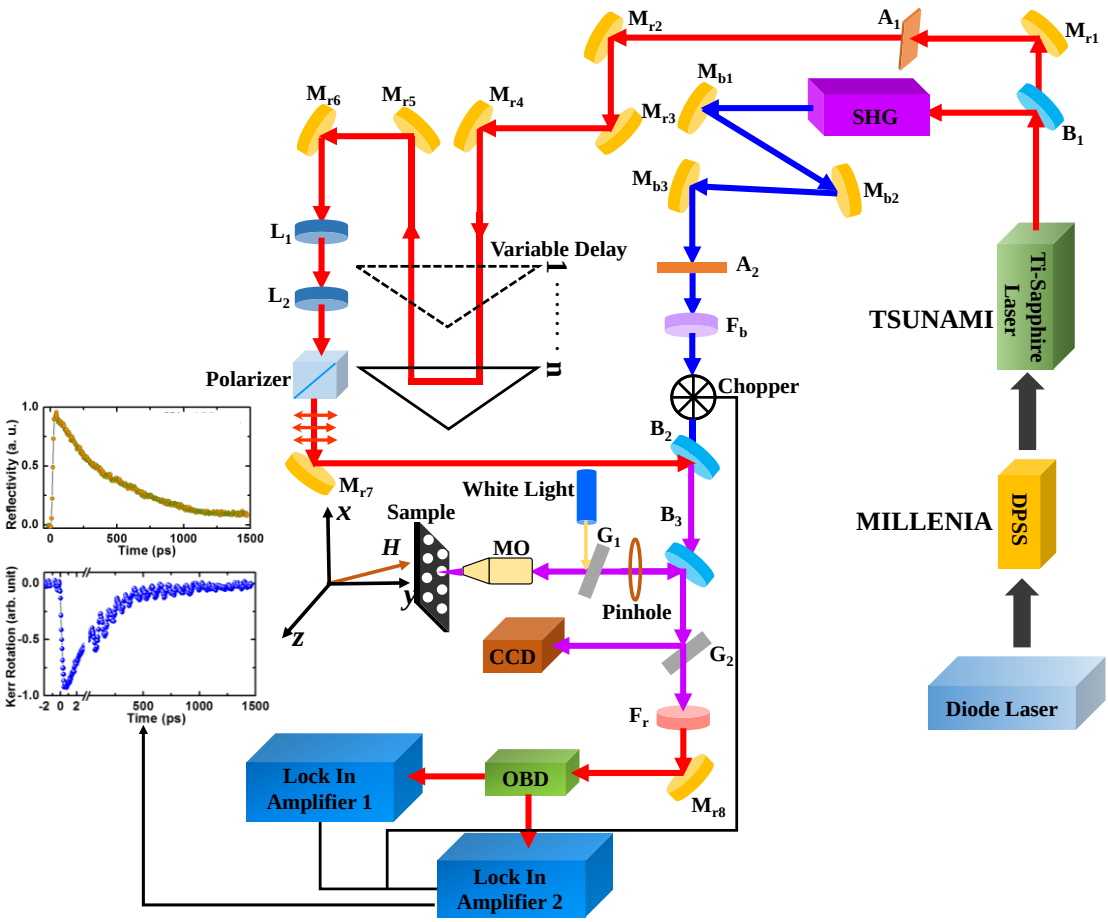

Figure 4.10: A schematic diagram of an all-optical time-resolved magneto-optical Kerr effect (TRMOKE) microscope with a collinear pump-probe geometry.

The modulated pump beam and linearly polarized probe beam are spatially combined with the help of a 50:50 non-polarized beam splitter B_2 set at an angle of 45° to the optical path of the probe beam, which acts as a beam combiner. Both the beams are collinearly focused onto the sample under study using a single microscope objective (MO: M-40X, N.A. = 0.65). This collinearity is optimized with the help of steering mirrors (particularly M_{r6}, M_{r7}, M_{b1}, M_{b2} and M_{b3}). The combined beams pass through a 50:50 non-polarized beam splitter B_3 and a glass slide (G_1) both set at 45° to the optical path before entering into the MO at normal incidence. It is very important to ensure that the sample is precisely placed normal to the axis of the microscope objective and also to the directions of the pump and probe beams. This can be achieved by adjusting the tilt of the MO.

The sample is generally held by using a suitable sample holder, which is mounted on a computer controlled piezo-electric scanning *X-Y-Z* stage. The probe beam is focused to a diffraction limited spot size (~ 800 nm) at the sample surface with the help of the MO and the Z-travel of the piezoelectric stage. The pump beam is spatially overlapped with the probe beam after passing through the same MO and is carefully placed at the center of the pump beam, where the latter is slightly defocused with a spot size of ~ 1 μm due to the chromatic aberration as shown in Figure. 4.11.
The back-reflected beams from the sample are collected and collimated by the same microscope objective (MO) and are reflected by the beam splitter B_3 towards the detector.In this path, small parts of the back-reflected pump and probe beams are sent to a CCD camera (after reflection from a glass slide G_2) for viewing the spatial overlaps of the pump and probe spots onto the sample.The remaining part is sent to an optical bridge detector (OBD) after filtering out the pump beam by a spectral filter (F_r). The optical bridge detector measures the Kerr rotation under a balanced condition and separates it from the total reflectivity signal. Consequently, the spin (Kerr rotation) and the charge and phonon (reflectivity) dynamics are isolated from each other. A white light is reflected by a glass slide (G_1) placed in between B_3 and MO and is focused onto the sample surface through the MO to view the sample structure with sub-μm spatial resolution such that we can locate the exact position where the pump and probe beams are focused onto the sample.

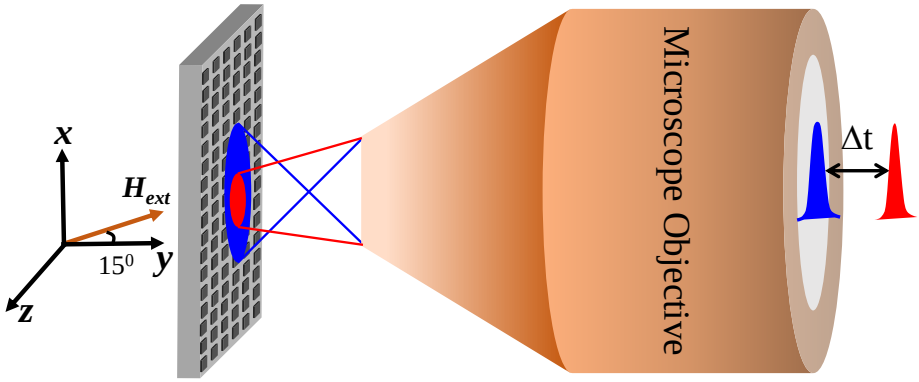

Figure 4.11: Schematic diagram of the collinear geometry of pump and probe beams focused by a microscope objective (MO) on the sample surface with in-plane bias field (H) geometry.

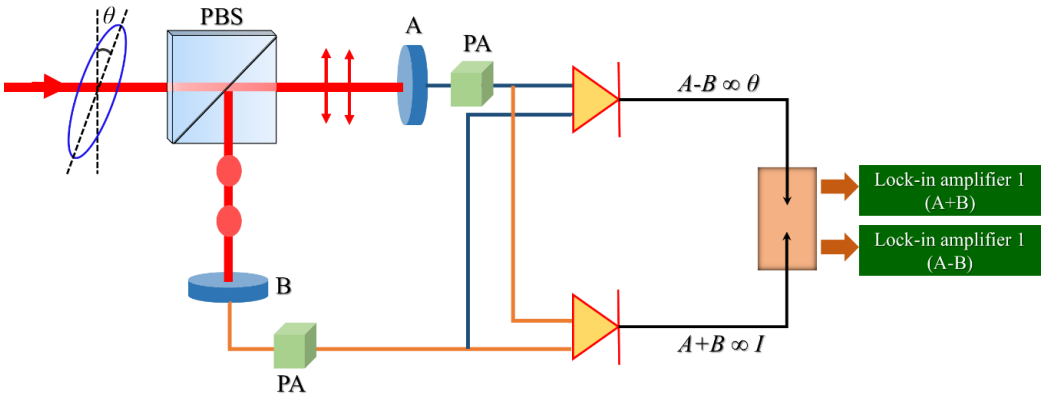

Figure 4.12: Schematic diagram of the optical bridge detector unit is shown.

Any ray with non-zero angles of incidence carries information about the longitudinal Kerr rotations, if any, present in the magnetization dynamics. However, in our measurements we have not used split photodiodes and hence, the longitudinal Kerr effect gets averaged out to negligible net value and we primarily measure the polar Kerr rotation. Still, there can be a finite longitudinal Kerr rotation component mixed with polar Kerr rotation if the incident beam is not perfectly normal to the sample/MO or the beam does not travel along the axis of the MO.

The geometries of dc bias magnetic fields for different samples are shown in figure. 4.11. The bias field is applied at a small angle (~ 15°) to the sample plane. Initially, a high field is applied along sample plane to saturate the magnetization. The magnetic field strength is then reduced to the bias field value to ensure that the magnetization remains saturated along the bias field direction. The bias field is tilted to have a finite

demagnetizing field. This demagnetizing field is eventually modified by the pump pulse to induce the magnetization precession within the sample and we measure the corresponding polar Kerr rotation for the out-of-plane component of the precession orbit of the tip of the magnetization vector.

Figure 4.12 presents the schematic diagram of the OBD used in the TR-MOKE measurements. There is a polarized beam splitter (PBS) at the entrance of the OBD, which splits the beam into two orthogonal polarization componets. These two parts with intensities I_A and I_B are then detected by two photodiodes A and B, respectively. The outputs of these two photodiodes are then preamplified (by pre-amplifiers PAs) and used as inputs for two operational amplifiers (Op-Amps) to measure the total signal A+B (*i.e.*, $I_A + I_B$) and the difference signal A-B (*i.e.*, $I_A - I_B$). The outputs of these two Op-Amps are measured by the lock-in-amplifiers (SR830) in a phase sensitive manner with the chopper frequency as the reference frequency. Initially, in the absence of the pump beam, the optical axis of this PBS is set at 45^0 to the plane of polarization of the probe beam. Under this condition $I_A = I_B$, *i.e.*, A-B = 0 and the detector is said to be in a "balanced" condition. In the next step, when the pump beam excites the sample, the plane of polarization of the probe beam is rotated due to the magneto-optical Kerr effect. Consequently, the optical axis of the PBS is no longer at 45^0 to the plane of polarization of the probe beam. As a result $I_A \neq I_B$ and A-B $\neq 0$. The linear magneto-optical Kerr rotation is proportional to the sample magnetization and hence the signal A-B gives a non-invasive way of measuring the magnetization of the sample. Thus, by measuring A-B as a function of time, magnetization dynamics over different timescales are observed. This magnetization dynamics can be used to extract various material parameters including Gilbert damping, magnetic anisotropy, saturation magnetization, gyromagnetic ratio of ferromagnetic thin films and confined nanostructures. On the other hand, the time-resolved reflectivity of the sample gives us the charge and phonon dynamics. The schematic diagram is shown in Figure. 4.10. The outputs (A-B and A+B) are regularly checked while aligning and optimizing the function of the OBD. In our set up the PBS and the two photodiodes A and B are mounted on a stage attached with a precision rotation mount, while the electronic signal processing is done in the circuit placed in a separate box using low noise amplifiers and connected by low noise cables and connectors. This improves the stability of the signal and the ease of optical alignment.

The collinear pump-probe geometry enables us to achieve a diffraction limited spatial resolution of about 1 μm along with a temporal resolution of about 100 fs limited by the cross-correlation between the pump and probe pulses. The balanced photodetector or OBD helps to achieve a very high measurement sensitivity of Kerr signal (~ μdeg) because a small variation of the Kerr rotation or ellipticity can be measured on top of a zero or negligible background.

4.4.4 Daily Alignment Procedure:

The construction procedure of this TRMOKE microscope is very involved and it requires very high precession optical alignment of the whole setup starting from the alignment of the optical table. In general before starting everyday's experiment we need some routine alignment that we will discuss here. But if there is a significant walking of the output beam from Tsunami due to the fluctuation in the environment temperature and humidity then we need to re-align the laser cavity to optimize the laser performance and also the alignment of the laser beam outside the cavity.
Normally the following steps are performed before starting the daily experiment.

- At first the output power and spectra of Tsunami is checked. The output power is maximized after adjusting the central wavelength (λ_0 = 800 nm) and FWHM (~ 10 nm or more) with the help of external micrometer controllers of Tsunami.
- The alignment of the retro-reflector is checked by placing the 'beam height' in the path of probe beam after the retro-reflector and by moving the retro-reflector from the left end to the right end of the delay stage. If there is a movement of the probe beam while moving the retro-reflector then the probe beam should be aligned.
- The collinearity of the pump and probe beams is checked by placing the 'beam height' after the beam combiner (B_2). Both beams should go through the hole on the beam height. Then the overlap between the pump and the probe is checked by observing their images in CCD camera. If they are not spatially overlapped on the sample then the overlapping is adjusted with the help of mirrors M_{b1}, M_{b3} and M_{r6}, M_{r7}.

- Now we check whether or not the pump-probe is co-axial with the MO. For that the MO is moved back and forth with the help of micrometer screw attached to it. The probe and pump beam is focused and defocused, which can be seen in the monitor attached to the CCD camera. If the pump and the probe beams are exactly co-axial with MO, then they will be focused-defocused keeping their centers fixed at a particular position. If there is a movement of the centre either along the horizontal direction or the vertical direction, then the pump and probe are not collinear with the MO. The pump and probe are made collinear with the help of the mirrors M_{b1}, M_{b3} and M_{r6}, M_{r7}.
- At last the alignment of the OBD is checked.

The routine alignment helps to get a basic alignment of the set up. A fine tuning is required before starting the measurement. This is usually done with a standard sample (a small piece of Si [100] wafer). The Si wafer is mounted on the sample holder with its polished surface facing the pump and probe beams. The pump and probe fluences are chosen to be about 10 mJ/cm^2 and 2 mJ/cm^2 (with the help of attenuators A_1 and A_2). The dc value of the total reflectivity (A + B) signal in the OBD is checked by a multimeter. For a reasonably good alignment of the setup, the dc reflectivity signal is more than 500 mV. If the measured voltage is lower than that, then the alignments of the MO and the OBD are improved. After that the total reflectivity just after the zero delay (by moving the stage to the position just after the zero delay) is checked by a lock-in amplifier. For a reasonably good alignment this value should be between 500 μV or more in the lock-in amplifier. If the A + B signal in the lock-in amplifier is found to be lower than the above value, the overlapping of pump-probe on the sample surface is improved by adjusting the mirrors M_{b1}, M_{b3} and M_{r6}, M_{r7}. After that the time-resolved reflectivity data from the Si wafer is measured over about ~ 2000 ps. The cross-correlation of pump and probe can be obtained by fitting a Gaussian function to the reflectivity signal at the zero delay, which is usually ~ 100 fs. A typical reflectivity signal is shown as a function of the time delay between the pump and the probe in Figure. 4.13. This shows that the reflectivity sharply goes up to a maximum value right after the zero delay position and then decays exponentially as the time delay increases. For a good alignment of the retro-reflector and the pump and

probe beams the reflectivity for the standard Si sample should decay with a time constant of ~ 210 ps. We take this as the standard data for a good alignment of our set up. A faster decay of the reflectivity often indicates that the spatial overlap between the pump and probe beams is lost with the movement of the delay stage. In this case the delay stage is aligned by optimizing the total reflectivity signal at later time delays instead of optimizing it right after the zero delay. Let us say the retro-reflector is placed at the position of 25 ps in time delay. The reflectivity signal is then improved by re-aligning the pump and the probe beams. The delay stage is then placed say, at 40 ps in time delay. The reflectivity signal is again improved by re-aligning pump and probe. After optimizing the reflectivity signal at 3 - 4 different time delays the full time-resolved reflectivity signal is measured again. If now the decay time is found to be close to or same as the standard value (210 ps), then the alignment is complete, else the above procedure is repeated until the desired decay time is obtained.

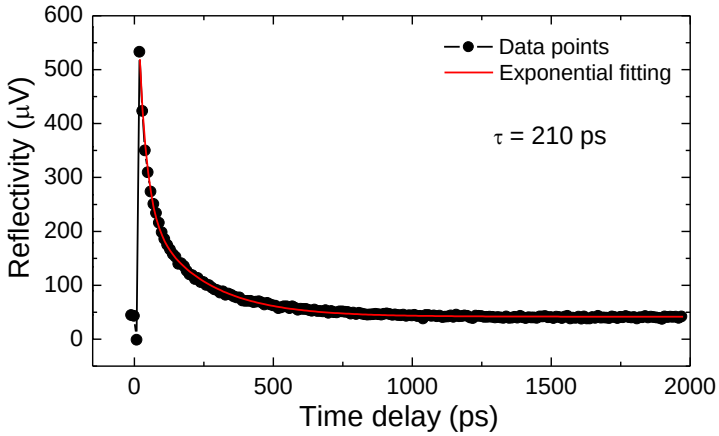

Figure 4.13: The reflectivity signal (A + B) from a Si [100] wafer as a function of the time delay between the pump and probe beams. The decay of the reflectivity signal after the zero delay has been fitted with a double exponential decay function. The time constant of the longer decay is 210 ps.

Once the whole alignment is finished, the set up is said to be ready for measurement.

4.5 Ferromagnetic Resonance Spectroscopy

Ferromagnetic resonance (FMR) spectroscopy is an efficient technique to detect the dynamic magnetic properties of magnetic nanostructures[20]. In this thesis the FMR results are detected using our homemade broadband FMR spectrometer (Figure. 4.14). The photograph of this set-up in our laboratory is shown in Figure 4.14. In this

system, a vector network analyser (VNA) (Agilent PNA-L N5230C) is used to detect the microwave absorption caused by the ferromagnetic resonance. As opposed to the classical FMR, here both frequency and magnetic field can be varied here continuously within a specific range of values.

The basic theory of FMR phenomenon has been explained in Section 2.5. Here we will discuss about the details of the VNA-FMR setup. A high frequency AC magnetic field H_{rf} and a static applied field H_{ext} are the two important factors in the system.

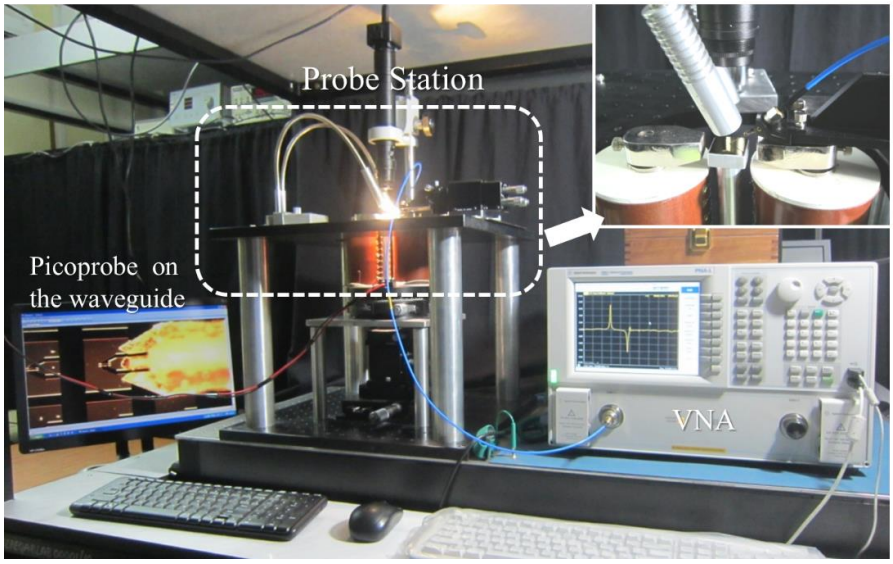

Figure 4.14: Photograph of the home-made broadband ferromagnetic resonance spectrometer.

In our setup the frequency range of the VNA is from 10 MHz to 50 GHz. We have also used a home-made high frequency probe station for broadband ferromagnetic resonance spectroscopy of our samples. The NPS micro-positioner (800 MRF) is connected with a ground-signal-ground type (G-S-G) probe tip (GGB Industries 40A-GSG-150 picoprobe) which has 125 µm pitch and matched 50 Ω impedance, made of a nonmagnetic material. The homemade high frequency probe station (Figure. 4.14) has an inbuilt electromagnet with maximum field of 2 kOe and the magnet system can be rotated through 360°. It is useful to derive the reference signal by applying a dc magnetic field, called external magnetic field (H_{ext}), parallel to the direction of the rf magnetic field (H_{rf}). To remove and compensate the noise from the cable contact, we calibrate the picoprobe using a calibration kit (GGB CS-5) composed of an ‘Open’, ‘Short’ and ‘Load’ before the experimental process (Figure. 4.15). The schematic of the

calibration procedure and the setup is shown in Figure. 4.16. In Figure. 4.16 'Short' means the signal line is connected with Ground, 'Open' is the signal line is disconnected from Ground, and 'Load' consists of a resistive material (matching 50 Ω) between the signal line and Ground. The unwanted outside effect are eliminated at the time of measurement by this calibration step.

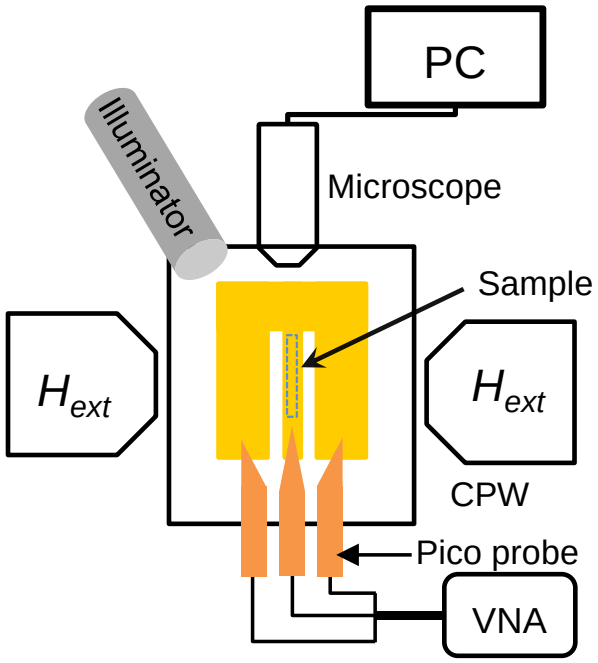

Figure 4.15: Schematic diagram of Broadband Ferromagnetic Resonance Spectrometer.

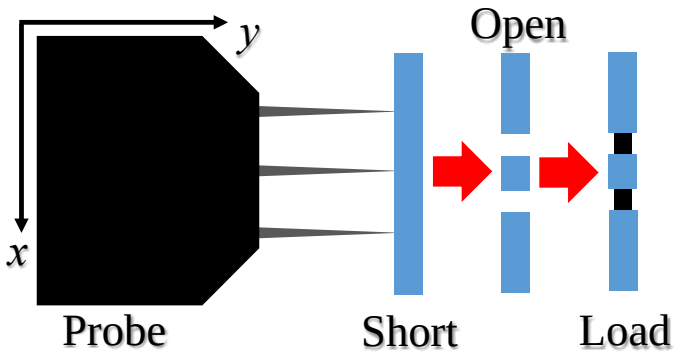

Figure 4.16: Calibration procedure of the high frequency probe.

A co-planar waveguide (CPW) with a characteristic impedance of about 50 Ω is used as a media for excitation of spin waves in the samples, which are placed beneath the CPW. We apply a dc magnetic field parallel to the CPW. The RF signal is applied through the G-S-G line (Figure 4.15) which will produce an rf field perpendicular to the dc magnetic field direction. Resonance phenomena appear when the H_{rf} makes an

angle to H_{ext}. When H_{ext} is applied along x-direction the magnetic moment precesses around the direction of H_{ext} at the resonant frequency. If the rf frequency produced by rf current matches with this frequency then the resonance phenomena including energy absorption occurs. This is the concept of FMR mechanism. After exciting the sample, we obtained scattering parameter (S-parameter) correlations between the incident and reflected electromagnetic waves. Here we used a closed CPW to measure reflection S parameter (S_{11}) *i.e.*, the absorbed signal in reflection geometry. Both real and imaginary parts of S_{11} are plotted against the rf sweep frequency to obtain the FMR spectrum.

Bibliography

[1] J. Kerr, *Philos. Mag. Series 5* **3**, 321 (1877).

[2] A. Hubert and R. Schafer, "Magnetic Domains: The Analysis of Magnetic Microstructure," *Springer*, (1998).

[3] M. R. Freeman and W. K. Hiebert, "Spin Dynamics in Confined Magnetic Structures I," *Springer*, (2002).

[4] M. R. Freeman, R. R. Ruf and R. J. Gambino, *IEEE Trans. Magn.* **27**, 4840 (1991).

[5] W. K. Hiebert, A. Stankiewicz and M. R. Freeman, *Phys. Rev. Lett.* **79**, 1134 (1997).

[6] E. Beaurepaire, J. C. Merle, A. Daunois and J.-Y. Bigot, *Phys. Rev. Lett.* **76**, 4250 (1996).

[7] M. van Kampen, C. Jozsa, J. T. Kohlhepp, P. LeClair, L. Lagae, W. J. M. de Jonge and B. Koopmans, *Phys. Rev. Lett.* **88**, 227201 (2002).

[8] A. Barman, V. V. Kruglyak, R. J. Hicken, C. H. Marrows, M. Ali, A. T. Hindmarch and B. J. Hickey, *Appl. Phys. Lett.* **81**, 1468 (2002).

[9] P. S. Keatley, V. V. Kruglyak, A. Barman, S. Ladak, R. J. Hicken, J. Scott and M. Rahman, *J. Appl. Phys.* **97**, 10R304 (2005).

[10] A. Barman, S. Wang, J. D. Maas, A. R. Hawkins, S. Kwon, A. Liddle, J. Bokor and H. Schmidt, *Nano Lett.* **6**, 2939 (2006).

[11] M. Bauer, R. Lopusnik, J. Fassbender and B. Hillebrands, *Appl. Phys. Lett.* **76**, 2758 (2000).

[12] A. Barman, T. Kimura, Y. Otani, Y. Fukuma, K. Akahane and S. Meguro, *Rev. Sci. Instrum.* **79**, 123905 (2008).

[13] W. K. Hiebert, "Experimental Micromagnetic Dynamics: Ultrafast Magnetization Reversal Using Time Resolved Scanning Kerr Effect Microscopy," Ph.D Thesis, Department of Physics, University of Alberta, (2001).

[14] Z. Q. Qiu and S. D. Bader, *Rev. Sci. Instrum.* **71**, 1243 (2000).

[15] O. Svelto, "Principles of Lasers," 5th Edition, *Springer*, (2009).

[16] W. T. Silfvast, "Laser Fundamentals," 2nd edition, *Cambridge University Press*, (1996).

[17] User's Manual, "Millenia Pro s-Series: Diode-Pumped, CW Visible Laser System," *Spectra-Physics*, (2007).

[18] User's Manual, "Model 3980: Frequency Doubler and Pulse Selector," *Spectra-Physics*, (2002).

[19] User's Manual, "Tsunami: Mode-locked Ti:sapphire Laser," *Spectra-Physics*, (2002).

[20] S. S. Kalarickal, P. Krivosik, M. Wu, C. E. Patton, M. L. Schneider, P. Kabos, T. J. Silva and J. P. Nibarger, *J. Appl. Phys.* **99**, 9 (2006).

Chapter 5

Micromagnetic Simulations

5.1 Introduction

Micromagnetism is an efficient tool for studying a wide range of phenomena including magnetization reversal and dynamics. In previous sections (2.5.1) we have already discussed about the Kittel formula and magnetostatic spin waves in magnetic media. In these cases the magnetization was considered to be uniform throughout the sample. We can calculate magnetization dynamics of the sample by solving the non-linear ordinary differential equation *i.e.*, the Landau- Lifshitz-Gilbert (LLG) equation (equation 2.42) by small angle approximation. In case of infinitely extended bulk magnetic material or two-dimensional magnetic thin films this assumption of uniform magnetization is valid only under certain conditions of the material (such as the sample should be above saturation).

However, for confined magnetic structures such as nanostripes, nanodots, nanoparticles, nanowires, antidots the magnetization inside them become non-uniform even above the saturation field due to the non-uniform nature of the demagnetizing field and so in those cases the above assumption will not valid. For these kinds of nanostructures discrete spin models (where the energy is described by either Ising or Hisenberg Hamiltonian) can be considered but it is hard to calculate the internal spin configuration of micron or sub-micron size magnetic structures and arrays, as the computational memory is limited.

Micromagnetism is a continuum theory, which is mainly developed by the scientists to overcome the gap between macrospin formalism and discrete spin model. In micromagnetic simulations the samples are divided or discretized into a large number of cells and each cells is supposed to be a single spin, which is equivalent to the average magnetization of the cell. The magnetization dynamics of these spins of the cells are numerically calculated by solving the LLG equation.

5.2 Free Energies Calculation of a Ferromagnetic Element in Micromagnetics

The total free energy of a ferromagnetic material in presence of an external magnetic field is expressed as (Ref. section 2.2)

$$E_{total} = E_z + E_d + E_e + E_k \tag{5.1}$$

where E_z is Zeeman energy, E_d is self-magnetostatic energy, E_e is the exchange energy and E_k is magnetocrystalline anisotropy energy. In micromagnetism the total free energy can be written as

$$E_{total} = \int_v \Big[-\boldsymbol{M}.\boldsymbol{H}_z - \frac{1}{2}\boldsymbol{M}.\boldsymbol{H}_d + \mathrm{A}\left((\nabla \boldsymbol{u}_x)^2 + \left(\nabla \boldsymbol{u}_y\right)^2 (\nabla \boldsymbol{u}_z)^2\right) + K_1(1 - (\boldsymbol{a}.\boldsymbol{u})) \Big] dv \tag{5.2}$$

where H_z is the Zeeman field, H_d is demagnetizing field, A is exchange stiffness constant, K_1 is the first order magnetocrystalline anisotropy constant, a is the unit vector parallel to the easy axis and u is the space and time dependent unit vector of magnetization. The space and time dependent magnetization can be written as

$$\boldsymbol{M}(x,t) = M_S(x).\boldsymbol{u}(x,t), \quad |\boldsymbol{u}| = 1 \tag{5.3}$$

In equilibrium, total energy (E_{total}) will be minimum and variation of E_{total} with $\boldsymbol{u}$ vanishes.

Therefore,

$$\frac{\delta E_{total}}{\delta \boldsymbol{u}} = 0 \tag{5.4}$$

This gives Brown's equation

$$\boldsymbol{u} \times \left(M_s \boldsymbol{H}_z + M_s \boldsymbol{H}_d + 2A\Delta \boldsymbol{u} + 2K_1 \boldsymbol{a}(\boldsymbol{u}.\boldsymbol{a})\right) = 0 \tag{5.5}$$

So, in equilibrium $\boldsymbol{M}$ is parallel to an effective field ($\boldsymbol{H}_{eff}$), which is given by

$$\boldsymbol{H}_{eff} = \frac{2A}{M_s}\Delta \boldsymbol{u} + \frac{2K_1}{M_s}\boldsymbol{a}(\boldsymbol{u}.\boldsymbol{a}) + \boldsymbol{H}_z + \boldsymbol{H}_d \tag{5.6}$$

In equilibrium, the torque produced by $\boldsymbol{H}_{eff}$ on $\boldsymbol{M}$ also vanishes *i.e.*,

$$\boldsymbol{M} \times \boldsymbol{H}_{eff} = 0 \tag{5.7}$$

The equilibrium distribution of magnetization in an array of nanomagnets can be obtained from the minimization of equation 5.2. But, in a micromagnetic system, the energy landscape is usually very complicated and contains many local maxima, minima, and saddle points. Therefore, a more appropriate approach to reach an equilibrium condition of a system in a local minimum could be provided by a dynamic description of magnetization through an energy landscape. The motion of a magnetic moment is governed by the LLG equation of motion where time rate of change in magnetization ($\boldsymbol{M}$) is described as a combination of torque produced by effective magnetic field ($\boldsymbol{H}_{eff}$) and a phenomenological damping term.

$$\frac{d\boldsymbol{M}}{dt} = -\gamma\left(\boldsymbol{M} \times \boldsymbol{H}_{eff}\right) + \frac{\alpha}{M_s}\left(\boldsymbol{M} \times \frac{d\boldsymbol{M}}{dt}\right) \tag{5.8}$$

In micromagnetics, the total system is divided or discretized into a number of cells. Therefore, the contributions to the total energy should also be discretized. The discrete approximation of spatially varying magnetization can be written as

$$\boldsymbol{M}(x) \approx \boldsymbol{M}_s(x) \sum_i \boldsymbol{u}_i \eta_i \approx \sum_i M_{s,i} \boldsymbol{u}_i \eta_i = \sum_i \boldsymbol{M}_i \tag{5.9}$$

where η_i is the basis function of the i^{th} cell. In the i^{th} cell the effective magnetic field can be expressed as

$$H_{i,eff} = -\left(\frac{\delta E_{tot}}{\delta \boldsymbol{M}}\right)_i \approx -\frac{1}{V_i}\frac{\delta E_{tot}}{\delta \boldsymbol{M}_i} = -\frac{1}{V_i M_{S,i}}\frac{\delta E_{tot}}{\delta \boldsymbol{u}_i} \tag{5.10}$$

The Zeeman energy can be expressed as

$$E_z = \int_V (-\boldsymbol{M}.\boldsymbol{H}_z) dv = \int_V \sum_J M_{S,j} \sum_k^{x,y,z} u_{j,k} \eta_j H_{Z,k} dv \tag{5.11}$$

Uniaxial magnetocrystalline anisotropy can be written as

$$E_K = \int_V \sum_j K_1 \left(1 - \left(\boldsymbol{a}.\boldsymbol{u}_j \eta_j\right)^2\right) dv \tag{5.12}$$

The exchange energy is expressed as

$$E_e = \int_V \sum_j A \left(\nabla u_j \eta_j\right)^2 dv \tag{5.13}$$

The magnetostatic self-energy can be expressed as

$$E_d = \int_V \nabla . \boldsymbol{M} dv = \int_V \sum_j \sum_V^{\{x,y,z\}} \nabla_k u_{j,k} \eta_j = \int_V \sum_j \sum_k^{\{x,y,z\}} u_{j,k} \nabla_k \eta_j \qquad (5.14)$$

5.3 Simulation Methods and Solvers

5.3.1 Introduction

The non-linear Landau-Lifshitz-Gilbert (LLG) equation is solved to calculate the magnetization dynamics of nanostructures. There are many technical difficulties to obtain the exact solution of LLG equation so numerical calculation becomes an alternative route of this solution. There are two very common approaches for solving LLG equation numerically: (i) Finite Difference Method (FDM) and (ii) Finite Element Method (FEM). In both FDM and FEM methods the samples are divided into large number of cells and each cell is assigned with a single spin (equivalent to the average magnetization of the cell). The size of each cell is kept smaller than the exchange length (l_{ex}) of the material so that the exchange interaction among the spins can be accounted with the magnetostatic interactions. As a result both the methods lead to a set of simultaneous linear equations[1]. The dynamics of the spins in each cell are then numerically calculated by integrating LLG equation over time by using available micromagnetic solvers. We have listed down different micromagnetic simulation codes and the calculation methods used in those codes[2]. There are both free and commercial software packages.

Free Software Package:

1. Object Oriented Micromagnetic Frameworks (OOMMF)
   Developer: M. Donahue and D. Porter
   Calculation Method: Finite Difference Method (FDM)
   Source website: http://math.nist.gov/oommf

2. NMAG
   Developer: H. Fangohr and T. Fischbacher
   Calculation Method: Finite Element Method (FEM)
   Source website: http://nmag.soton.ac.uk

3. MAGPAR
   Developer: Werner Scholtz
   Calculation Method: Finite Element Method (FEM)
   Source website: http://magnet.atp.tuwien.ac.at/scholz/magpar

Commercial Software Package:

1. LLG Simulator
   Developer: M. R. Scheinfein
   Calculation Method: Finite Difference Method (FDM)
   Source website: http://llgmicro.home.mindspring.com/
2. MicroMagus
   Developer: D. V. Berkov and N. L. Gorn
   Calculation Method: Finite Difference Method (FEM)
   Source website: http://www.micromagus.de

For a particular problem, appropriate modeling strategies and the code should be required in order to obtain reliable numerical simulation results. In micromagnetic simulation a thumb rule is valid for time scales > 1 ps and length scales > 1 nm. According to the continuum micromagnetics all the numerical simulation codes solve LLG equation. In this thesis the ultrafast precessional magnetization dynamics has been simulated by OOMMF software and the LLG micromagnetic simulator calculates magnetostatic stray field profiles. So here we will describe about OOMMF and the LLG micromagnetic simulator.

5.3.2 Object Oriented Micromagnetic Framework (OOMMF)

In OOMMF FDM solves the non-linear LLG equations in micromagnetic framework. Mike Donahue and Don Porter developed this software at the National Institute of Standards and Technology, Gaithersburg, MD in 1999. OOMMF software is written in the platform of C++ and Tcl. In this methodology the sample or space is divided into number of cells of same size and they are often called as ‘finite differences’. At the beginning a file called ‘MIF file’ is written in Tcl script where all the required parameters like bulk saturation magnetization, exchange stiffness constants,

magnetocrystalline anisotropy, Zeeman field, sample structure and dimension and the magnetic field geometry are declared. At the starting point of simulation an initial state of magnetization is provided. When the simulation starts, the evolvers starts to update the magnetization configuration from one step to the next. Mainly two types of evolvers are used, such as (i) time-evolvers, which track Landau-Lifshitz-Gilbert dynamics and (ii) minimization evolvers, which locate the local minima in the energy surface through direct minimization techniques. Time evolver implements a simple first order forward Euler method with step size control on the LLG ODE. Driver control the evolvers so they should be compatible with each other such as time evolver must be paired with time driver as well as minimization evolver be with minimization drivers. In our case we have used time driver and time evolver. It is the role of the drivers, not the evolvers, to determine when a simulation stage or run is complete. Driver detects when stages and runs are finished, using criteria specified in the MIF problem description, and can enforce constraints, such as making sure stage boundaries respect time stopping criteria.

It is the role of the drivers, not the evolvers, to determine when a simulation stage or run is complete. Driver detects when stages and runs are finished, using criteria specified in the MIF problem description, and can enforce constraints, such as making sure stage boundaries respect time stopping criteria.

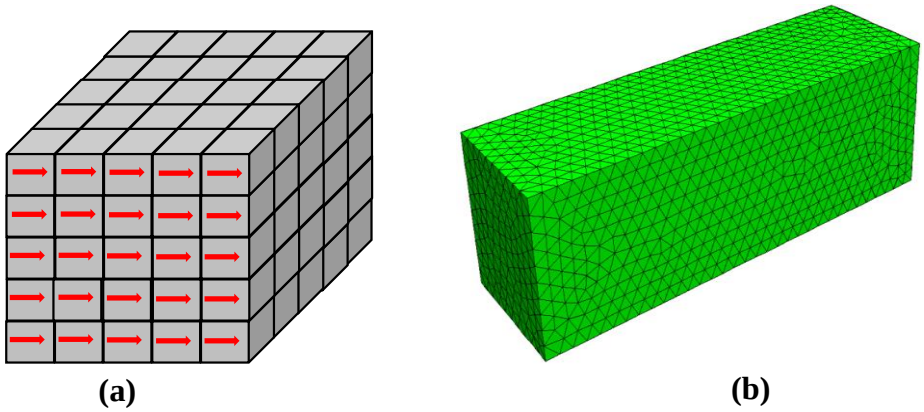

Figure 5.1: The Schematic diagrams which show the discretization of a rectangular sample into a number of (a) cuboidal cells with equal size and (b) tetrahedral cells with varying size.

In simulation setting the stopping value of d$\boldsymbol{m}$/dt or time creates the convergence criteria. The time or value of d$\boldsymbol{m}$/dt is set in such a way that the maximum torque,$\boldsymbol{m}\times\boldsymbol{H}$ (where $\boldsymbol{m}=\boldsymbol{M}/M_s$) goes well below 10^{-6} A/m. At the stopping time the maximum

value of d***m***/dt across all spins drops below the set value. One of the important advantages of this method is that here the demagnetizing field can be computed very efficiently (via fast Fourier transformation techniques).

5.3.3 LLG Micromagnetic Simulator

The LLG Micromagnetic Simulator is a simulation package based on FDM platform[3]. This simulator only works in Windows operating system and it is a full 3-D simulation tool. There is an extra feature in LLG simulator than OOMMF simulator. Here we can incorporate the effect of temperature dependence providing an equivalent random magnetic field. The quasi-static magnetic properties are strongly affected by temperature. So the LLG simulator is helpful for studying the quasi-static magnetization reversal dynamics in magnetic nanostructures. It can also compute equilibrium magnetization distribution in small particles and in thin films, as well as fundamental properties, such as the coercive field, stray fields, switching time, interlayer coupling strength, and vortex and domain wall lengths. In this simulator, magnetization dynamics can be triggered by spin polarized current so that spin valve kind of structures can be also studied using this simulator. The magnetic interaction among magnetic nanoelements also can be visualized by colored contour plot. We have used this feature to calculate the magnetostatic stray field profiles for an array of magnetic dots[4-8], nanoring[9] and antidots[10]. Finally in LLG Micromagnetic Simulator we can control the input magnetic parameters for each layer in a multilayered nanostructures, which is more complicated in OOMMF simulator.

5.3 Methods for Calculation of Power and Phase Profiles of Resonant Modes

We have numerically calculated the power and phase profiles of the resonant modes using Dotmag software developed by our group[11, 12]. At first simulation is done by OOMMF simulator for magnetic nanostructures. From the simulated data we obtain a single file (called .omf files) for each point of simulated time-domain magnetization. The information contained in the file is used to plot the spatial distribution of magnetization of the sample. So, at a particular point of time, the spatial profile shows

a magnetization map which is a superposition of multiple resonant modes present in the system with proper power and phase. To extract the power and phase profiles of a particular resonant mode, at first one spatial co-ordinate (either *x* or *y* or *z*) of the time-dependent magnetization is kept fixed and discrete Fourier transform is performed *with respect to* the time in Dotmag software. The output file plots the space dependent power and phase map at discrete frequencies (*f*). The frequency resolution basically depends on the total simulation time window and the spatial resolution depends on the discretization used in the micromagnetic simulation. In the fast Fourier transform (FFT), if we fix the *z* co-ordinate let's say at $z=z_1$ to obtain the power and phase distribution in the *x*-*y*plane, then we have:

$$\widetilde{M}^{z_1}(f,x,y) = FFT\big(M^{z_1}(t,x,y)\big) \tag{5.15}$$

The power and phase profiles for a particular resonant mode at $f = f_r$ can then be expressed as:

Power: $$P^{z_1,f_r}(x,y) = 20\ log_{10}\left|\widetilde{M}^{z_1}(f_r,x,y)\right| \tag{5.16}$$

Phase: $$\Phi^{z_1,f_r}(x,y) = \tan^{-1}\left[\frac{Im(\widetilde{M}^{z_1}(f_r,x,y))}{Re(\widetilde{M}^{z_1}(f_r,x,y))}\right] \tag{5.17}$$

Bibliography

[1] M. Donahue and D. G. Porter, "OOMMF User's guide, Version 1.0," *NIST Interagency Report Number 6376, National Institute of Standard and Technology, Gaithersburg, MD, URL:* http://math.nist.gov/oommf, City (1999).

[2] S.-K. Kim, *J. Phys. D: Appl. Phys.* **43**, 264004 (2010).

[3] M. R. Scheinfein, "LLG Micromagnetic Simulator," http://llgmicro.home.mindspring.com/, (1997).

[4] B. Rana, D. Kumar, S. Barman, S. Pal, Y. Fukuma, Y. Otani and A. Barman, *ACS Nano* **5**, 9559 (2011).

[5] S. Saha, R. Mandal, S. Barman, D. Kumar, B. Rana, Y. Fukuma, S. Sugimoto, Y. Otani and A. Barman, *Adv. Funct. Mater.* **23**, 2378 (2013).

[6] B. K. Mahato, B. Rana, R. Mandal, D. Kumar, S. Barman, Y. Fukuma, Y. Otani and A. Barman, *Appl. Phys. Lett.* **102**, 192402 (2013).

[7] B. Rana and A. Barman, *SPIN* **3**, 1330001 (2013).

[8] B. K. Mahato, B. Rana, D. Kumar, S. Barman, S. Sugimoto, Y. Otani and A. Barman, *Appl. Phys. Lett.* **105**, 012406 (2014).

[9] C. Banerjee, S. Saha, S. Barman, O. Rousseau, Y. Otani and A. Barman, *J. Appl. Phys.* **116**, 163912 (2014).

[10] R. Mandal, P. Laha, K. Das, S. Saha, S. Barman, A. K. Raychaudhuri and A. Barman, *Appl. Phys. Lett.* **103**, 262410 (2013).

[11] D. Kumar, O. Dmytriiev, S. Ponraj and A. Barman, *J. Phys. D: Appl. Phys.* **45**, 015001 (2012).

[12] G. Venkat, D. Kumar, M. Franchin, O. Dmytriiev, M. Mruczkiewicz, H. Fangohr, A. Barman, M. Krawczyk and A. Prabhakar, *IEEE Trans. Magn.* **49**, 524 (2013).

Chapter 6

Ferromagnetic Thin Film Growth and Characterization

6.1 Introduction

The magnetic properties of ferromagnetic thin film and nanostructured materials have been become a subject of intense research interest during the past two decades for their potential applications in magnetic recording, magnetic storage and related technological applications[1]. Patterned thin film magnetic materials are one of the main subjects of investigation within modern magnetism. The physical properties of those magnetic thin films depend on the method and condition of growth and the substrate nature. The static magnetic properties of the ferromagnetic thin films are studied extensively in literature[2]. The dynamical magnetic properties of these ferromagnetic thin film have been studied experimentally by Brillouin light scattering[2], time-resolved scanning Kerr microscopy[3-7](TRSKM), ferromagnetic resonance[8, 9] and pulsed inductive microwave magnetometry[10].

Ferromagnetic thin films with patterned arrays of antidots have generated considerable scientific interests in the last decade[11-22]. Patterning holes into ferromagnetic thin films is a simple yet effective way to engineer magnetic properties. Arrays of patterned antidots behave like an artificial crystal and this kind of crystal is promoted as the most suitable candidate for magnonic crystals[23-25]. In this thesis we focus on the study of magnetization dynamics of arrays of ferromagnetic antidot arrays by making several structural variations in their geometry. Before fabricating or patterning the thin films we need to characterize the thin films to understand their properties.

In this chapter we will discuss about the growth, patterning and static and dynamic magnetic properties of ferromagnetic blanket thin films of $10 \times 10\ \mu m^2$ and $25 \times 250\ \mu m^2$ lateral dimensions. The thin film that we used for patterning the antidot arrays have thickness of about 20 - 25 nm and it practically behaves like a continuous thin

film with a very minor edge demagnetizing effect even for a 10 × 10 μm^{2}blanket film for a very small thickness/width ratio[26].

6.2 Growth and Fabrication

A silicon wafer Si (100) with a 300 nm silicon-oxide coating is used as a substrate for thin film growth. The Si wafer is cut into square pieces of 20 mm sides and are cleaned to remove all the inorganic and organic contaminations. The square shaped Si substrate is soaked in acetone and ultrasonicated for 10 min at high power. This process is repeated with isopropanol to remove the residual acetone followed by drying the substrate with a N_2 gun flow. Finally, the ultraviolet cleaning of the substrates were performed for 10 min to remove remaining organics on the surface before inserting the substrate into the deposition chamber (Eiko Ultrahigh Vacuum film Deposition System) for thin film growth. We have used Co and $Ni_{80}Fe_{20}$ as a target material for deposition. At a base pressure of 2 × 10^{-8} Torr a very thin Co (25 nm) or $Ni_{80}Fe_{20}$ (20 nm) films were deposited on top of the Si substrate. Those thin ferromagnetic materials are used as a base material for the study of this thesis.

For the work presented in this thesis the antidot lattices were prepared on 10 × 10 μm^2 blanket ferromagnetic (Co or $Ni_{80}Fe_{20}$) thin films instead of continuous thin films. This helps in eliminating any effects coming from the continuous film into the results of the antidot lattices. Those patterned blanket films were made by a combination of photolithography and electron beam evaporation. We have used D-light-DL1000RS mask-less UV photolithography for patterning a two-dimensional array of such blanket films and Eiko Ultrahigh Vacuum Deposition System for depositing the ferromagnetic material. For preparing the substrate for photolithography, we first coated the substrate with a primer (1,1,1,3,3,3,-Hexamethyldisilazane, $C_6H_{10}NSi_2$, HDMS) at 500 rpm for 5 sec and 5000 rpm for 40 sec followed by a soft baking at 80 ^{0}C for 5 min. The AZ-1500 photoresist is spin-coated on top of the primer with a 500 rpm for 5 sec and baked at 80 ^{0}C for 10 min. The spin-coater helps for a uniform distribution of resist throughout the substrate. The baking process removes the solvent in the photoresist and enhances the adhesion between the photoresist and the substrate. The thickness of the photoresist layer was adjusted to about 1 μm

depending upon the viscosity of the resist and the spinning speed[27]. The laser beam is exposed on the substrate surface with typical energy of 90 mJ/mm^2 to draw the two dimensional 10 × 10 μm^2 patterns onto the surface. The ferromagnetic material (Co /$Ni_{80}Fe_{20}$) is then deposited onto the resist pattern using an electron beam evaporator chamber at a base pressure of 2 × 10^{-8} Torr.

Using the same procedure we have prepared another set of $Ni_{80}Fe_{20}$ film of different dimension for the broadband ferromagnetic resonance measurement. A 25 μm × 250 μm × 20 nm thick $Ni_{80}Fe_{20}$ film coated with a 60 nm Al_2O_3 protective layer was deposited in an ultra-high vacuum chamber at a base pressure of 2 × 10^{-8} Torr on a commercially available self-oxidized Si [100] substrate. A co-planar waveguide made of Au with thickness of 150 nm was deposited on top of the thin film at a base pressure of 6 × 10^{-7} Torr for the broadband ferromagnetic resonance measurement. The waveguide has central conductor of 30 μm width, total length of 300 μm and a nominal characteristic impedance of 50 Ω.

6.3 Characterization

The Co or $Ni_{80}Fe_{20}$ blanket thin film as prepared using the methods described in the previous section are characterized by some routine characterization techniques. To check the morphology and surface quality of the blanket thin films we have used scanning electron microscopy[28] (SEM) and atomic force microscopy[29] (AFM). The chemical purity of the thin film is obtained from energy dispersive X-ray (EDX) spectroscopy. The static magnetic properties are investigated by using vibrating sample magnetometer[30] (VSM) (for continuous thin film) and static magneto-optical Kerr effect microscopy (SMOKE) (for blanket thin films). The time-domain magnetization dynamics for 10 × 10 μm^2 blanket thin films is studied by using the time-resolved magneto-optical Kerr effect microscope[31]. On the other hand the ferromagnetic resonance of the 25 × 250 μm^2 blanket film is measured by the broadband ferromagnetic resonance spectrometer.

6.3.1 General Characterization

Figure 6.1 (a) and (b) show the typical scanning electron micrographs of 10 × 10 μm^2 square patterned Co and $Ni_{80}Fe_{20}$ thin film, respectively. The atomic force microscopic image of the 10 ×10 μm^2 $Ni_{80}Fe_{20}$ film is shown in Figure. 6.1(c). The SEM and AFM images shows that the blanket films are reasonably well prepared with small amount of rounded corners and edge roughness. Small amounts of residual resists are observed near the edges of some of the Co blanket films, while the $Ni_{80}Fe_{20}$blanket film is relatively clean.

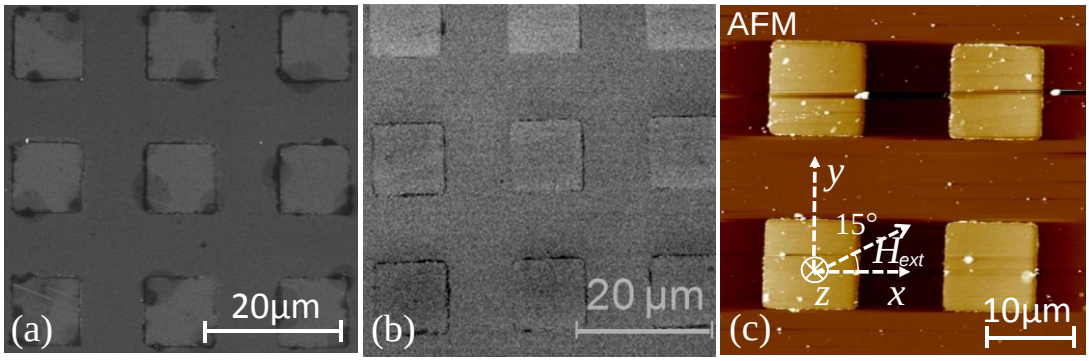

Figure 6.1: Scanning electron micrographs of 10 × 10 μm^2 Cobalt (a) and $Ni_{80}Fe_{20}$ (b) blanket thin films. (c) The atomic force microscopic image of a 10 × 10 μm^2 $Ni_{80}Fe_{20}$ blanket thin film. The geometry of the applied bias field is shown in (c).

In all of our static and dynamic magnetic measurements, we probe the samples with a much smaller the laser spot placed at the middle of the sample. Consequently, no significant effects from the boundaries are expected. To find out the actual thickness of the films we have measured the line scans along *x*-direction by AFM at three different positions on *y*-axis of the square pattern as shown in Figure. 6.2(a). The height profiles at three different y positions in Figure. 6.3(b) show that the thickness of the film is between 31 and 32 nm. This is tabulated in Figure. 6.3 (c). The measured height is found to be consistent with the nominal height which should 20 nm ($Ni_{80}Fe_{20}$ layer thickness) + 10 nm (Al_2O_3 layer thickness) = 30 nm. Similar AFM measurements on other blanket thin films confirmed that the nominal thicknesses of the films are maintained in the real sample.

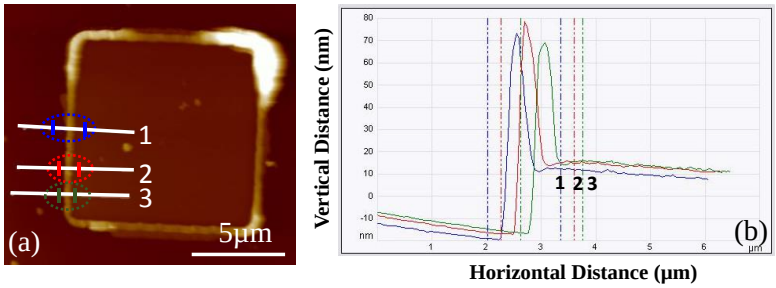

(c)

Position	Thickness (in nm)
1	31.44
2	31.67
3	32.31

Figure 6.2: (a) Topography of a 10 × 10 μm^2 $Ni_{80}Fe_{20}$ pattern. The red, blue and green regions are taken for its thickness measurement. (b) Line scans showing the height profile from those three different regions. (c) The measured heights are tabulated.

To investigate the chemical composition of the thin film we have performed the EDX measurements of the 10 × 10 μm^{2}Co (25 nm) (Figure. 6.3 (a)) and $Ni_{80}Fe_{20}$ (20 nm) (Figure. 6.3 (b)) blanket thin films. In both cases the ferromagnetic material peak is dominant and the capping layer material (Al_2O_3) peaks *i.e.*, the Aluminium (Al) and Oxyzen (O) also appear with appropriate peak amplitude. For the $Ni_{80}Fe_{20}$ film the weight percentages of Ni and Fe are 50.7% and 13.4%, which correspond to a Ni:Fe ratio of 3.9:1, very close to the nominal composition of 4:1. For both Co and $Ni_{80}Fe_{20}$ films a sharp peak at about 2 keV is observed in the EDX spectra corresponds to the base substrate material Si.

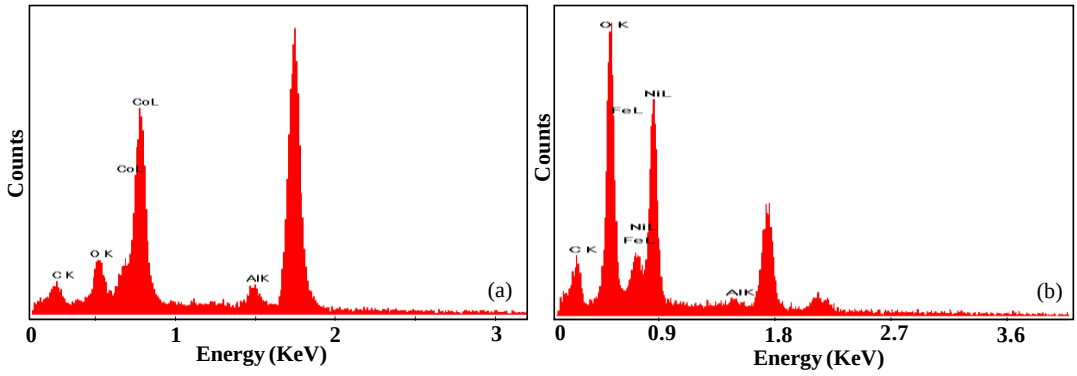

Figure 6.3: EDX spectra of Cobalt (a) and $Ni_{80}Fe_{20}$ (b) blanket thin films.

6.3.2 Static Magnetic Characterization

To investigate the static magnetic properties of continuous ferromagnetic thin films we have used two different tools such as vibrating sample magnetometer (VSM) and static magneto-optical Kerr effect (SMOKE) magnetometer.

The magnetization (M) vs. the applied bias magnetic field (H_{ext}) for 25 nm thick continuous Co films was measured at room temperature (300 K) by using VSM. Figure 6.4 represents the corresponding M-H loop. The loop shows a saturation field of ~50 Oe and coercive field of about 29 Oe.

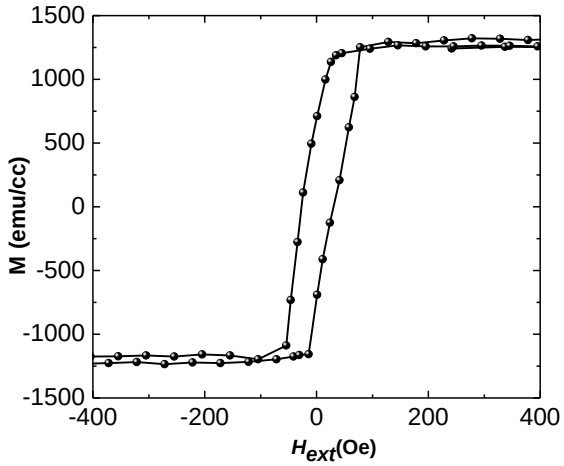

Figure 6.4: M-H_{ext} Loop of a 25 nm thick continuous Co film at room temperature.

For the 10 × 10 μm^2 blanket Co and $Ni_{80}Fe_{20}$ films the magnetic hysteresis loops were measured using a static magneto-optical Kerr effect magnetometer. A linearly polarized CW laser beam having wavelength (λ) of 632 nm from a He-Ne laser is used in this SMOKE set-up. The laser beam, is incident on the sample through an extra-long working distance microscope objective with N.A. = 0.55 and magnification = ×40. The approximate spot size of the laser is 2 μm. The laser beam is incident on an off-axis point on the back aperture of the microscope objective allowing an oblique angle of incidence on the sample. The reflected beam from the sample surface is collected by the same objective and is sent to the detector for measuring the Kerr rotation angle. The magnetic field is applied in the plane of the sample so that longitudinal Kerr effect geometry is maintained during the measurement. The incident

beam was chopped at 1-2 kHz frequency and the detector signal is measured by a lock-in amplifier using the chopper output as a reference to the lock-in so that a phase sensitive detection is done. The focused laser spot is placed at the center of the 10 × 10 μm^2 blanket film. Figure 6.5(a) shows the measured MOKE loop obtained from the blanket (10 μm × 10 μm) Co film. The saturation magnetization field comes out be ~50 Oe while the coercivity field is ~33 Oe in this case.

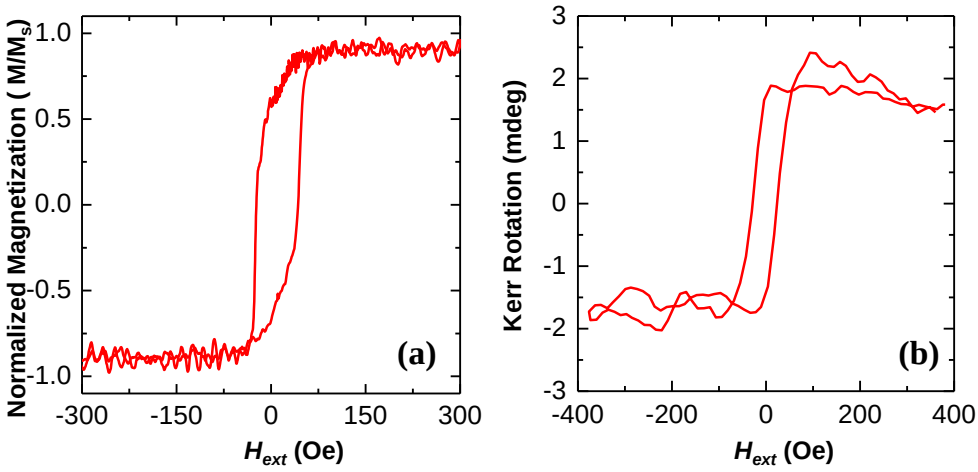

Figure 6.5: Static Magnetic Hysteresis loops of 10 μm × 10 μm Co (a) and $Ni_{80}Fe_{20}$ (b) blanket films.

Figure 6.5(b) shows the MOKE loop from the centre of the $Ni_{80}Fe_{20}$ blanket film. The saturation field is < 50 Oe and the coercive field is ~ 25 Oe in this case.

6.3.3 Magnetization Dynamics of Blanket Ferromagnetic Thin Film

In chapter 7 and 8 we will study the magnetization dynamics of arrays of Co and $Ni_{80}Fe_{20}$ antidot lattices patterned on 10 × 10 μm^2 blanket thin films. In order to understand the dynamics of the antidot lattices, first we measure the magnetization dynamics of the base materials using our all-optical time-resolved magneto-optical Kerr effect microscope[32, 33]. The dynamics was excited by the second-harmonic (λ = 400 nm, pulse width = 100 fs, fluence = 16 mJ/cm^2) of a Ti-sapphire oscillator (Tsunami, Spectra-Physics), while the time-delayed fundamental (λ = 800 nm, pulse width = 70 fs, fluence = 3 mJ/cm^2) laser is used to probe the dynamics of the sample.

The Kerr rotation was measured as a function of the time-delay between the pump and the probe beams. The probe beam is tightly focused to a spot size of about 800 nm on the sample plane at the centre of the blanket film, while the pump beam becomes slightly defocused at the same plane due to chromatic aberration with a spot size of about 1 μm. The probe beam is placed precisely at the centre of the pump beam so that the dynamics is measured from a uniformly excited volume of the sample. The external bias magnetic field is tilted at a small angle (~15°) from the plane of the sample, the in-plane component of which is denoted by H_{ext} (Figure. 6.1(c)). This investigation allows us to extract the magnetic parameters of the material that will be used for the analysis of results from the antidot arrays. The experimental conditions for the measurements of the magnetization dynamics are same for both $Ni_{80}Fe_{20}$ and Co films.

6.3.3.1 Magnetization Dynamics of 10 × 10 μm^2 Co Thin Film

Figure 6.6 (a) shows the polar Kerr rotation of the 10 × 10 μm^2 blanket Co thin film as a function of time delay between the pump and probe beams. An in-plane bias field H_{ext} = 700 Oe is applied during this measurement, which is well above the saturation field of this sample. The polar Kerr rotation data was taken for upto 1500 ps of positive time delay. The time-resolved Kerr rotation data contains three parts, a negative delay where the probe beam arrived the sample before the pump beam and any excitation has happened, a zero delay where the pump and probe beams appears simultaneously to the sample and a positive delay, where the probe beam arrives the sample after the excitation and the pump-induced excitation can be measured. The positive delay shows three different regimes the first one being the ultrafast demagnetization which occurs within sub-ps time scale, a fast remagnetization within about 10 ps and a slow remagnetization which occurs over 100s of ps. To resolve the ultrafast demagnetization and fast remagnetization well the initial 25 ps was measured with a 50 fs resolution, while the following time window is measured with a 5 ps resolution.

The ultrafast demagnetization occurs within about 500 fs due to the phenomenon as described in section 2.4.3 of chapter 2.[35, 36]. After the ultrafast demagnetization the magnetization shows an initial recovery very sharply with a time constant of 8.5 ps (region 3: Figure. 6.6(a)) followed by a slow recovery with a time constant of about

300 ps (region 4: Figure. 6.6(a)). The fast relaxation occurs due to relaxation of spin energy by spin-lattice interaction and the slow relaxation is due to diffusion of electron and lattice energy to the substrate and the surroundings[37]. The precessional dynamics appears as an oscillatory signal on top of the slowly decaying Kerr rotation.

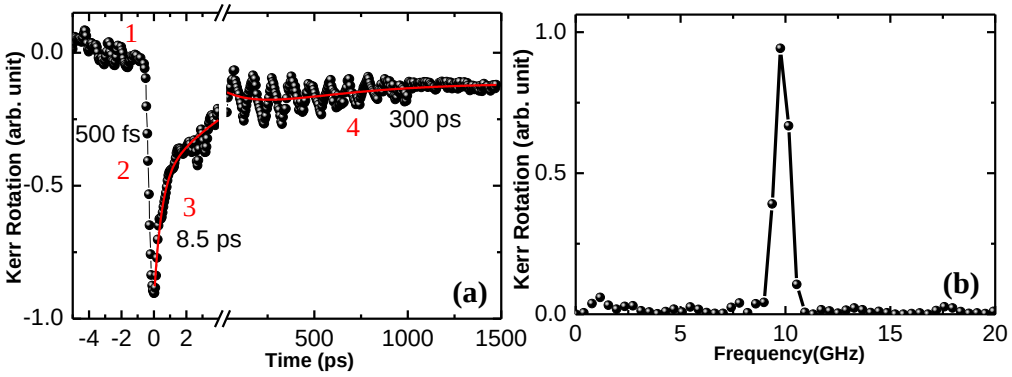

Figure 6.6: (a) A typical time-resolved Kerr rotation data from a 10 × 10 μm^2 blanket Co thin film with 25 nm thickness and a bias field magnitude (H_{ext}) of 700 Oe applied along the positive *x*-axis. Four distinct regions of the time-resolved Kerr rotation are marked by numbers (1, 2, 3 and 4). The solid red lines in region 3 and 4 are the bi-exponential fitting to the data. From the fitting the relaxation time constants are obtained as τ_1 = 8.5 ps and τ_2 = 300 ps. (b) The corresponding fast Fourier transform (FFT) power spectrum of the Kerr signal showing the resonant mode frequency.

To extract the precessional frequency we need to separate out the oscillatory part of the signal and subtract a bi-exponential background corresponding to the two-step remagnetization processes. The fast Fourier transform (FFT) is performed on the bi-exponential background subtracted data to and the corresponding power spectrum reveals the precessional frequency of the blanket Co film at a bias field of H_{ext} = 700 Oe (Figure 6.6 (b)) applied along positive *x*-axis.

The frequency resolution of the FFT power spectrum depends upon the total measurement time window. The precession frequency is extracted by fitting the peak in the power spectrum with a Gaussian function. Use of the Gaussian function includes any possible inhomogeneous line broadening contribution to the peak shape.

The precession frequencies thus extracted for a series of bias field values are then plotted in Figure. 6.7.

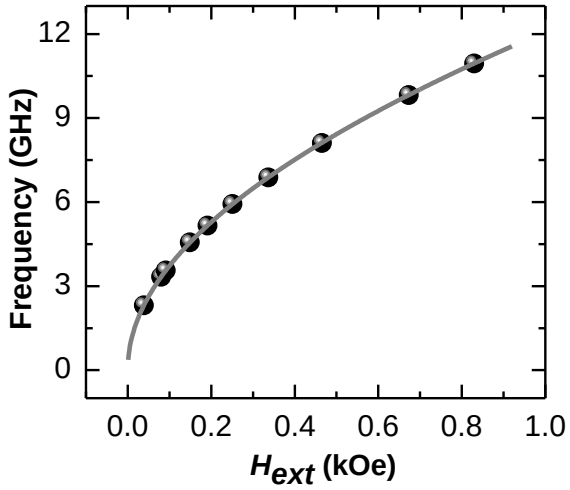

Figure 6.7: Frequency of the single precessional mode is plotted as a function of the bias magnetic field (solid circles). And the solid line corresponds to the fit with the Kittel formula.

Figure 6.7 shows the variation of precessional frequency as a function of the applied bias field. The solid black circles represent the experimentally obtained frequency values, which show an increase with the increase in bias field. The variation of frequency with bias field is fitted with Kittel formula (Eq. 6.1) (solid line for uniform precession of magnetization. The Kittel formula can be expressed as

$$f = \frac{\gamma}{2\pi}\sqrt{(H_{ext} + H_k)(H_{ext} + H_k + 4\pi M_s)} \qquad (6.1)$$

where γ is the gyromagnetic ratio, H_{ext} is the bias field, H_k is the magnetocrystalline anisotropy and M_s is the saturation magnetization. The magnetic parameters are extracted from this fitting for the Co film, which can be used for further analysis of results from the antidot lattices using micromagnetic simulations. The parameter values thus obtained are γ = 17.6 MHz/Oe, $H_k \approx 0$and M_s = 1400 emu/cm^3 for Co.

6.3.3.2 Magnetization Dynamics of 10 × 10 μm^2 $Ni_{80}Fe_{20}$Thin Film

In chapter 8 we will discuss about the effect of antidot shape on the magnonic spectra of an array of $Ni_{80}Fe_{20}$ antidot lattice. Those antidot lattice were fabricated on a 10 × 10 μm^2 $Ni_{80}Fe_{20}$ blanket film. Here, we study the magnetization dynamics of the blanket 10 × 10 μm^2 $Ni_{80}Fe_{20}$ thin film. We have applied an external bias field (H_{ext}) to the $Ni_{80}Fe_{20}$ film in the geometry as shown in Figure. 6.1 (c). The time-resolved

polar Kerr rotation data from the centre of the blanket $Ni_{80}Fe_{20}$ film is shown in Figure. 6.8(a). In this case an ultrafast demagnetization time of about 600 fs and remagnetization time constants of 5.75 ps and 300 ps are observed. The precessional signal is again observed on top of the slowly decaying magnetization. The variation of the single precessional mode with bias magnetic field is extracted and plotted in Figure. 6.8(b) as solid blue circles. The variation of frequency with bias field is again fitted with Kittel formula and the solid line in Figure. 6.8(b) corresponds to the Kittel (Eq. 6.1) fit. From the Kittel fit the magnetic parameters of the blanket $Ni_{80}Fe_{20}$ film are extracted as γ = 17.6 MHz/Oe, $H_k \approx 0$and M_s = 860 emu/cm^3.

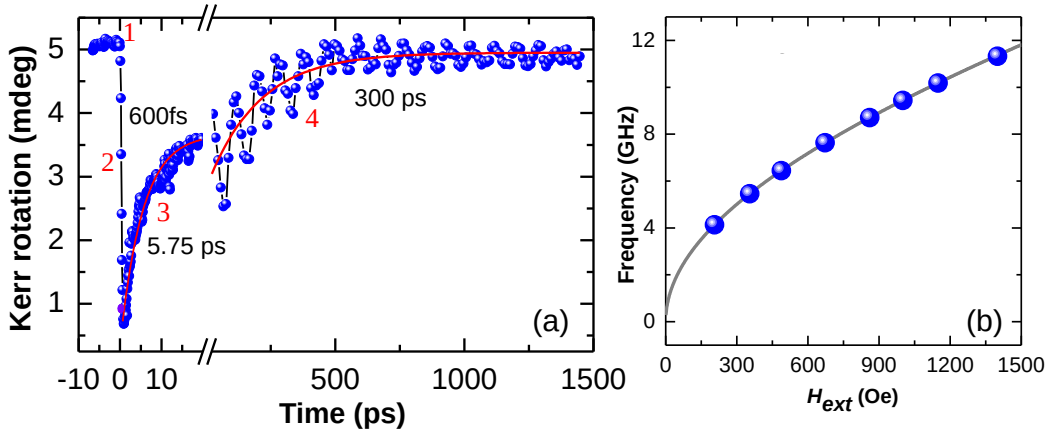

Figure 6.8: (a) A typical time-resolved Kerr rotation data from a 10 × 10 μm^2 blanket $Ni_{80}Fe_{20}$ thin film with 20 nm thickness and a bias field of magnitude (H_{ext}) of 1400 Oe, applied along the positive *x*-axis. The solid red line in region 3 and 4 are the bi-exponential fitting to the data. (b) Frequencies of the uniform precessional mode as a function of the bias magnetic field (solid blue circles) and the fit with the Kittel formula (solid gray line) are shown.

6.3.3.3 Broadband FMR measurement of 25 × 250 μm^2 $Ni_{80}Fe_{20}$ Blanket Thin Film

The spin wave spectra from the 25 × 250 μm^2 blanket thin $Ni_{80}Fe_{20}$ film with 20 nm thickness was measured by a broadband ferromagnetic resonance (FMR) spectrometer[38]. As discussed in section 4.4 of chapter 4 this setup is built using a vector network analyzer (Agilent PNA-L N5230C, 10 MHz to 50 GHz) and a home-made high frequency probe station with nonmagnetic G-S-G type probes (GGB Industries, Model Number 40A-GSG-150-EDP). Inside the probe station an inbuilt

electromagnet is attached which gives an in-plane bias magnetic field upto 2.0 kOe rotatable by 360° within the sample plane. We apply an external bias field (H_{ext}) parallel to the co-planar waveguide (CPW) during the FMR measurement. The frequency of the rf signal has been varied and launched into the CPW structure using the G-S-G type probe. The CPW is shorted at one end and the back reflected signal is collected by the same probe to the analyzer. Absorption of the ongoing and returning signals at various spin wave frequencies produces the characteristic spin wave spectrum of the sample. The real and imaginary parts of the scattering parameter in the reflection geometry (S_{11}) at various bias fields are subtracted from its value at the maximum bias field (reference spectrum) and the spin wave spectra are obtained.

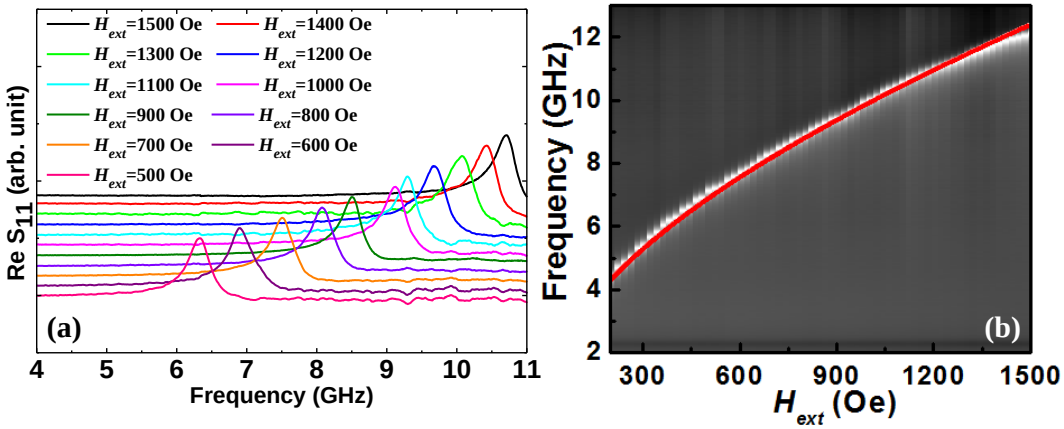

Figure 6.9: (a) Real part of S_{11} is plotted as a function of frequency of the rf signal. Curves are shown at different values of the bias magnetic field, H_{ext}. (b) Surface plots of a number of FMR spectra at varying bias field values. The variation of frequency with bias field is modelled using Kittel formula shown by the symbols.

Figure 6.9(a) shows the real part of S_{11} parameter as a function of external applied bias field (H_{ext}) for the 25× 250 μm^2 $Ni_{80}Fe_{20}$ thin film from 500 Oe to 1500 Oe at a 100 Oe spacing. The surface plot (Figure. 6.9(b)) of frequency over a broad range (200 to 1500 Oe at 20 Oe resolution) of H_{ext} shows that the frequency is decreases with the decrease in applied bias field. The variation of frequency vs. H_{ext} is modelled by using Kittel formula as shown by symbols in Figure. 6.9(b). The magnetic parameters obtained for the fitting are γ = 18.1 MHz/Oe, $H_k \approx 0$and M_s = 860 emu/cm^3. These will be further used for modelling of the spin wave spectra obtained from the $Ni_{80}Fe_{20}$ antidot lattices with varying lattice symmetry as presented in chapter 9.

6.4 Conclusion

In summary we have characterized the continuous and blanket Co and $Ni_{80}Fe_{20}$ thin films with different dimensions by various routine characterization methods. In addition, we measured the ultrafast magnetization dynamics of these thin films by using time-resolved MOKE microscope and broadband ferromagnetic resonance spectrometer. The blanket films are found to have a good quality with small amount of rounded corners and edge roughness. However, due to their very small thickness/width ratio the edge demagnetization effects are very small in these samples and would not affect the static and dynamic magnetic properties of the overall sample. In addition, the time-resolved magnetization dynamics is measured by a focused laser spot of much smaller sized placed at the centre of the blanket film and hence edge effect would be negligible. The static magnetic characterization by the VSM and static MOKE techniques gave some initial ideas about the magnetic behavior of the samples. The magnetization dynamics of the blanket films are measured by time-resolved MOKE and broadband ferromagnetic resonance spectrometer. A single resonant mode corresponding the uniform precessional dynamics is observed in all cases. The variation of precession frequencies with bias magnetic field are modelled by Kittel formula and the magnetic parameters are extracted, which will be further used for micromagnetic simulations of the various antidot lattices investigated in chapters 7 to 9.

Bibliography

[1] G. Prinz and e. K. H., pp. 24–63, *Physics Today (AIP, New York), special issue on the subject*, (1995).

[2] J. Jorzick, S. O. Demokritov, B. Hillebrands, M. Bailleul, C. Fermon, K. Y. Guslienko, A. N. Slavin, D. V. Berkov and N. L. Gorn, *Phys. Rev. Lett.* **88**, 047204 (2002).

[3] W. K. Hiebert, A. Stankiewicz and M. R. Freeman, *Phys. Rev. Lett.* **79**, 1134 (1997).

[4] Y. Acremann, A. Kashuba, M. Buess, D. Pescia and C. H. Back, *J. Magn. Magn. Mater.* **239**, 346 (2002).

[5] J. P. Park, P. Eames, D. M. Engebretson, J. Berezovsky and P. A. Crowell, *Phys. Rev. Lett.* **89**, 277201 (2002).

[6] A. Barman, V. V. Kruglyak, R. J. Hicken, A. Kundrotaite and M. Rahman, *Appl. Phys. Lett.* **82**, 3065 (2003).

[7] A. Barman, V. V. Kruglyak, R. J. Hicken, J. Scott, A. Kundrotaite and M. Rahman, *J. Appl. Phys.* **95**, 6998 (2004).

[8] Y. Zhai, J. Shi, X. Y. Zhang, L. Shi, Y. X. Xu, H. B. Huang, Z. Lu and H. R. Zhai, *J. Phys.: Condens. Matter* **14**, 7865 (2002).

[9] G. N. Kakazei, P. E. Wigen, K. Y. Guslienko, V. Novosad, A. N. Slavin, V. O. Golub, N. A. Lesnik and Y. Otani, *Appl. Phys. Lett.* **85**, 443 (2004).

[10] T. M. Crawford, M. Covington and G. J. Parker, *Phys. Rev. B* **67**, 024411 (2003).

[11] C. T. Yu, H. Jiang, L. Shen, P. J. Flanders and G. J. Mankey, *J. Appl. Phys.* **87**, 6322 (2000).

[12] P. Vavassori, G. Gubbiotti, G. Zangari, C. T. Yu, H. Yin, H. Jiang and G. J. Mankey, *J. Appl. Phys.* **91**, 7992 (2002).

[13] L. J. Heyderman, F. Nolting, D. Backes, S. Czekaj, L. Lopez-Diaz, M. Kläui, U. Rüdiger, C. A. F. Vaz, J. A. C. Bland, R. J. Matelon, U. G. Volkmann and P. Fischer, *Phys. Rev. B* **73**, 214429 (2006).

[14] A. O. Adeyeye, J. A. C. Bland and C. Daboo, *Appl. Phys. Lett.* **70**, 3164 (1997).

[15] W. Y. Lee, H. T. Leung, W. Zhang, Y. B. Xu, A. Hirohata, C. C. Yao, B.-C. Choi, D. G. Hasko and J. A. C. Bland, *IEEE Trans. Magn.* **35**, 3475 (1999).

[16] C. C. Wang, A. O. Adeyeye and Y. H. Wu, *J. Appl. Phys.* **94**, 6644 (2003).

[17] M. J. Van Bael, S. Raedts, K. Temst, J. Swerts, V. V. Moshchalkov and Y. Bruynseraede, *J. Appl. Phys.* **92**, 4531 (2002).

[18] A. Y. Toporov, R. M. Langford and A. K. Petford-Long, *Appl. Phys. Lett.* **77**, 3063 (2000).

[19] O. Martyanov, V. Yudanov, R. Lee, S. Nepijko, H. Elmers, R. Hertel, C. Schneider and G. Schönhense, *Phys. Rev. B* **75**, 174429 (2007).

[20] S. McPhail, C. Gürtler, J. Shilton, N. Curson and J. Bland, *Phys. Rev. B* **72**, 094414 (2005).

[21] M. Yu, L. Malkinski, L. Spinu, W. Zhou and S. Whittenburg, *J. Appl. Phys.* **101**, 09F501 (2007).

[22] C. Yu, M. J. Pechan, W. A. Burgei and G. J. Mankey, *J. Appl. Phys.* **95**, 6648 (2004).

[23] V. V. Kruglyak, S. O. Demokritov and D. Grundler, *J. Phys. D: Appl. Phys.* **43**, 264001 (2010).

[24] B. Lenk, H. Ulrichs, F. Garbs and M. Münzenberg, *Phys. Rep.* **507**, 107 (2011).

[25] S. O. Demokritov and A. N. Slavin, "Magnonics: From Fundamentals to Applications," *Springer*, (2013).

[26] A. Barman, V. V. Kruglyak, R. J. Hicken and J. M. Rowe, *Phys. Rev. B* **69**, (2004).

[27] J. I. Martín, J. Nogués, K. Liu, J. L. Vicent and I. K. Schuller, *J. Magn. Magn. Mater.* **256**, 449 (2003).

[28] D. McMullan, *Scanning* **17**, 175 (1995).

[29] L. Gross, F. Mohn, N. Moll, P. Liljeroth and G. Meyer, *Science* **325**, 1110 (2009).

[30] S. Foner, *Rev. Sci. Instrum.* **30**, 548 (1959).

[31] B. Rana and A. Barman, *SPIN* **3**, 1330001 (2013).

[32] A. Barman, S. Wang, J. D. Maas, A. R. Hawkins, S. Kwon, A. Liddle, J. Bokor and H. Schmidt, *Nano Lett.* **6**, 2939 (2006).

[33] B. Rana, D. Kumar, S. Barman, S. Pal, Y. Fukuma, Y. Otani and A. Barman, *ACS Nano* **5**, 9559 (2011).

[34] L. Guidoni, E. Beaurepaire and J.-Y. Bigot, *Phys. Rev. Lett.* **89**, 017401 (2002).

[35] J.-Y. Bigot, M. Vomir and E. Beaurepaire, *Nat. Phys.* **5**, 515 (2009).

[36] A. Laraoui, J. Vénuat, V. Halté, M. Albrecht, E. Beaurepaire and J.-Y. Bigot, *J. Appl. Phys.* **101**, 09C105 (2007).

[37] B. K. Mahato, S. Choudhury, R. Mandal, S. Barman, Y. Otani and A. Barman, *J. App. Phys.* **117**, 213909 (2015).

Chapter 7

Optically Induced Tunable Magnetization Dynamics in Nanoscale Co Antidot Lattices with Varying Lattice Constants

7.1 Introduction

Nanoscale ferromagnetic antidot (hole) lattices have emerged as a system of intense interest as magneto-photonic crystals due to the influence of magnetic field on the light coupling to surface plasmons[1-3]. Magnetic antidots have also been considered as a candidate for ultrahigh density data storage devices[4], so that the memory bit could be trapped between consecutive holes along the intrinsic hard axis of the antidot nanostructure[5]. The antidots have some advantages at the deep nanoscale dimensions due to the absence of any isolated small magnetic entity and they do not suffer from the superparamagnetic bottleneck. However, one of their most exciting prospects is in the magnonic crystals[6-8], where the magnonic band structures can be manipulated by the periodic arrays of magnetic antidots. Magnonic crystals are spatially modulated magnetic mediums, analogous to photonic or phononic crystals in the microwave band, which may open up magnonic bandgaps for the propagating magnons leading towards the applications in on-chip nanoscale microwave communications. The periodic modulation is not only limited at the physical boundaries of the antidots but also at the strong pinning centres for spin waves created by the demagnetized regions between the antidots. Magnetic antidot lattices are exchange coupled magnetic systems as opposed to the magnetostatically coupled magnetic dot lattices and hence offer much higher propagation velocity (steeper frequency vs. wavevector dispersion) and longer propagation length for the magnons than the dot lattices before the excitation is decayed. More recently filled antidots have raised interests as bi-component magnonic crystals[9, 10], where the differences between the magnetic parameters of two magnetic mediums provide additional tunability in the magnonic band structures.

One of the important issues regarding the various applications of magnetic antidot lattices is the successful fabrication of good quality structures with smaller dimensions and the time-domain detection of the magnetization dynamics in such materials. So far, the reported experimental results have been primarily confined to antidots with micrometer to several hundreds of nanometers of dimensions[5, 11-22]. The lithographic techniques including e-beam lithography and focused ion beam lithography often creates defects at the edges of the antidots at the deep nanometer scale providing additional pinning regions, which may significantly modify the magnonic spectra of the intrinsic lattice. On the other hand, the measurements of magnetization dynamics of magnetic antidot lattices have been primarily done by Brillouin light scattering[14-17, 19, 21]and broadband ferromagnetic resonance measurements[11, 16-18, 20, 23], while there is only a single report on the time-domain observation of precessional dynamics from microscale CoFeB antidot lattices[24]. In the early works, attenuation of uniform ferromagnetic resonance mode due to the excitation of non-uniform in-plane spin wave mode[20] and pattern induced frequency splitting of propagating spin waves[19] were observed. More recently field controlled and anisotropic propagation[17, 25] of spin waves, spin wave localization[18, 25], and magnonic miniband formation with large spin wave velocities[16] have attracted attentions. Further experiments such as spatial control of spin wave modes in bi-component antidots[10] and angular variation of the dynamics by tailoring lattice symmetry[15, 26] have been initiated.

However, tunability of magnonic bandgaps with the variation of physical parameters of the nanoscale antidot lattices and understanding the origin of such tunability has not been reported in the literature. Here, we report the fabrication of high quality Co antidot lattices with 100 nm antidot diameters and with lattice constant (*S*) varying between 200 and 500 nm. We have excited and detected the precessional dynamics in the antidot lattices by an all-optical method. We observe a significant variation in the dynamics with the variation in the lattice constant, including a tunable gap in the magnonic spectra from the experimental results and micromagnetic simulations. Finally, we propose composite antidot structures with very rich magnonic spectra based upon the above observation.

7.2 Sample Fabrication and Measurement Technique

7.2.1 Fabrication

Square arrays of Co antidots were prepared on 10 × 10 μm^2 blanket Co films by focused ion beam lithography. Arrays of 10 × 10 μm^2 resist patterns were first prepared on Si/SiO_2 substrate by UV photolithography. The Co film was deposited onto the resist pattern by e-beam evaporation at a base pressure of about 2×10^{-8} Torr. A 10 nm thick SiO_2 capping layer was deposited on top of Co film to protect the sample from degradation when exposed to the optical pump-probe experiments in air. This is followed by the lifting off of the sacrificial material to obtain the blanket Co films. In the next step, the antidot arrays are fabricated on the blanket Co films by using focused liquid Ga^+ ion beam lithography (Helios NANOLAB 600, dual beam FIB). The optimal parameters for milling were found to be 30 kV voltage and 28 pA current. In FIB the spot size used for milling need be optimized not only for creating repetitive nanopatterns with high fidelity but also to ensure that the material that has been retained after patterning (Co films in this case) does not have excessive Ga^+ ion implantations. The spot size is a function of the beam current. We have used a beam current of 28 pA that gives sufficient etch rate yet limits the spot size to around 8 nm. The thickness of the Co film (25nm) is smaller than the stopping range of Ga^+ ions at 30keV, which ensures that the ions stop within the SiO_2layer underneath the film. There are two types of damage that can occur on the Co film during the milling process. One is the direct damage that affects the edges of the holes due to direct beam of finite width. The other is the struggling of the ion beam that causes lateral implantation in the bulk of the film along the edges. The presence of 10 nm thick SiO_2 capping layer protects the un-milled Co film to a large extent from direct irradiation. However, there will be some finite damages at the edges of the antidots due to Ga^+ ion implantation occurring laterally. Simulations of ion trajectory and damage profile on Co (25 nm)/SiO_2 (10 nm) film using the experimental parameters show that the lateral damages are located within about 5 nm from the edges. This is much less than the antidot separation (*S*) thus ensuring that predominant magnetization precession occurs in regions that does not have appreciable defects. The initial preparation of the 100 nm holes was done by focused ion beam milling at 30 kV voltage in single pass. The redepositions occurred during the initial milling were then removed by a final

milling at 2 kV voltage in multipass mode (200 passes), which makes the holes much cleaner with uniform edges. The circular holes were made with fixed 100 nm antidot diameters and with variable lattice constants of 200, 300 400 and 500 nm. Figure 7.1 presents the scanning electron micrographs of the lattices, which show that the samples are generally well fabricated with small deviations in the antidot diameters and lattice constants, which will eventually be included in the micromagnetic simulations to the extent possible under the finite difference method.

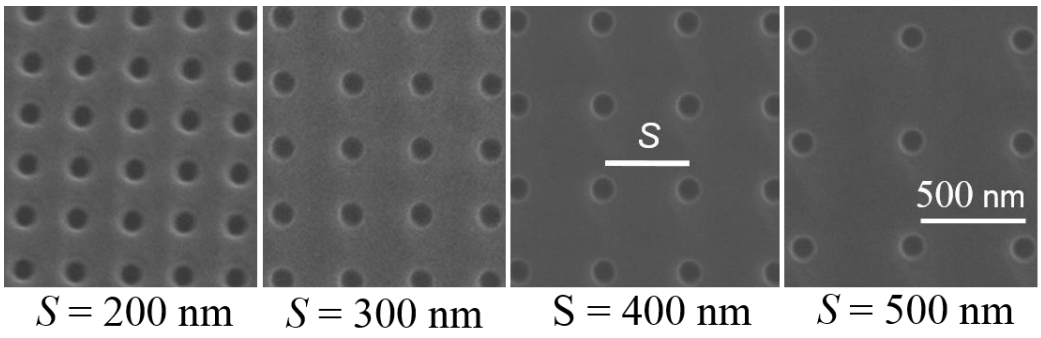

Figure 7.1: Scanning electron micrographs of the antidot lattices with width W = 100 nm and with variable lattice constant *S*.

7.2.2 Measurement

The ultrafast magnetization dynamics was measured by using a home-built time-resolved magneto-optical Kerr effect microscope[27] based upon a two-color collinear pump-probe set-up (Figure. 7.2). The second harmonic (λ = 400 nm, pulse width ~ 100 fs, average power = 10 mW) of a Ti-sapphire laser (Tsunami, Spectra Physics, pulse width ~ 70 fs) was used to pump the samples, while the time-delayed fundamental (λ = 800 nm, average power = 2.5 mW) laser beam was used to probe the dynamics by measuring the polar Kerr rotation by means of a balanced photo-diode detector. The probe beam is focused to a spot size of 800 nm and placed at the centre of each lattice by a microscope objective with numerical aperture N.A. = 0.65. The pump beam is spatially overlapped with the probe beam after passing through the same microscope in a collinear geometry.

A large magnetic field is first applied at a small angle (~ 15°) to the sample plane to saturate its magnetization. The bias field was tilted at 15° angle from the plane of the sample (H_{ext} = component of the bias field along x-direction) (Figure. 4.11) to have a

finite demagnetizing field along the direction of the pump pulse, which is eventually modified by the pump pulse to induce precessional magnetization dynamics within the samples. The magnetic field strength is then reduced to the bias field value, which ensures that the magnetization remains saturated along the bias field direction. The pump beam was chopped at 2 kHz frequency and phase sensitive detections of the Kerr rotation and reflectivity were measured.

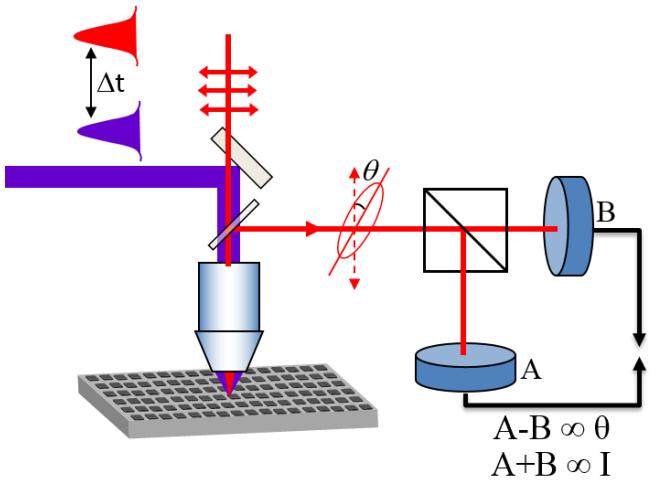

Figure 7.2: A schematic diagram of the time-resolved Kerr microscope.

7.3 Time-Resolved Precessional Dynamics of Array of Co Antidot Lattices with Varying Lattice Constant

The precessional dynamics appears as an oscillatory signal above the slowly decaying part of the time-resolved Kerr rotation signal after a fast demagnetization within 500 fs, and a fast remagnetization within 10 ps (Figure. 7.3). The schematic of the measurement setup is shown in Figure. 7.2. A bi-exponential background is subtracted from the time-resolved Kerr signal before performing the fast Fourier transform (FFT) to find out the corresponding power spectra. The reflectivity data, on the other hand, shows a sharp increase at zero delay and a bi-exponential decay.

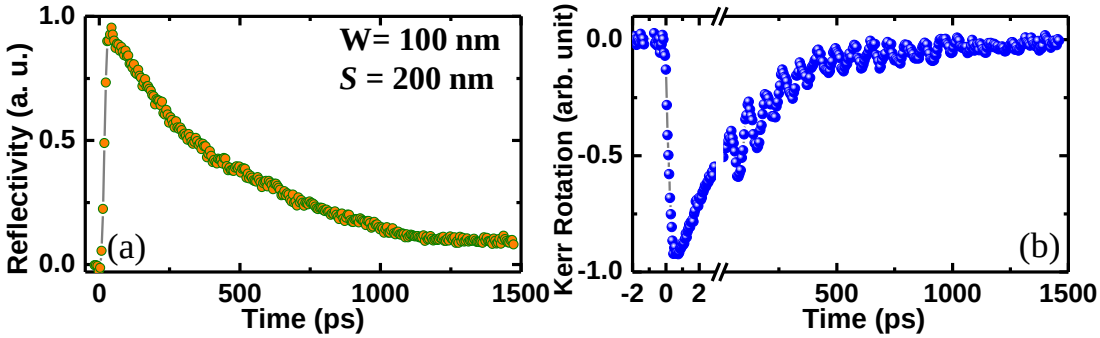

Figure 7.3: The time-resolved reflectivity and Kerr rotation for the antidot lattice with S = 200 nm at a bias field H_{ext} = 0.9 kOe.

The magnetization dynamics of a 10 × 10μm^{2}square Co film was measured at varying bias field values by placing the pump and probe beams at the centre of the pattern as already described in chapter 6. The FFT spectra show a single precession frequency, which is plotted as a function of the bias field in Figure. 7.4.The experimental data is fitted with the Kittel's formula for the uniform precession of magnetization as given in Eq. 7.1.

$$f = \frac{\gamma}{2\pi}\sqrt{(H_{ext} + H_k)(H_{ext} + H_k + 4\pi M_s)} \tag{7.1}$$

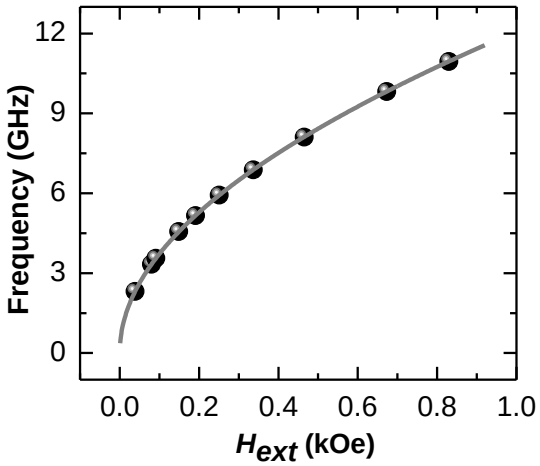

Figure 7.4: The experimental precession frequencies (symbols) as a function of the bias magnetic field for a 10 × 10 μm^2 Co film with 25 nm thickness and the fit to the Kittel's formula (solid curve).

The magnetic parameters extracted from the fit are gyromagnetic ratio γ = 17.6 MHz/Oe, magneto crystalline anisotropy field $H_K \approx 0$, and the saturation magnetization M_S = 1400 emu/cc. These magnetic parameters will later be used in micromagnetic simulations of the Co antidot structures. Figure 7.5(a) shows the

background subtracted time-resolved Kerr rotation data and the corresponding FFT spectra (Figure. 7.5(b)) from the Co antidot lattices with varying lattice constants from 200 to 500 nm at H_{ext}= 0.9 kOe. In Figure 7.5(b) we show the precession frequency of the unpatterned thin film as a vertical dotted line. Two clear bands of modes are observed for S = 500, 400 and 300 nm and the bandgap increases consistently and significantly with the reduction of S. The frequency of the dominant resonant mode (mode 2) for S = 500 nm is very close to that of the unpatterned thin film but with the decrease in S the position of this peak shifts slightly towards lower frequency. This is due to the relative increase in the demagnetized regions between the antidots, which produces lower effective fields in these regions as opposed to the unpatterned thin film as shown later in this article. The higher frequency peak (mode 1) on the other hand shifts to even higher frequency with the decrease in S and the bandgap opens up further. At S = 200 nm a drastic change occurs in the frequency spectra and four clear bands of modes appear in the frequency range between 3 and 26 GHz.

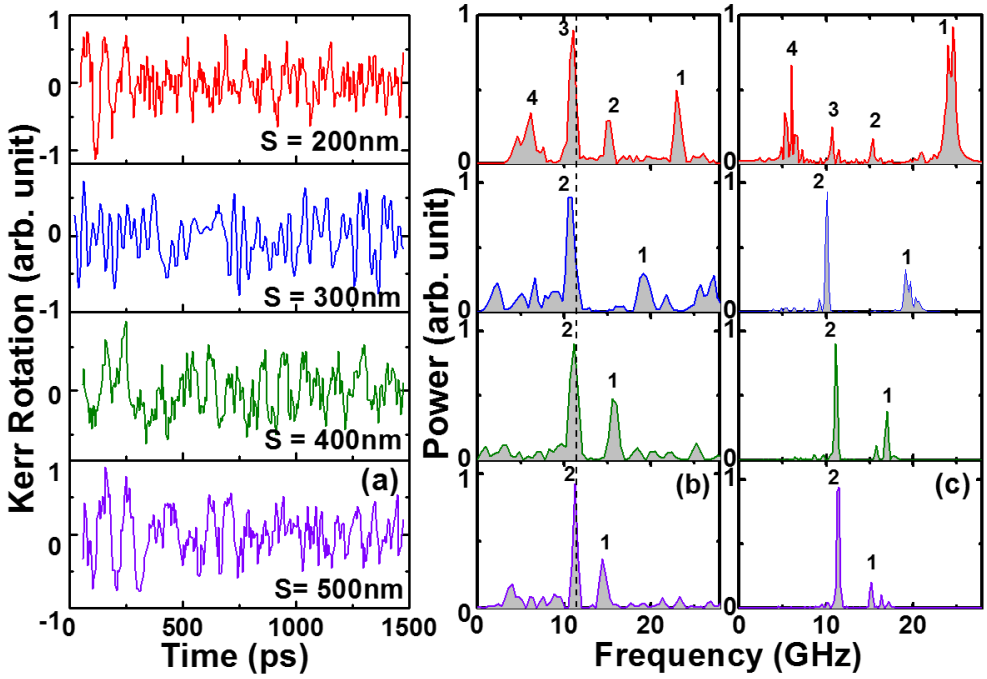

Figure 7.5: (a) The measured time-resolved Kerr rotations and (b) the corresponding FFT spectra are shown for antidot lattices with variable lattice constants at H_{ext} = 0.9 kOe. (c) The FFT spectra of the simulated time-resolved magnetization. The mode numbers are assigned to the peaks of each band.

7.4 Micromagnetic Simulation

We have performed micromagnetic simulations using the OOMMF software[28]by considering finite arrays of 7 × 7 antidots with varying lattice constants.The static configuration at the applied bias field was obtained by first applying a large field to saturate the sample and then by reducing the field to bias field value and allowing the system to reach the equilibrium (maximum torque $\boldsymbol{m} \times \boldsymbol{H}$ where $\boldsymbol{m} = \boldsymbol{M}/M_S$, goes well below 10^{-6} A/m). The dynamics was obtained by applying a pulsed magnetic field and by calculating the spatial distribution of magnetization at time steps of 5 ps for a total duration of 4 ns. The convergence criterion for the dynamic calculation is set on the time steps. The spatial profile of the power and phase information for various resonant modes are obtained by fixing one of the spatial co-ordinates in the space and time dependent magnetization $M_{z_o}^{k}(t, x, y, z)$ and by performing a discrete Fourier transform *with respect to* time-domain.Figure 7.5(c) shows the FFT spectra of the simulated time-domain magnetizations for all four samples. The simulations qualitatively reproduce the observed features although the precise values of the frequencies and relative intensities are not always reproduced. This is expected due to the deviation of the simulated samples and conditions from the experimental samples and conditions. In general, the deviation in the dimensions as observed in the experimental samples are included in the simulated samples but the precise edge roughness profiles are not possible to include in the finite difference method based micromagnetic simulations used here, where samples are divided into rectangular prism like cells. The simulated arrays are much smaller (7 × 7 antidots) than the experimental samples (upto 50 × 50 antidots) due to the limitation in the computational resources. Possible changes in the magnetic parameters in the Ga^+ implanted regions could not be characterized and included in the simulation. Finally, the optical excitation in the experimental sample is simulated as an effective pulsed magnetic field induced excitation. Despite all these deviations, we observe the increase in the bandgap between two frequency bands as *S* varies from 500 to 300 nm, and occurrence of four frequency bands for *S* = 200 nm from the simulation. Figure 7.6 (a) shows the bias field dependence of the resonant mode at around 11 GHz in the magnonic spectra for the antidot lattices with *S* = 200 nm and 500 nm. The mode frequencies for the lattice with *S* = 200 nm is slightly downshifted from those for the

lattice with S = 500 nm. This solid curves show the fit with the Kittel's formula and the extracted effective magnetization for the two different lattices are 1310 emu/cc and 1380 emu/cc, respectively. This is confirmed by the simulated spatial distribution of magnetization (Figure. 7.6(b), which shows the fraction of the demagnetized volume increases with the decrease in the lattice constant. The average magnetization values calculated from Figure. 7.6(b) are identical to the values obtained from the fit to the Kittel's formula. In Figure. 7.6(c) we show the simulated internal field maps, which resembles the magnetization maps and would play key roles in the spatial profiles of the resonant modes, as described below.

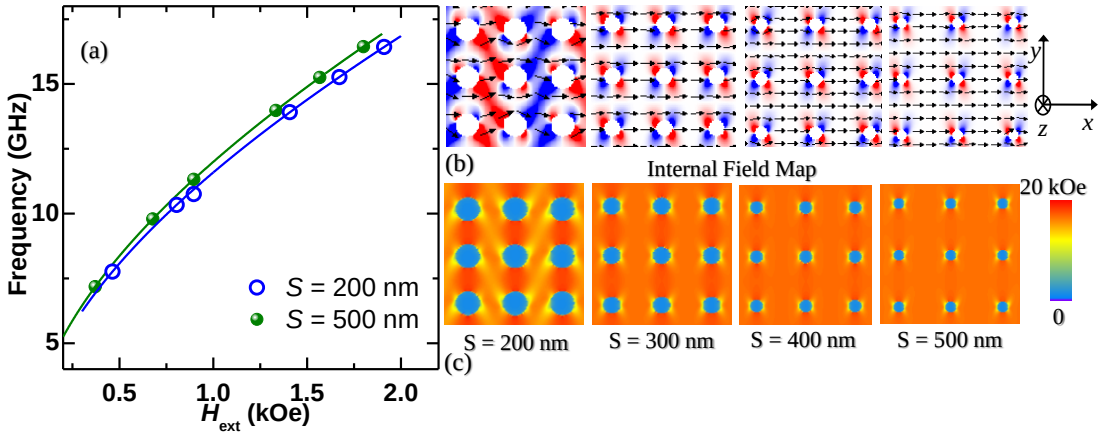

Figure 7.6: (a)The experimental precession frequencies (symbols) and the fit to Kittel's formula (solid curve) for two antidot lattices with S = 200 and 500 nm. The projection on the x-y plane of the spatial maps of (b) magnetization and (c) the internal field for the Co antidot lattices with lattice constants S = 200, 300, 400 and 500 nm. The y-component of magnetization is represented by blue-white-red colormaps, while the colormap for the internal field is shown next to (c).

7.5 Power and Phase Profiles of Resonant Modes

In order to understand the mode profiles corresponding to each resonant peak, we have calculated the power and phase maps of the resonant modes by using a home built code[29]. Due to the finite size of the array the boundaries of the arrays experience non-uniform magnetostatic environment and consequently show boundary effect. Hence, we concentrate on 3 × 3 antidots from the centre of the simulated lattices, for which the magnetostatic environment is almost identical. Figure 7.7 shows the power and phase maps for the main resonant peaks for antidot lattices with S = 500, 400, 300

and 200 nm. The bias field is applied parallel to the horizontal edges of the samples. The high frequency mode (mode 1) for 500 nm ≤ *S* ≤ 300 nm corresponds to quantized spin wave modes with quantization axis perpendicular to the bias field. On the other hand, the low frequency mode (mode 2) corresponds to extended spin wave mode with wave vector perpendicular to the applied bias field *i.e.*, in the magnetostatic surface wave (MSSW) mode geometry. The frequency of this mode is slightly reduced than the unpatterned thin films because of the modulation by the antidot structures and the ensuing demagnetized regions around the antidots. With the decrease in the lattice parameter the quantization number of the spin wave modes for the mode 1 reduces, while mode 1 remains identical with a slight reduction in the amplitude down to S = 300 nm. However, a drastic change occurs at *S* = 200 nm. For *S* = 200 nm, mode 1 and mode 2 are quantized modes with quantization axis parallel to the diagonal of the antidot lattice (rotated by 45° from those observed in 500 nm ≤ *S* ≤ 300 nm). Mode 3 is identified as the MSSW mode with much reduced intensity, while mode 4 has a modulated MSSW like profile.

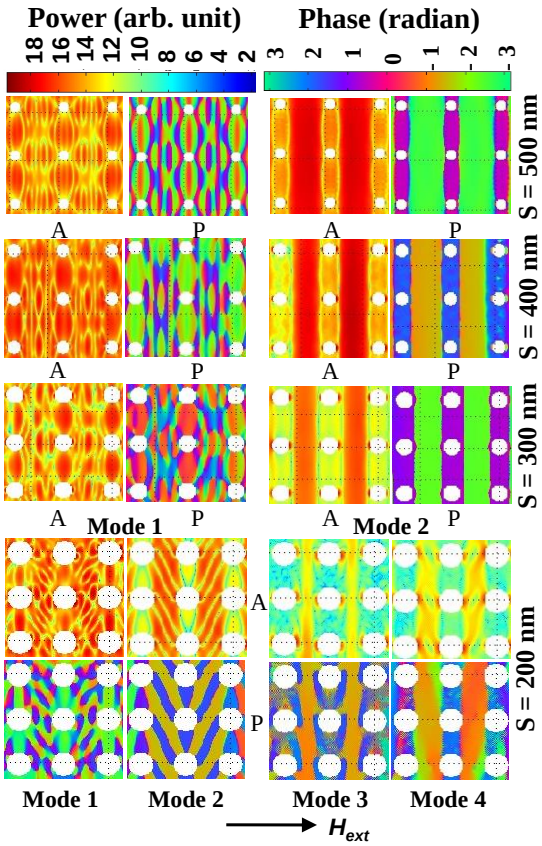

Figure 7.7: The simulated power (A) and phase (P) maps of different resonant modes for the antidot lattices with lattice constants *S* = 500, 400, 300 and 200 nm. The colormap for the power and phase distributions are shown at the top of the figure.

7.6 Magnonic Spectra of Composite Antidot Structures

The tunability of magnonic spectra including the magnonic bandgap can be applied to design nanoscale microwave filters in the form of a composite antidot structure formed of variable lattice constants. In order to demonstrate that we have considered three different composite antidot structures with variable lattice constants arranged in a checkerboard pattern, and patterns consist of and radially increasing and decreasing lattice constants. Figure 7.8 shows the numerically calculated magnonic spectra for three different composite structures along with their static magnetic configurations in the inset. In all three structures rich magnonic spectra are observed. However, the bandwidth is maximum (27 GHz) for the structure shown in the middle panel, while the numbers of bands vary with the geometry of the structure (11 bands for the checkerboard pattern and 8 bands each for the other two structures). The observed spectra clearly go beyond the linear superposition of the bands observed for the constituent lattices.

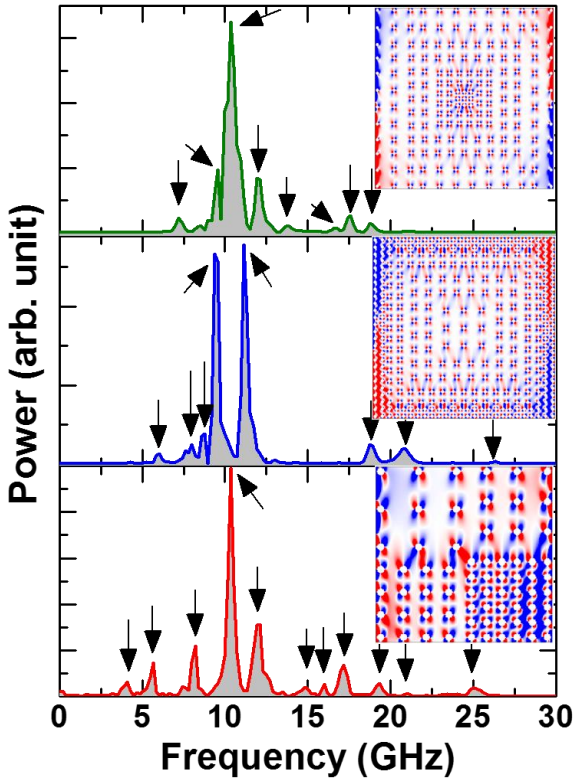

Figure 7.8: Simulated magnonic spectra of composite antidot structures consisting of arrays of square lattices with variable lattice constants arranged in three different geometries. The simulated static magnetization configurations of the composite structures are shown in the inset. The arrows indicate various peaks observed in the magnonic spectra.

More importantly, the arrangement of the constituent lattices in the composite structure plays an important role in determining the magnonic spectra both qualitatively and quantitatively. This is because of the geometry dependent creation of additional demagnetization regions in the composite structures, which is more prominent in the checkerboard pattern due to the sudden variation in the lattice constants at the joining regions and less prominent in the other two structures due to the continuous variation in the lattice constants in the structures. This is also evident in the static magnetic configurations of the three structures. The dependence of magnonic spectra on the arrangements of the constituent lattices in the composite structures provides an additional control parameter in the design of magnonic devices based upon composite antidot structures.

7.7 Summary

In summary we have fabricated high quality Co antidot lattice structures by using focused ion beam lithography. We have excited and detected the magnetization dynamics in those antidot lattice structures by an all-optical time-resolved Kerr microscope. The dynamics shows two prominent magnonic bands for sparsely packed lattices with a clear bandgap. The bandgap increases with the decrease in the lattice constant and at the lowest value of the lattice constant four distinct magnonic bands appear. The observations are qualitatively reproduced by micromagnetic simulations and the mode profiles of the resonant modes are calculated and interpreted. We further demonstrate the tunability of magnonic spectra in composite antidot structures with varying geometry. The observations are important for potential applications of the antidot lattices in nanoscale magnonic crystals in the form of composite antidot structures with tunable bandgap.

Bibliography

[1] K. Kern, D. Heitmann, P. Grambow, Y. Zhang and K. Ploog, *Phys. Rev. Lett.* **66**, 1618 (1991).

[2] M. Diwekar, V. Kamaev, J. Shi and Z. V. Vardeny, *Appl. Phys. Lett.* **84**, 3112 (2004).

[3] G. Ctistis, E. Papaioannou, P. Patoka, J. Gutek, P. Fumagalli and M. Giersig, *Nano Lett.* **9**, 1 (2009).

[4] L. Torres, L. Lopez-Diaz and O. Alejos, *J. Appl. Phys.* **87**, 5645 (2000).

[5] C. C. Wang, A. O. Adeyeye and N. Singh, *Nanotech.* **17**, 1629 (2006).

[6] S. Neusser and D. Grundler, *Adv. Mater.* **21**, 2927 (2009).

[7] V. V. Kruglyak, S. O. Demokritov and D. Grundler, *J. Phys. D: Appl. Phys.* **43**, 264001 (2010).

[8] A. V. Chumak, V. S. Tiberkevich, A. D. Karenowska, A. A. Serga, J. F. Gregg, A. N. Slavin and B. Hillebrands, *Nat. Commun.* **1**, 141 (2010).

[9] F. S. Ma, H. S. Lim, Z. K. Wang, S. N. Piramanayagam, S. C. Ng and M. H. Kuok, *Appl. Phys. Lett.* **98**, 153107 (2011).

[10] G. Duerr, M. Madami, S. Neusser, S. Tacchi, G. Gubbiotti, G. Carlotti and D. Grundler, *Appl. Phys. Lett.* **99**, 202502 (2011).

[11] M. Yu, L. Malkinski, L. Spinu, W. Zhou and S. Whittenburg, *J. Appl. Phys.* **101**, 09F501 (2007).

[12] C. T. Yu, H. Jiang, L. Shen, P. J. Flanders and G. J. Mankey, *J. Appl. Phys.* **87**, 6322 (2000).

[13] A. Y. Toporov, R. M. Langford and A. K. Petford-Long, *Appl. Phys. Lett.* **77**, 3063 (2000).

[14] S. Tacchi, M. Madami, G. Gubbiotti, G. Carlotti, A. O. Adeyeye, S. Neusser, B. Botters and D. Grundler, *IEEE Trans. Magn.* **46**, 172 (2010).

[15] S. Tacchi, M. Madami, G. Gubbiotti, G. Carlotti, A. O. Adeyeye, S. Neusser, B. Botters and D. Grundler, *IEEE Trans. Magn.* **46**, 1440 (2010).

[16] S. Neusser, G. Duerr, S. Tacchi, M. Madami, M. Sokolovskyy, G. Gubbiotti, M. Krawczyk and D. Grundler, *Phys. Rev. B* **84**, 094454 (2011).

[17] S. Neusser, G. Duerr, H. Bauer, S. Tacchi, M. Madami, G. Woltersdorf, G. Gubbiotti, C. Back and D. Grundler, *Phys. Rev. Lett.* **105**, 067208 (2010).

[18] S. Neusser, B. Botters, M. Becherer, D. Schmitt-Landsiedel and D. Grundler, *Appl. Phys. Lett.* **93**, 122501 (2008).

[19] S. McPhail, C. Gürtler, J. Shilton, N. Curson and J. Bland, *Phys. Rev. B* **72**, 094414 (2005).

[20] O. Martyanov, V. Yudanov, R. Lee, S. Nepijko, H. Elmers, R. Hertel, C. Schneider and G. Schönhense, *Phys. Rev. B* **75**, 174429 (2007).

[21] M. Kostylev, G. Gubbiotti, G. Carlotti, G. Socino, S. Tacchi, C. Wang, N. Singh, A. O. Adeyeye and R. L. Stamps, *J. Appl. Phys.* **103**, 07C507 (2008).

[22] C. A. Grimes, P. L. Trouilloud, J. K. Lumpp and G. C. Bush, *J. Appl. Phys.* **81**, 4720 (1997).

[23] J. Ding, D. Tripathy and A. O. Adeyeye, *J. Appl. Phys.* **109**, 07D304 (2011).

[24] H. Ulrichs, B. Lenk and M. Münzenberg, *Appl. Phys. Lett.* **97**, 092506 (2010).

[25] S. Neusser, B. Botters and D. Grundler, *Phys. Rev. B* **78**, 054406 (2008).

[26] A. Barman, *J. Phys. D: Appl. Phys.* **43**, 195002 (2010).

[27] B. Rana, D. Kumar, S. Barman, S. Pal, Y. Fukuma, Y. Otani and A. Barman, *ACS Nano* **5**, 9559 (2011).

[28] M. Donahue and D. G. Porter, "OOMMF User's guide, Version 1.0," *NIST Interagency Report Number 6376, National Institute of Standard and Technology, Gaithersburg, MD, URL:* http://math.nist.gov/oommf, City (1999).

[29] D. Kumar, O. Dmytriiev, S. Ponraj and A. Barman, *J. Phys. D: Appl. Phys.* **45**, 015001 (2012).

Chapter 8

Effect of Antidot Shape on the Spin Wave Spectra of Two-dimensional $Ni_{80}Fe_{20}$ Antidot Lattices

8.1 Introduction

Ferromagnetic antidot lattices have emerged as a strong candidate for magneto-photonic crystals[1, 2] and ultra-high density magnetic data storage media[3]. More recently, they have been studied intensively as a promising candidate for magnonic devices. Waveguides[4], filters[5], interferometers[6], phase shifters[7], spin wave logic[8] and magnonic crystals[9, 10] are some important components of magnonic devices and investigation of spin wave dispersion in such devices with their structural and material parameters are at the forefront of research in magnonics. For antidot lattices with large periods in μm and sub-μm range, inhomogeneous internal magnetic fields play important role in determining the frequencies and spatial characters of the spin waves, while for reduced period down to few tens of nm the exchange field starts to play important role. Consequently, a large number of parameters of antidot lattices can be varied to tune the spin waves in them. These include the size and shape of the antidots, the spacing between the antidots (lattice constant), base material, and the strength and orientations of the bias magnetic field. In the last chapter we already investigated the effects of lattice constant on spin wave spectra on two-dimensional antidot lattices.

In this chapter, we investigate the spin wave spectra in a two-dimensional antidot lattice with varying antidot shapes namely square, circular, triangular and diamond shapes. When the bias field is applied parallel to one of the edges of the lattices, a remarkable difference in the spin wave spectra is observed in the lattices with triangular and diamond shaped antidots as opposed to the circular and square shaped antidots. In addition, a strong anisotropy in spin wave spectra is observed as the bias field is rotated by 45° *with respect to* the edges of the lattice. We understood this significant variation as a result of the variation in the internal field profiles

surrounding the antidots and the resulting spin wave mode profiles with the aid of the micromagnetic simulations.

Initial studies on the dynamics of ferromagnetic antidot lattices showed pattern induced splitting of surface and volume modes[11], localization, confinement, and field-controlled propagation of spin waves[12, 13], and observation of dispersive and entangled spin waves between the antidots[14]. Later, anisotropic propagation velocity and damping of spin waves were observed in a square lattice of circular antidots, which was explained by magnetic field-controlled spin wave guiding in a network of interconnected nanowires[15]. Ulrichs *et al.* studied spin waves in CoFeB antidot lattices[16], where they observed a field independent localized mode. Significant effects of lattice symmetry[17]and diameters of the antidots on spin waves[18] were observed on one hand and on the other hand formantion of magnonic minibands,[19] and tunable metamaterial response in $Ni_{80}Fe_{20}$ antidot lattices[20] attracted great interests. Later, a number of works reported complete magnonic bandgaps[21], linear bias field dependence of high-symmetric magnonic modes for perpendicularly magnetized antidot lattices[22], transformation of quantized spin wave modes to propagating ones and vice- versa by changing the in-plane orientation of the applied magnetic field[23], and tunable frequency gap in spin wave spectra with varying lattice constants in two-dimensional Co antidot lattices[24]. Micromagnetic simulations have been performed to study the effect of varying shapes of the antidot on the magnonic bandgap in a one-dimensional magnonic antidot waveguide at a length scale dominated by exchange interaction[25]. However, the effect of the shapes of the antidot on the demagnetizing field profiles inside an antidot lattice and the corresponding spin wave spectra have not been extensively studied. The spin wave dispersion for a square lattice with varying shape of the basis (antidot) structure, particularly when calculated along Γ-M and X-M symmetry axes, may show anisotropy arising from symmetry considerations. However, here we measure the zero wave vector modes and some localized and standing wave modes. Hence, the demagnetizing field profiles surrounding different shapes of the antidots play the major role.

8.2 Sample Fabrication and Measurement Technique

8.2.1 Fabrication

Square, circular, triangular and diamond shaped antidots with about 200 nm width and height and having separation between the nearest edges of about 230 nm were fabricated on square lattices, each covering 10 × 10 μm^2 area on a 20 nm thick $Ni_{80}Fe_{20}$ film coated with a 5 nm SiO_2 protective layer. The circular antidots were fabricated by focused ion beam milling using liquid Ga^+ ion beam at 30 kV voltage and 28 pA beam current, which produced a spot size of about 8 nm. Since square and triangular shapes have sharp corners we used lower spot size (~4 nm) by reducing the beam current to 10 pA. The presence of 5 nm thick SiO_2 capping layer protects the un-milled $Ni_{80}Fe_{20}$ film to a large extent from direct irradiation, while damages at the edges of the antidots due to Ga^+ ion implantation occurring laterally is limited to only about 5 nm from the edges. Further details of the focused ion beam milling can be found elsewhere[24]. The scanning electron micrographs (Figure. 8.1) show that the square, triangular and diamond shaped antidots have rounded corners due to the finite size of the ion beam. The triangular and diamond shaped antidots also suffer from small asymmetry in their shapes. The antidot size and edge-to-edge separation show upto ±5% deviation. All the above deviations will be introduced in the numerical simulations except for the edge roughness, possible edge pinning and variation of material quality at the antidot edges because of Ga^+ ion implantation due to the difficulty in their characterization.

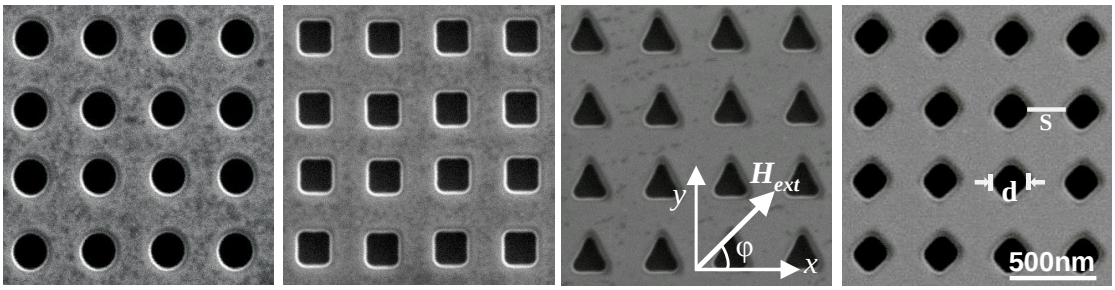

Figure 8.1: Scanning electron micrographs of four different antidot lattices with varying shapes.

8.2.2 Measurement

The time-resolved magnetization dynamics was measured by an all-optical time-resolved magneto-optical Kerr effect microscope[24]. The dynamics was excited by the second-harmonic (λ = 400 nm, pulse width = 100 fs, fluence = 16 mJ/cm^2) of a Ti-sapphire oscillator (Tsunami, Spectra-Physics), while the time-delayed fundamental (800 nm, 70 fs, 3 mJ/cm^2) is used to probe the dynamics by measuring the Kerr rotation as a function of the time-delay between the pump and the probe beams. The external bias magnetic field is tilted at a small angle (~15°) from the plane of the sample, the in-plane component of which is denoted by H_{ext} in Figure. 8.1.

8.3 Micromagnetic Simulation

The experimental results are reproduced by using micromagnetic simulations using OOMMF software[26]. We have studied arrays of 7 × 7 antidots with varying shapes and discretized the arrays into rectangular prisms with dimensions 3×3×20 nm^3. The shapes of the antidots are derived from the SEM images and material parameters used in the simulations are gyromagnetic ratio, γ =17.5 MHz/Oe, magnetocrystalline anisotropy, H_k = 0, saturation magnetization, M_s = 800 emu/cc and exchange stiffness constant, A = 1.3×10^{-6} erg/cm. The simulation methods are described in detail elsewhere[24]. The bias field is applied according to experimental configurations and a pulsed field of peak value of 20 Oe and 10 ps rise time is used perpendicular to the sample plane, while a damping coefficient α = 0.015 is used during dynamic simulations.

In Figure. 8.2, we show the contour plot of simulated magnetostatic field distributions for all four lattices, which show the non-uniform magnetic field distributions (demagnetized regions) around the edges of the antidots. The profiles of these demagnetized regions are key to determining the extended and quantized spin wave modes. While the symmetry of the demagnetized regions is similar for the circular and square antidots, it changes significantly for the triangular and diamond shaped antidots. In addition to the nominal variation in the shape, introduction of asymmetry of shape due to fabrication defect poses further differences in the internal field profile.

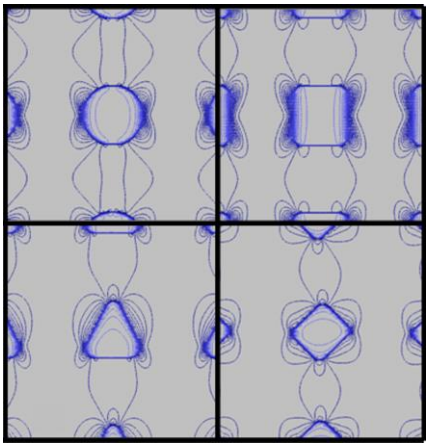

Figure 8.2: Simulated magnetostatic fields for four different antidot lattices with varying shapes.

8.4 Time-Resolved Precessional Dynamics of Array of $Ni_{80}Fe_{20}$ Antidot Lattices with Different Antidot Shapes

Figure 8.3 shows the time-resolved Kerr rotations for the four samples at H_{ext} = 900 Oe revealing three important temporal regimes, namely the ultrafast demagnetization (500 fs), fast relaxation (5.4 ps) and the precessional motion superposed on a slow relaxation (334 ps).

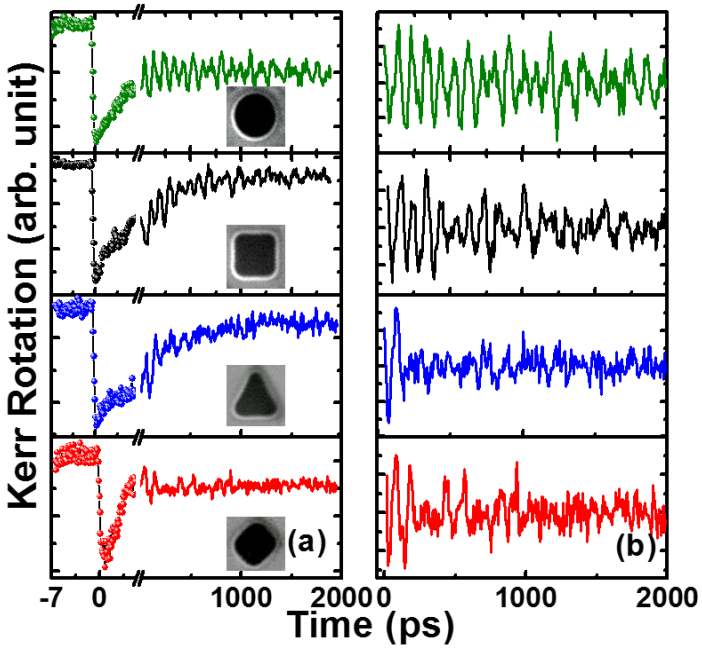

Figure 8.3: (a) Time-resolved Kerr rotation from different antidot lattices showing three different temporal regimes, namely ultrafast demagnetization, fast relaxation and spin precession superposed on a slow relaxation and (b) the precessional part of the time-resolved Kerr rotation after a bi-exponential background subtraction.

In Figure 8.3(a) we show the precessional part of the time-resolved magnetization dynamics after subtracting a bi-exponential background. The spin wave spectra are obtained by taking fast Fourier transform (FFT) of the background subtracted time-resolved Kerr rotation as shown in Figure.8.4 for all four samples at three bias field orientations φ = 0°, 45° and 90°. The spectra for φ = 0° and 90° are qualitatively similar but there are some quantitative differences due to the fabrication induced structural asymmetry in the antidots of each shape to varying extent.

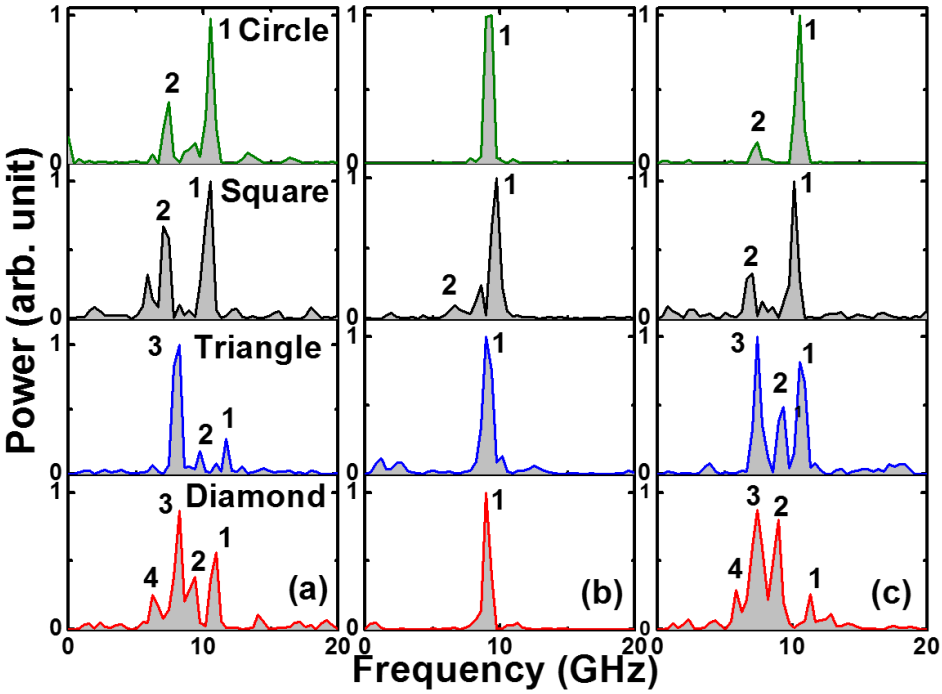

Figure 8.4: Spin wave spectra obtained from experimental time-resolved Kerr rotation data from four different antidot lattices for three different bias field orientations (a) φ = 0°, (b) φ = 45° and (c) φ = 90°.

Figure 8.4(a) reveals that the circular and square shaped antidot lattices show two dominant bands of frequencies with a gap of about 3.17 and 3.34 GHz, respectively. For the square antidot lattice another low amplitude shoulder is observed at about 5.9 GHz. In the triangular antidot lattice another mode appears in the gap between the two bands, reducing the gap to about 1.7 GHz each between the three bands. For the diamond antidot lattice four closely spaced modes occur with narrow gaps of about 1.35, 1.25 and 1.85 GHz. We have simulated the spin wave spectra by micromagnetic simulations as shown in Figure. 8.5.

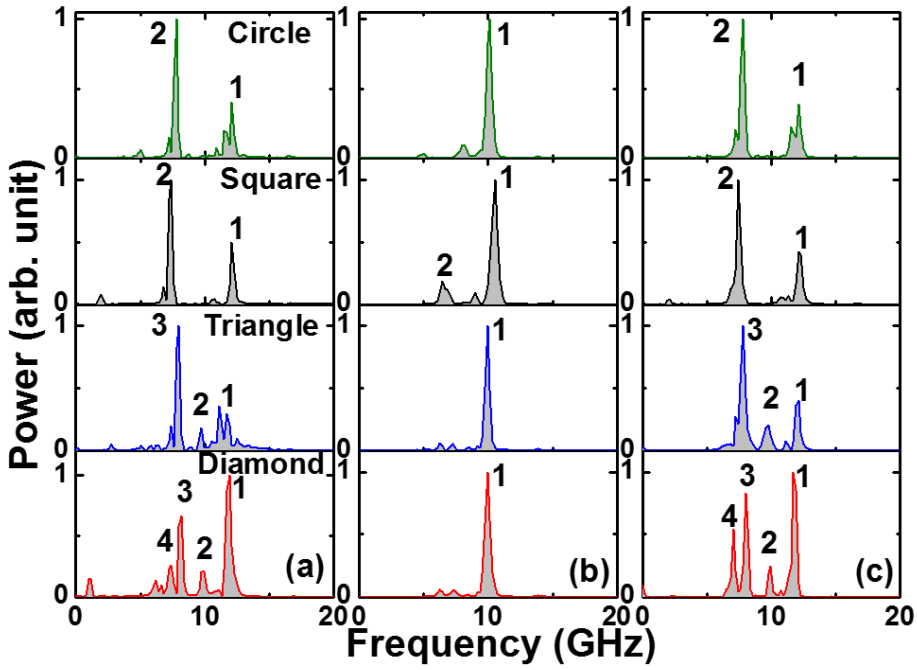

Figure 8.5: Simulated spin wave spectra from four different antidot lattices for three different bias field orientations (a) φ = 0°, (b) φ = 45° and (c) φ = 90°.

The simulation reproduced the important features in the spin wave spectra qualitatively. It shows two bands of modes for the circular and square shaped antidot lattices with frequency gaps of 3.9 and 4.5 GHz, respectively. The triangular antidots lattice shows three modes with two frequency gaps of about 2.1 GHz each, between the three modes. On the other hand the diamond shaped lattice shows four closely spaced modes with frequency gaps of 1.8, 1.8 and 1.2 GHz. The remarkable difference in the spin wave spectra between different antidot shapes stems from their internal field profiles, which lead to various extended and localized modes as shown later in this article. At φ = 45° a strong anisotropy in the spin wave spectra is observed for all lattices, where a dominant mode is observed just below 10 GHz irrespective of the antidot shape. For circular antidots a dominant mode with frequency about 9.3 GHz is observed, which is intermediate between the two bands of modes observed for φ = 0° and 90°. However, for the square lattice, in addition to a dominant mode at around 9.8 GHz, a small amplitude mode at 6.6 GHz is also observed. In cases of triangular and diamond shaped antidot lattice again a single mode with frequencies of 9.1 and 9.0 GHz is observed. Again, micromagnetic simulations qualitatively reproduced the experimental spin wave modes. Dominant single mode for circular,

triangular and diamond shaped antidot lattices and an additional small amplitude mode at lower frequency for the square shaped antidot are observed in the simulated spectra. The simulated peak frequencies are slightly (5-10%) higher than the experimental frequencies.

8.5 Power and Phase Profiles of Resonant Modes

We have further simulated the profiles of the resonant modes[27] and the simulated power maps are shown in Figure. 8.6. At φ = 0°, mode 1 in the circular antidot lattice shows a quantized mode (mode number q = 5) due to the formation of standing wave in the backward volume magnetostatic (BWVMS) wave geometry between two neighboring antidots. Mode 2 is an extended mode flowing through the channel between the neighboring antidots in the Damon-Eshbach (DE) geometry. In the square lattice mode 1 is again a quantized mode, while mode 2 identical to mode 2 of circular antidot lattice. In the triangular antidot lattice mode 1 is also a quantized mode with q = 5 but in this case the standing wave does not form exactly between the two antidots but shifts down vertically and becomes asymmetric due to the asymmetry in the internal field profile. Mode 2 is a quantized mode with q = 3 along the bias field direction but it extends in the direction perpendicular to the bias field forming a serpentile shape through the channel between the neighboring antidots. This shape of mode also stems from the internal field profile. Unlike the other shapes of antidots, in this case, when the field is rotated by 90° mode profiles for all three modes change significantly giving rise to further differences in the frequency spectra. In the diamond shaped antidot lattice, the first three modes are identical to those of the triangular antidots with small changes in shape due to the different internal field profile. However, in this case a fourth mode appears, which is a DE-like mode that got modified by the corners of the diamond shape. The absence of the q = 3 mode in the circular and square antidot lattice causes larger gap in their frequency spectra, while appearance of the same reduces that gap in the triangular and diamond antidot lattices.

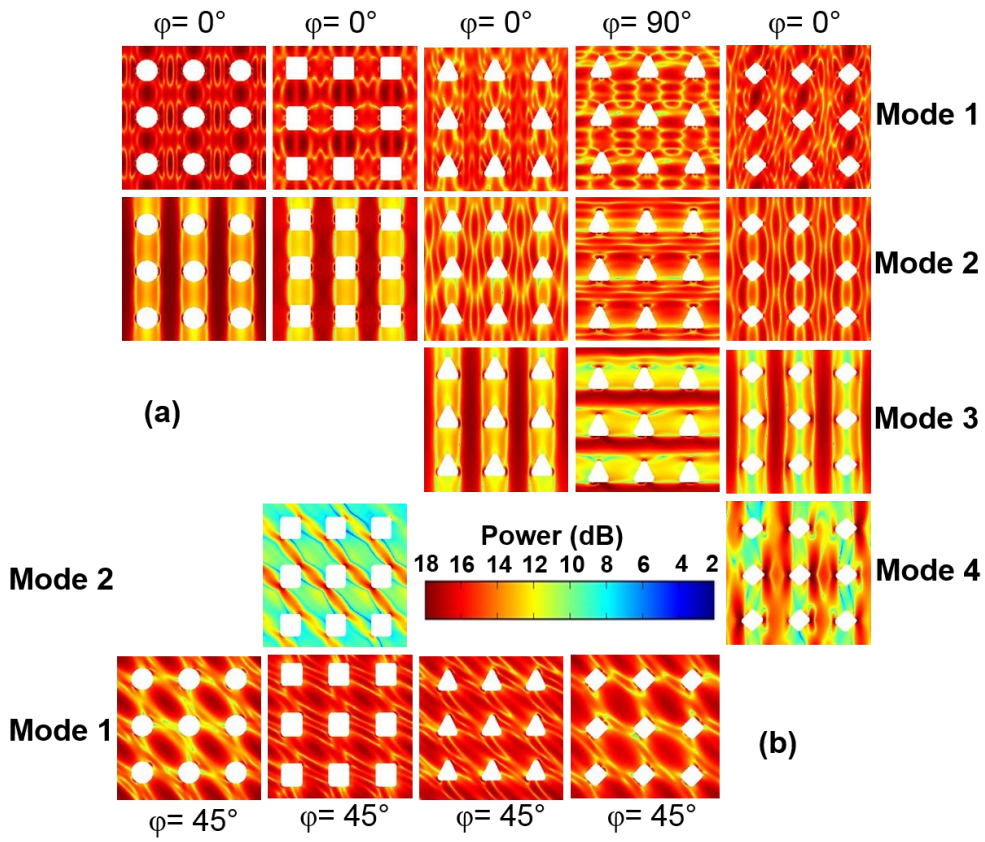

Figure 8.6: Spin wave mode profiles (power) for antidot lattices with varying shapes with the bias field orientation of (a) φ = 0° or 90° and (b) φ = 45°. The colormap used for the mode profiles is shown inside the figure.

At φ = 45°, mode 1 is identical for all antidot shapes, which is the localized (trapped) mode between the next nearest antidots perpendicular to the field direction. However, there is a small difference between different antidot shapes of the localized mode profile, which changes due to the variation in the internal field profile. For the square antidot a weak extended second mode (mode 2) in the DE geometry is accommodated in the narrow channel between the antidots, while this mode does not appear with significant amplitude in other antidot lattices, where the demagnetizing fields surrounding the neighboring antidots start to overlap at this value of φ, blocking the path of the extended spin wave mode.

8.6 Summary

In summary, we have investigated the effects of the shape of the antidots on the spin waves in $Ni_{80}Fe_{20}$ antidot lattices. Significant differences in the spin wave spectra are

observed with the variation in the antidot shape. Two prominent modes with significant gaps in the spin wave spectra for the circular and square shaped antidots change into three and four closely spaced modes with narrow gaps for the triangular and diamond shaped antidot lattices, respectively. In addition, when the bias field is rotated within the sample plane by $\varphi = 45°$ from the horizontal or vertical edges of the lattices a single dominant mode is observed for three lattices except for the square shaped antidot lattice, where an additional low amplitude mode occurs at lower frequency. Micromagetic simulations helped to identify the spin wave modes. While for the circular and square antidot lattices the higher frequency mode is a quantized mode in the BWVMS geometry with mode number $q = 5$, the lower frequency mode is an extended DE mode. In the triangular and diamond shaped lattices an additional quantized mode with $q = 3$ appeared in the frequency gap observed in the other two lattices. For the diamond shaped lattice another modified DE-like mode appears at frequency below the DE mode. At $\varphi = 45°$ the extended DE mode disappears for the circular, triangular and diamond shaped antidot lattices and its power is reduced significantly in the square antidot lattice, while a mode localized in the region between the next nearest antidots in a direction perpendicular to the bias field becomes dominant. The observed tunability of the spin wave spectrum with the antidot shape and the bias field orientation may give rise to an enabling tool for tuning the frequency of such devices when they are used as magnonic filters, splitters and other magnonic devices.

Bibliography

[1] K. Kern, D. Heitmann, P. Grambow, Y. H. Zhang and K. Ploog, *Phys. Rev. Lett.* **66**, 1618 (1991).

[2] G. Ctistis, E. Papaioannou, P. Patoka, J. Gutek, P. Fumagalli and M. Giersig, *Nano Lett.* **9**, 1 (2009).

[3] L. Torres, L. Lopez-Diaz and O. Alejos, *J. Appl. Phys.* **87**, 5645 (2000).

[4] J. W. Kłos, D. Kumar, M. Krawczyk and A. Barman, *Sci. Rep.* **3**, 2444 (2013).

[5] S.-K. Kim, K.-S. Lee and D.-S. Han, *Appl. Phys. Lett.* **95**, 082507 (2009).

[6] J. Podbielski, F. Giesen and D. Grundler, *Phys. Rev. Lett.* **96**, 167207 (2006).

[7] Y. Au, M. Dvornik, O. Dmytriiev and V. V. Kruglyak, *Appl. Phys. Lett.* **100**, 172408 (2012).

[8] T. Schneider, A. A. Serga, B. Leven, B. Hillebrands, R. L. Stamps and M. P. Kostylev, *Appl. Phys. Lett.* **92**, 022505 (2008).

[9] V. V. Kruglyak, S. O. Demokritov and D. Grundler, *J. Phys. D: Appl. Phys.* **43**, 264001 (2010).

[10] B. Lenk, H. Ulrichs, F. Garbs and M. Münzenberg, *Phys. Rep.* **507**, 107 (2011).

[11] S. McPhail, C. Gürtler, J. Shilton, N. Curson and J. Bland, *Phys. Rev. B* **72**, 094414 (2005).

[12] S. Neusser, B. Botters, M. Becherer, D. Schmitt-Landsiedel and D. Grundler, *Appl. Phys. Lett.* **93**, 122501 (2008).

[13] S. Neusser, B. Botters and D. Grundler, *Phys. Rev. B* **78**, 054406 (2008).

[14] M. Kostylev, G. Gubbiotti, G. Carlotti, G. Socino, S. Tacchi, C. Wang, N. Singh, A. O. Adeyeye and R. L. Stamps, *J. Appl. Phys.* **103**, 07C507 (2008).

[15] S. Neusser, G. Duerr, H. Bauer, S. Tacchi, M. Madami, G. Woltersdorf, G. Gubbiotti, C. Back and D. Grundler, *Phys. Rev. Lett.* **105**, 067208 (2010).

[16] H. Ulrichs, B. Lenk and M. Münzenberg, *Appl. Phys. Lett.* **97**, 092506 (2010).

[17] S. Tacchi, M. Madami, G. Gubbiotti, G. Carlotti, A. O. Adeyeye, S. Neusser, B. Botters and D. Grundler, *IEEE Trans. Magn.* **46**, 1440 (2010).

[18] J. Ding, D. Tripathy and A. O. Adeyeye, *J. Appl. Phys.* **109**, 07D304 (2011).

[19] S. Neusser, G. Duerr, S. Tacchi, M. Madami, M. Sokolovskyy, G. Gubbiotti, M. Krawczyk and D. Grundler, *Phys. Rev. B* **84**, 094454 (2011).

[20] S. Neusser, H. G. Bauer, G. Duerr, R. Huber, S. Mamica, G. Woltersdorf, M. Krawczyk, C. H. Back and D. Grundler, *Phys. Rev. B* **84**, 184411 (2011).

[21] R. Zivieri, S. Tacchi, F. Montoncello, L. Giovannini, F. Nizzoli, M. Madami, G. Gubbiotti, G. Carlotti, S. Neusser, G. Duerr and D. Grundler, *Phys. Rev. B* **85**, 012403 (2012).

[22] R. Bali, M. Kostylev, D. Tripathy, A. O. Adeyeye and S. Samarin, *Phys. Rev. B* **85**, 104414 (2012).

[23] S. Tacchi, B. Botters, M. Madami, J. W. Klos, M. Sokolovskyy, M. Krawczyk, G. Gubbiotti, G. Carlotti, A. O. Adeyeye, S. Neusser and D. Grundler, *Phys. Rev. B* **86**, 014417 (2012).

[24] R. Mandal, S. Saha, D. Kumar, S. Barman, S. Pal, K. Das, A. K. Raychaudhuri, Y. Fukuma, Y. Otani and A. Barman, *ACS Nano* **6**, 3397 (2012).

[25] D. Kumar, P. Sabareesan, W. Wang, H. Fangohr and A. Barman, *J. Appl. Phys.* **114**, 023910 (2013).

[26] M. Donahue and D. G. Porter, "OOMMF User's guide, Version 1.0," *NIST Interagency Report Number 6376, National Institute of Standard and Technology, Gaithersburg, MD, URL:* http://math.nist.gov/oommf, City (1999).

[27] D. Kumar, O. Dmytriiev, S. Ponraj and A. Barman, *J. Phys. D: Appl. Phys.* **45**, 015001 (2012).

Chapter 9

Tunable Spin Wave Spectra in Two-dimensional $Ni_{80}Fe_{20}$ Antidot Lattices with Varying Lattice Symmetry

9.1. Introduction

Ferromagnetic antidot lattices have emerged as a strong candidate for magneto-photonic crystals[1, 2] and ultra-high density magnetic data storage media[3]. The latter has been prompted due to the absence of any isolated small magnetic entity and the consequent avoidance of superparamagnetic bottleneck in such lattices. More recently, ferromagnetic antidot lattices have been studied intensively as a promising candidate for magnonic devices. Waveguides[4, 5], filters[6, 7], interferometers[8, 9], phase shifters[10], spin wave logic[11] and magnonic crystals[12-15] are some important components of magnonic devices and investigation of spin wave dispersion in such devices with their structural and material parameters are at the forefront of research in magnonics. In the antidot lattices spin waves propagate through the continuous ferromagnetic medium between the antidots and have much higher propagation velocity and longer propagation distance as opposed to other forms of magnonic crystals such as lattices formed of dots and stripes. Ferromagnetic antidots with dimensions ranging from few micrometers to 100 nm have been fabricated by various nanofabrication techniques and are studied in great details in last few years[16-34]. For antidot lattices with large periods in μm and sub-μm range, inhomogeneous internal magnetic fields play important roles in determining the frequencies and spatial characters of the spin waves, while for reduced period down to few tens of nm the exchange field starts to play important role. Consequently, a large number of parameters of antidot lattices can be varied to tune the spin waves in them. These include the size and shape of the antidots, the spacing between the antidots (lattice constant), base material, and the strength and orientations of the bias magnetic field. A number of studies have been reported in the literature where almost all the above parameters have been varied to investigate their effects on the spin wave spectra.

Initial studies on the dynamics of ferromagnetic antidot lattices using Brillouin light scattering (BLS) and ferromagnetic resonance (FMR) experiments showed pattern induced splitting of surface and volume modes[16], a strong attenuation of the uniform ferromagnetic resonance mode in comparison to a continuous film but excitation of non-uniform in-plane spin wave mode due to the non-uniform demagnetization field around the antidots[17], localization, confinement, and field-controlled propagation of spin waves[18, 19] and observation of dispersive and entangled spin waves between the antidots[20]. Later, using a combination of BLS and FMR a number of magnetic normal modes were observed as a function of the bias field strength and orientation[22]. In the same year anisotropic propagation velocity and damping of spin waves were observed in a square lattice of circular antidots, which was explained by magnetic field-controlled spin wave guiding in a network of interconnected nanowires[21]. Ulrichs *et al.* studied spin waves in CoFeB antidot lattices, where they observed a field independent localized mode[24]. Significant effects of diameters of the antidots on spin waves[25] were observed at one hand and on the other hand formantion of magnonic minibands[17], spatial contrtol of spin waves in a bi-component magnonic crystals[26] and tunable metamaterial response in $Ni_{80}Fe_{20}$ antidot lattices[27] attracted great interests. Later, a number of works reported complete magnonic bandgaps[32, 33] linear bias field dependence of high-symmetric magnonic modes for perpendicularly magnetized antidot lattices[29], rich mode spectra in binary antidot lattices[34], transformation of quantized spin wave modes to propagating ones and vice- versa by changing the in-plane orientation of the applied magnetic field[31], and tunable spin wave spectra with varying lattice constants[30] and antidot shapes[35] in two-dimensional ferromagnetic antidot lattices. Micromagnetic simulations have also been performed to study the effect of varying shapes on the antidot on the magnonic bandgap in a one-dimensional magnonic antidot waveguide in a length scale dominated by exchange interaction[36]. However, there are not many reports[23, 37]in the literature to investigate the effects of lattice symmetry on the spin wave properties of two dimensional antidot lattices.

Here, we fill that gap in research and present the investigation of spin wave spectra in a two-dimensional circular antidot lattice with varying lattice symmetry, namely square, rectangular, hexagonal, honeycomb and octagonal symmetry. Using broadband ferromagnetic resonance we show a remarkable difference in the spin wave spectra with the variation of lattice symmetry. With the reduction of lattice

symmetry the number of modes and the mode intensities varied significantly. With the aid of micromagnetic simulations, we unravel the spin wave mode profiles, which show various extended, standing wave and localized spin wave modes. The reduction of lattice symmetry resulted in the disappearance of the extended modes and localization of the modes. For the non-Bravais lattices the localized modes are distributed in a non-uniform pattern throughout the lattice. We understood this significant variation as a result of the variation in the internal field profiles surrounding the antidots, which varied with lattice symmetry.

9.2. Sample Fabrication and Measurement Technique

9.2.1 Fabrication

25 μm × 250 μm arrays of $Ni_{80}Fe_{20}$ circular antidots arranged in different lattice symmetries were fabricated by a combination of electron beam lithography, electron beam evaporation and ion milling. The width of each antidot is about 300 nm (±5%) and the separation between the nearest edges of about 330 nm (±5%). The 20 nm thick $Ni_{80}Fe_{20}$ film coated with a 60 nm Al_2O_3 protective layer was deposited in an ultra-high vacuum chamber at a base pressure of 2×10^{-8} Torr on a commercially available self-oxidized Si [100] substrate. Bi-layer (PMMA/MMA) resist was used for e-beam lithography to make the resist pattern on the $Ni_{80}Fe_{20}$ thin film followed by ion milling at a base pressure of 1×10^{-4} Torr with a beam current of 60 mA for 6 minutes for creating the antidots.

A co-planar waveguide made of Au with thickness of 150 nm was deposited on top of the antidot structures at a base pressure of 6×10^{-7} Torr for the broadband ferromagnetic resonance measurement. The Au waveguide (Figure. 9.1) has central conductor of 30 μm width, total length of 300 μm and a nominal characteristic impedance of 50 Ω. The Au waveguide was patterned by using mask-less photolithography. This is followed by deposition of a protective layer of Ti (5 nm) on top of the Au layer at the same base pressure. Both the Bravais (square, rectangular, hexagonal) and non-Bravais (honeycomb, octagonal) lattices are fabricated to investigate the effect of variation in lattice symmetry on the spin wave spectra.

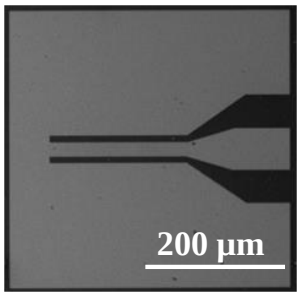

Figure 9.1: Scanning electron micrograph of a co-planar waveguide structure.

9.2.2 Measurement

The spin wave spectra from the arrays were measured by a broadband ferromagnetic resonance (FMR) spectrometer[38] using a vector network analyzer (Agilent PNA-L N5230C, 10 MHz to 50 GHz) and a home-built high frequency probe station with nonmagnetic G-S-G type probes (GGB Industries, Model Number 40A-GSG-150-EDP). Figure 9.2 shows a schematic of the broadband FMR setup. An inbuilt electromagnet inside the probe station with bias field upto 2.0 kOe is used to apply an external bias field (H_{ext}) parallel to the co-planar waveguide (CPW). RF signals with varying frequencies are launched into the CPW structure using a G-S-G type probe. The CPW is shorted at one end and the back reflected signal is collected by the same probe to the analyzer. Absorption of the ongoing and returning signals at various spin wave frequencies produces the characteristic spin wave spectrum of the sample. The real and imaginary parts of the scattering parameter in the reflection geometry (S_{11}) at various bias fields are subtracted from its value at the maximum bias field (reference spectrum) and the spin wave spectra are obtained.

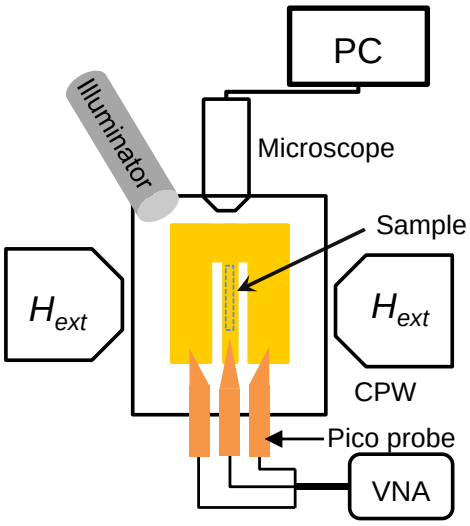

Figure 9.2: A Schematic diagram of the broadband ferromagnetic resonance spectrometer.

9.3 Micromagnetic Simulation

The experimental results are reproduced by using micromagnetic simulations using OOMMF software[39] by considering finite lattices of about 4000 × 4000 × 20 nm^3volumes with nominal dimensions of the antidots and with varying lattice symmetry. The arrays of each lattices are discretized into rectangular prisms with dimensions 4 × 4 × 20 nm^3. The material parameters used in the simulations are gyromagnetic ratio, γ =17.6 MHz/Oe, magnetocrystalline anisotropy, H_k = 0, saturation magnetization, M_s = 860 emu/cc and exchange stiffness constant, A = 1.3×10^{-6} erg/cm. The simulation methods are described in detail elsewhere[30]. The bias field is applied according to experimental configurations and a pulsed field of peak value of 20 Oe and 10 ps rise time is used perpendicular to the sample plane, while a damping coefficient α = 0.008 is used during dynamic simulations.

9.4 Results and Discussion

Figure 9.3(a) shows scanning electron micrographs of different lattice structures. They are generally well fabricated with small deviation from the nominal shape and size. Figure 9.3(b) shows the real part of scattering parameter (S_{11}) as a function of the *r.f* frequency for a bias field value H_{ext} = 1 kOe applied at an angle ϕ= $0^0$to the samples with five different lattice symmetry. The dips in the spectra at higher frequencies are generally obtained due to the subtraction of the reference spectrum, which sometimes obscures the low intensity modes occurring at higher frequencies. However, this is unavoidable due to the limit in the maximum bias magnetic field as well as occurrence of broad band of modes in these systems. Distinct differences between the spectra are observed with the variation of lattice symmetry. The square lattice shows three clear modes all with significant intensity. The gap between modes 3 and 2 (1.5 GHz) is nearly twice of that between modes 2 and 1 (0.8 GHz). The spectrum for the rectangular lattice is qualitatively similar to that for a square lattice barring two clear differences; the gap between modes 3 and 2 (3.4 GHz) is much higher than that for the square lattice and the intensity of mode 3 is relatively low. The hexagonal lattice showed a stark difference in the spectrum. Here the two lowest frequency modes (modes 1 and 2) are hardly resolved. Mode 3 is also very close to

mode 2 and of very low intensity and is appeared as a shoulder to mode 2. A very low intensity fourth mode is also observed in this case. The honeycomb lattice shows three very closely spaced modes with reasonably large intensities and a higher frequency fourth mode (gap = 2 GHz between modes 4 and 3) with low intensity. The spectrum for the octagonal lattice is very similar to that for the honeycomb lattice. Here, modes 1, 2 and 3 are very closely spaced with mode 3 appearing as a low intensity shoulder to mode 2. A low intensity mode 4 appears after a large gap from mode 3.

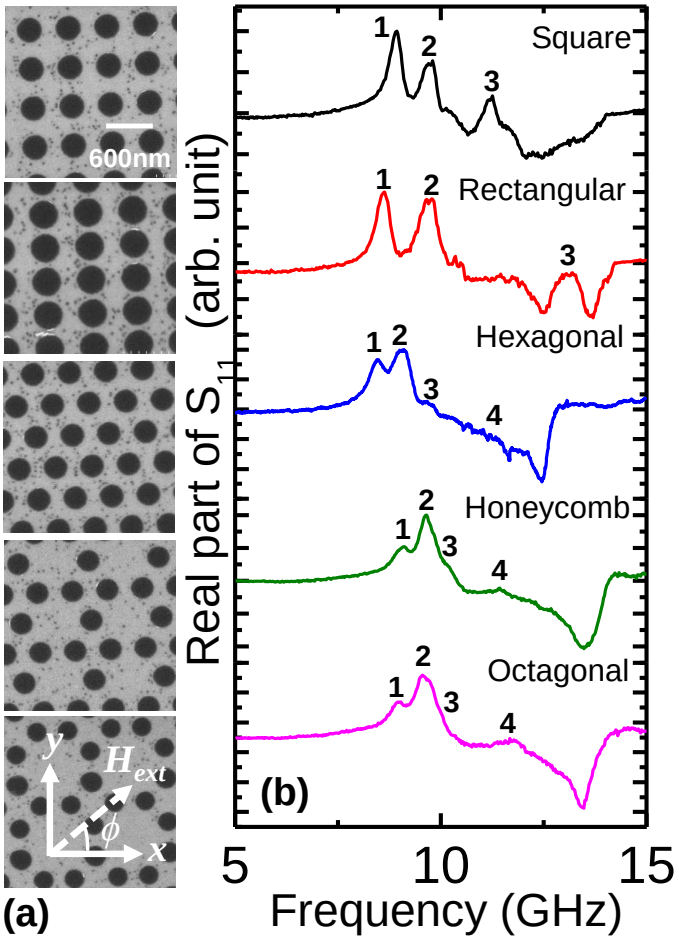

Figure 9.3: (a) Scanning electron micrographs of the antidots with varying lattice symmetry. (b) Real part of S_{11} parameter showing the FMR spectra for all five samples for H_{ext} = 1 kOe applied at ϕ = 0°.

In Figure 9.4 the bias field dependence of the real part of S_{11} is plotted for all five samples. The surface plots of 56 spectra for bias field range 400 Oe ≤ H_{ext} ≤ 1500 Oe at a spacing of 20 Oe are shown for each array. The bias field dependence of spin wave mode frequencies revealed some additional information. For the square lattice the gap between modes 1 and 2 remained constant over the whole field range while

mode 2 splits into two modes for $H_{ext} \leq 800$ Oe, and the magnitude of splitting increases with the reduction of H_{ext}. In contrary, the spacing between modes 4 and 2 increases with the reduction of bias field. The dependence of resonant mode frequency with bias field for the rectangular lattice is identical to the square lattice

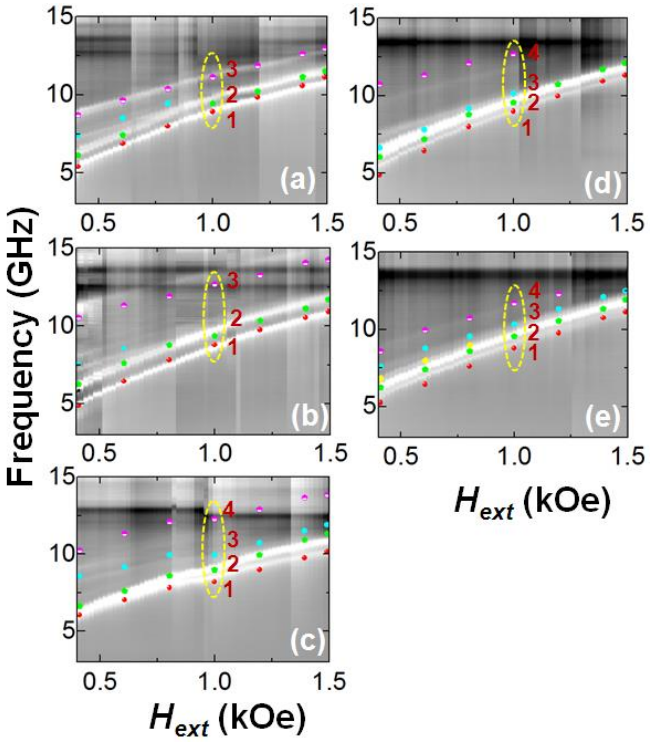

Figure 9.4: Bias field dependent ferromagnetic resonance frequencies for the (a) square, (b) rectangular, (c) hexagonal, (d) honeycomb and (e) octagonal lattice. The surface plots correspond to the experimental data while the symbols correspond to the simulated data.

including the splitting of mode 2 for $H_{ext} \leq 800$ Oe. However, in the hexagonal lattice modes 1 and 2 come closer with the reduction of field and merge into a single mode for $H_{ext} < 700$ Oe. On the other hand, mode 3 deviates from mode 2 with the reduction of bias field and at the lowest measurement field (400 Oe) the gap becomes maximum (2GHz). The frequency of mode 4 reduces monotonically with bias field and its separation with mode 2 remained constant within the measured field range. The bias field variation of mode frequencies in honeycomb lattice is qualitatively similar to the square and rectangular lattices with the exception that the splitting of mode 2 into two modes commenced at a higher field (~ 1 kOe). In the octagonal lattice frequencies of all four modes decrease monotonically with field with no significant change in the

separation between the modes with bias field. Here also a splitting of mode 3 occurs at about 1 kOe.

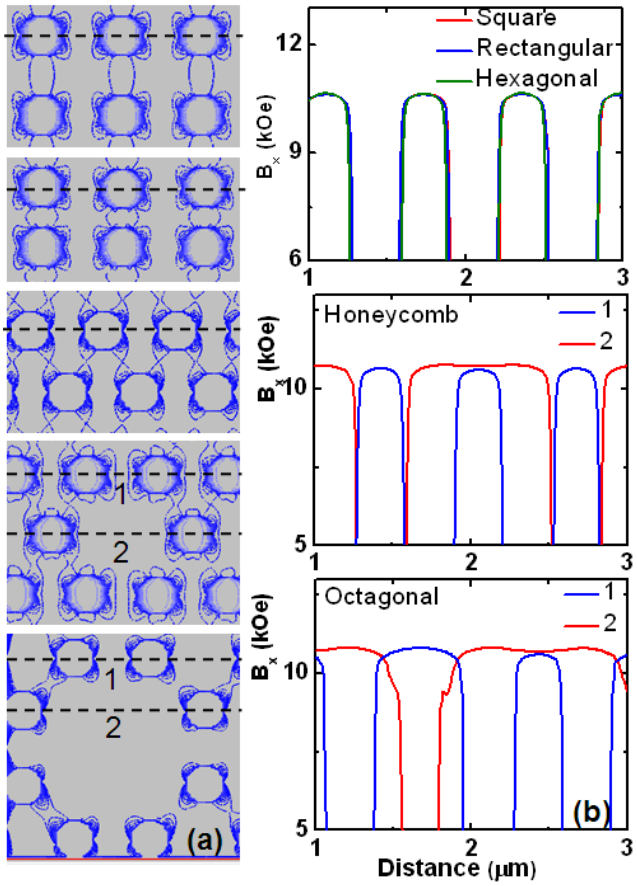

Figure 9.5: (a) Contour plot of the simulated magnetostatic field distribution in $Ni_{80}Fe_{20}$ antidot lattices with five different lattice symmetries. The line scans are taken along the dotted lines. (b) Line scans of the simulated magnetostatic fields.

Figure 9.5(a) shows the simulated contour plots of the internal magnetic field profiles for all five lattices. The non-uniform demagnetizing fields around the antidots have similar profiles for both square and rectangular lattice with the only difference that along y-direction the fields are tightly spaced for the rectangular lattice due to its smaller lattice constant along that direction. In both cases the channels between antidots arranged on consecutive columns are open to allow extended spin wave modes. However, in case of hexagonal lattice the demagnetizing fields of the next nearest antidots overlap, forbidding any extended regions along both x- and y-directions for the extension of spin waves. The non-Bravais lattices show even more complicated field profiles. The honeycomb and octagonal lattices allow two regions

for the formation of standing spin waves, one inside each honeycomb or octagonal unit and the other between two such consecutive units. Line scans of the simulated magnetic field along the dotted lines are shown in Figure. 9.5(b). While the internal fields in the materials between the antidots show nearly identical values for the square, rectangular and hexagonal lattices, the non-Bravais lattices show different behavior. Here fields on different rows of antidots are different indicating complicated resulting spin wave spectra.

Figure 9.6 shows the simulated spin wave mode profiles[40] for the three Bravais-lattices studied here. The power and phase maps are shown for all modes while the color scales for both power and phase are shown at the bottom of the figure. The bias field is applied along the x-direction. It is clear from the figure that in square and rectangular lattices the modes are extended along y-direction giving rises to modes with different wave vectors q. On the other hand the modes along x-direction form standing waves due to confining potentials produced by the demagnetizing fields around the antidots. Hence, we assign quantization numbers n to these standing waves. For a square lattice modes 1, 2 and 3 correspond to $q = 0, \pi/2a$ and π/a, where a is the lattice constant of the square lattice. These correspond to Damon Eshbach (DE) modes at the centre, middle and the boundary of the first Brillouin Zone (BZ), respectively. On the other hand along x-direction these modes correspond to standing spin wave modes in the backward volume (BV) geometry with $n = 3$, 3 and 5. For the rectangular lattice the extended modes along the y-directions (DE-mode) correspond to $q = 0, \pi/2a'$ and π/a', where a' is the lattice constant of the rectangular lattice along y-direction. On the other hand the standing spin waves in the BV geometry correspond to quantization number $n = 3$, 5 and 7. In the case of hexagonal lattice no extended modes in the DE geometry are observed as the positions of the antidots along the y-direction cause unavailability of continuous channels of materials along y-direction unlike the square and rectangular lattices. Hence no q vector corresponding to DE-mode is assigned in this case and only BV-like standing spin wave modes and localized modes are observed. Mode 1 is a localized mode confined in the potential around the edges of the antidots, while modes 2 to 4 correspond to BV-like standing spin waves with $n = 3$, 5 and 7 similar to the rectangular lattice.

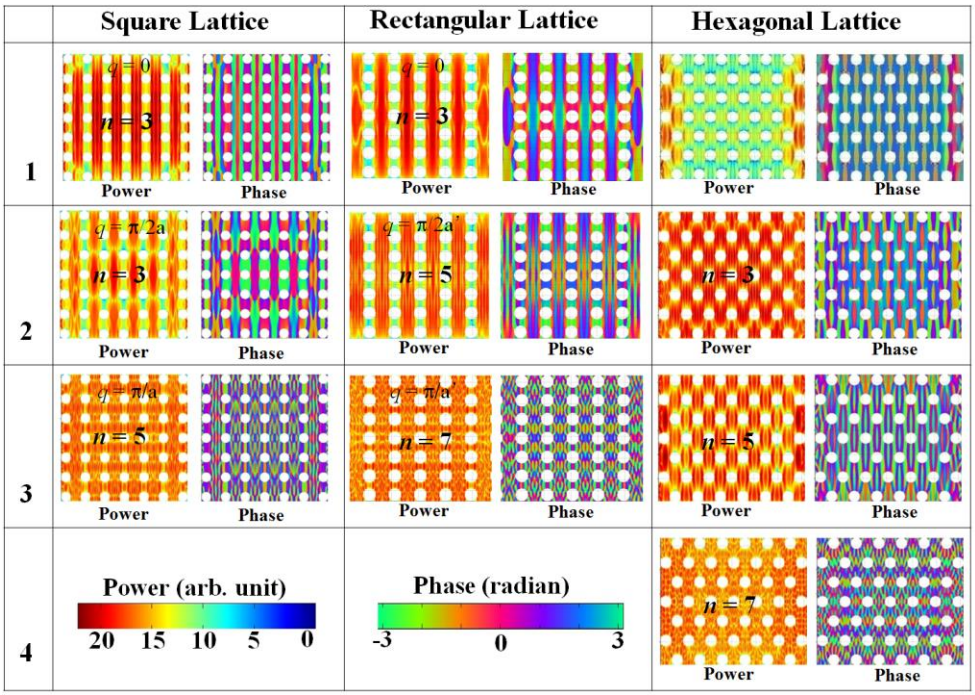

Figure 9.6: Simulated spin wave mode profiles (power and phase maps) for the $Ni_{80}Fe_{20}$ antidot lattices with square, rectangular and hexagonal lattice symmetry. The color scales for the power and phase maps are shown at the bottom of the figure.

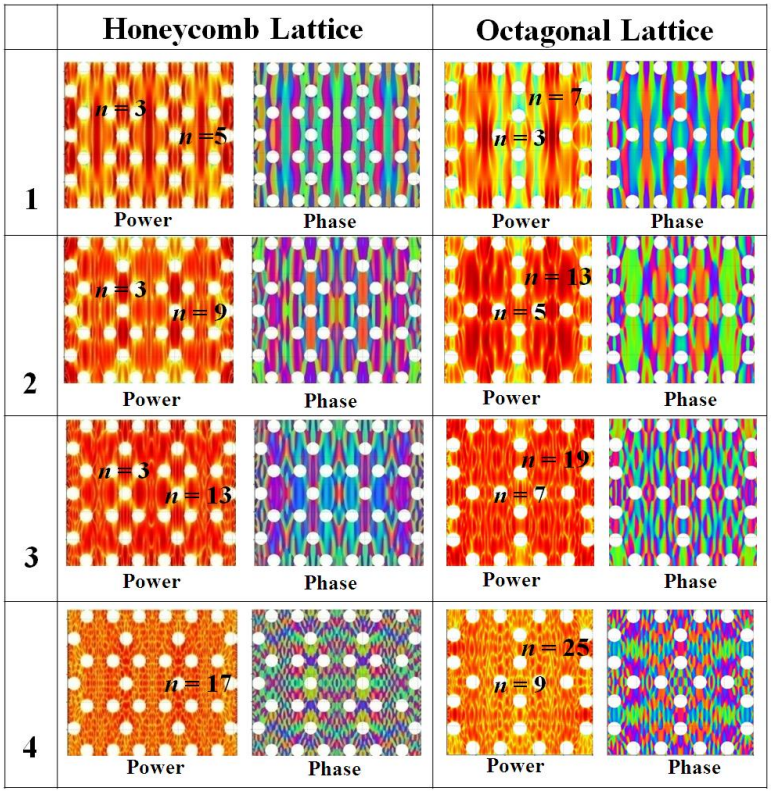

Figure 9.7: Simulated spin wave mode profiles (power and phase maps) for the $Ni_{80}Fe_{20}$ antidot lattices with honeycomb and octagonal lattice symmetry. The color scales for the power and phase maps are as shown in Figure. 9.6.

Figure 9.7 shows the simulated spin wave mode profiles for the two non-Bravais lattices. Here, the modes are more complicated and different standing spin waves in the BV geometry can be identified at two different locations inside the lattice, namely, a) inside the honeycomb (octagonal) units and between two such consecutive units. In case of honeycomb lattice the BV-like standing wave modes inside the honeycomb unit for modes 1, 2, 3 and 4 are found have n = 5, 9, 13 and 17, while the modes confined between two honeycomb units have n = 3 for modes 1, 2 and 3, while the same for mode 4 could not be identified. For the octagonal lattice the BV-like standing waves have n = 7, 13, 19 and 25 for modes 1, 2, 3 and 4 inside the octagonal unit. On the other hand the modes confined in between the octagonal units have n = 3, 5, 7 and 9 for modes 1, 2, 3 and 4. The observation of such a wide variety of extended, standing and localized spin wave modes in the antidot lattices and their tunability by varying lattice symmetry will enable the design of two-dimensional magnonic devices with a widely tunable magnonic band structures suitable for applications in a wide range of devices.

9.5 Summary

In summary, we have investigated the tunability in spin wave spectrum by varying lattice symmetry in two dimensional $Ni_{80}Fe_{20}$ antidot lattices. We used broadband ferromagnetic resonance spectroscopy to measure the spin wave spectra in those lattices by varying the bias magnetic field. A distinct difference in the number of modes, their frequency values, gaps between the modes and onset of mode splitting are observed with the variation of lattice symmetry. Simulated magnetostatic field profiles showed the variation of the internal demagnetized fields within the lattices leading towards the origin of the variation of the spin wave spectra. The simulated spin wave mode profiles for the square and rectangular lattices showed extended modes in the Damon-Eshbach (DE) geometry with different wave vectors originating at the centre, middle and boundary of the first Brillouin zone. On the other hand standing spin wave modes with varying mode quantization numbers are also observed in the backward volume (BV) geometry for those lattices. The hexagonal lattice showed a localized mode and three standing wave modes in BV geometry with varying mode quantization numbers distributed uniformly over the lattice. In contrary

the honeycomb and the octagonal lattices showed two different types of standing spin waves with varying mode quantization number in the BV geometry. One is confined within the honeycomb or octagonal unit and the other is confined between two such units. The observation of such wide variety of spin waves and their tunability by varying lattice symmetry opens up exciting new possibilities in two-dimensional magnonic devices.

Bibliography

[1] K. Kern, D. Heitmann, P. Grambow, Y. H. Zhang and K. Ploog, *Phys. Rev. Lett.* **66**, 1618 (1991).

[2] G. Ctistis, E. Papaioannou, P. Patoka, J. Gutek, P. Fumagalli and M. Giersig, *Nano Lett.* **9**, 1 (2009).

[3] L. Torres, L. Lopez-Diaz and O. Alejos, *J. Appl. Phys.* **87**, 5645 (2000).

[4] K.-S. Lee, D.-S. Han and S.-K. Kim, *Phys. Rev. Lett.* **102**, 127202 (2009).

[5] J. W. Kłos, D. Kumar, M. Krawczyk and A. Barman, *Sci. Rep.* **3**, 2444 (2013).

[6] S.-K. Kim, K.-S. Lee and D.-S. Han, *Appl. Phys. Lett.* **95**, 082507 (2009).

[7] E. K. Semenova and D. V. Berkov, *J. Appl. Phys.* **114**, 013905 (2013).

[8] S. K. Choi, K. S. Lee and S. K. Kim, *Appl. Phys. Lett.* **89**, 062501 (2006).

[9] J. Podbielski, F. Giesen and D. Grundler, *Phys. Rev. Lett.* **96**, 167207 (2006).

[10] Y. Au, M. Dvornik, O. Dmytriiev and V. V. Kruglyak, *Appl. Phys. Lett.* **100**, 172408 (2012).

[11] T. Schneider, A. A. Serga, B. Leven, B. Hillebrands, R. L. Stamps and M. P. Kostylev, *Appl. Phys. Lett.* **92**, 022505 (2008).

[12] S. Nikitov, P. Tailhades and C. Tsai, *J. Magn. Magn. Mater.* **236**, 320 (2001).

[13] V. V. Kruglyak, S. O. Demokritov and D. Grundler, *J. Phys. D: Appl. Phys.* **43**, 264001 (2010).

[14] B. Lenk, H. Ulrichs, F. Garbs and M. Münzenberg, *Phys. Rep.* **507**, 107 (2011).

[15] S. O. Demokritov and A. N. Slavin, "Magnonics: From Fundamentals to Applications," *Springer*, (2013).

[16] S. McPhail, C. Gürtler, J. Shilton, N. Curson and J. Bland, *Phys. Rev. B* **72**, 094414 (2005).

[17] O. Martyanov, V. Yudanov, R. Lee, S. Nepijko, H. Elmers, R. Hertel, C. Schneider and G. Schönhense, *Phys. Rev. B* **75**, 174429 (2007).

[18] S. Neusser, B. Botters and D. Grundler, *Phys. Rev. B* **78**, 054406 (2008).

[19] S. Neusser, B. Botters, M. Becherer, D. Schmitt-Landsiedel and D. Grundler, *Appl. Phys. Lett.* **93**, 122501 (2008).

[20] M. Kostylev, G. Gubbiotti, G. Carlotti, G. Socino, S. Tacchi, C. Wang, N. Singh, A. O. Adeyeye and R. L. Stamps, *J. Appl. Phys.* **103**, 07C507 (2008).

[21] S. Neusser, G. Duerr, H. Bauer, S. Tacchi, M. Madami, G. Woltersdorf, G. Gubbiotti, C. Back and D. Grundler, *Phys. Rev. Lett.* **105**, 067208 (2010).

[22] S. Tacchi, M. Madami, G. Gubbiotti, G. Carlotti, A. O. Adeyeye, S. Neusser, B. Botters and D. Grundler, *IEEE Trans. Magn.* **46**, 172 (2010).

[23] S. Tacchi, M. Madami, G. Gubbiotti, G. Carlotti, A. O. Adeyeye, S. Neusser, B. Botters and D. Grundler, *IEEE Trans. Magn.* **46**, 1440 (2010).

[24] H. Ulrichs, B. Lenk and M. Münzenberg, *Appl. Phys. Lett.* **97**, 092506 (2010).

[25] J. Ding, D. Tripathy and A. O. Adeyeye, *J. Appl. Phys.* **109**, 07D304 (2011).

[26] G. Duerr, M. Madami, S. Neusser, S. Tacchi, G. Gubbiotti, G. Carlotti and D. Grundler, *Appl. Phys. Lett.* **99**, 202502 (2011).

[27] S. Neusser, H. G. Bauer, G. Duerr, R. Huber, S. Mamica, G. Woltersdorf, M. Krawczyk, C. H. Back and D. Grundler, *Phys. Rev. B* **84**, 184411 (2011).

[28] S. Neusser, G. Duerr, S. Tacchi, M. Madami, M. Sokolovskyy, G. Gubbiotti, M. Krawczyk and D. Grundler, *Phys. Rev. B* **84**, 094454 (2011).

[29] R. Bali, M. Kostylev, D. Tripathy, A. O. Adeyeye and S. Samarin, *Phys. Rev. B* **85**, 104414 (2012).

[30] R. Mandal, S. Saha, D. Kumar, S. Barman, S. Pal, K. Das, A. K. Raychaudhuri, Y. Fukuma, Y. Otani and A. Barman, *ACS Nano* **6**, 3397 (2012).

[31] S. Tacchi, B. Botters, M. Madami, J. W. Klos, M. Sokolovskyy, M. Krawczyk, G. Gubbiotti, G. Carlotti, A. O. Adeyeye, S. Neusser and D. Grundler, *Phys. Rev. B* **86**, 014417 (2012).

[32] R. Zivieri, S. Tacchi, F. Montoncello, L. Giovannini, F. Nizzoli, M. Madami, G. Gubbiotti, G. Carlotti, S. Neusser, G. Duerr and D. Grundler, *Phys. Rev. B* **85**, 012403 (2012).

[33] T. Schwarze, R. Huber, G. Duerr and D. Grundler, *Phys. Rev. B* **85**, 134448 (2012).

[34] J. Ding, D. Tripathy and A. O. Adeyeye, *Europhys. Lett.* **98**, 16004 (2012).

[35] R. Mandal, P. Laha, K. Das, S. Saha, S. Barman, A. K. Raychaudhuri and A. Barman, *Appl. Phys. Lett.* **103**, 262410 (2013).

[36] D. Kumar, P. Sabareesan, W. Wang, H. Fangohr and A. Barman, *J. Appl. Phys.* **114**, 023910 (2012).

[37] A. Barman, *J. Phys. D: Appl. Phys.* **43**, 195002 (2010).

[38] B. K. Mahato, S. Choudhury, R. Mandal, S. Barman, Y. Otani and A. Barman, *J. App. Phys.* **117**, 21390 (2015).

[39] M. Donahue and D. G. Porter, "OOMMF User's guide, Version 1.0," *NIST Interagency Report Number 6376, National Institute of Standard and Technology, Gaithersburg, MD, URL:* http://math.nist.gov/oommf, City (1999).

[40] D. Kumar, O. Dmytriiev, S. Ponraj and A. Barman, *J. Phys. D: Appl. Phys.* **45**, 015001 (2012).

Chapter 10

Summary and Future Perspectives

10.1 Summary

In this thesis, we have investigated the static and dynamic magnetic properties of two-dimensional magnonic crystals in the form of arrays of antidot lattices. Antidot lattice is a promising candidate of two-dimensional magnonic crystals due to their steeper frequency vs. wave vector dispersion and larger propagation velocities, which allows the tenability of magnonic band gaps more efficiently. The static magnetic properties have been studied by static magneto-optical Kerr effect (SMOKE) measurements. On the other side, we have measured the time-domain ultrafast magnetization dynamics by our home-built all-optical time-resolved magneto-optical Kerr effect (TRMOKE) microscope. The magnetization dynamics in frequency domain have been measured by using a broadband ferromagnetic resonance spectrometer based on a vector network analyzer (VNA-FMR). All the experimental results have been analyzed and interpreted with the aid of finite difference method based micromagnetic simulations.

We have fabricated continuous and microscale blanket Co and $Ni_{80}Fe_{20}$ thin films with different dimensions by optical lithography and e-beam evaporation methods and characterized them by various routine characterization methods. The blanket films are found to be of good quality with small amount of rounded corners and edge roughness and deformations. However, due to their very small thickness/width ratio, the edge demagnetization effects are very small in these samples and would not affect the static and dynamic magnetic properties of the overall sample. In addition, the time-resolved magnetization dynamics is measured by a focused laser spot of much smaller size placed at the centre of the blanket film and hence edge effect would be negligible. The static magnetic characterization by VSM and static MOKE techniques gave some initial ideas about the magnetic properties of the samples. The magnetization dynamics of the blanket films have been measured by time-resolved MOKE and broadband ferromagnetic resonance spectrometers. A single resonant mode corresponding to the uniform precessional dynamics is observed in all cases. The variations of precession frequencies with bias magnetic field are modelled by Kittel

formula and the magnetic parameters are extracted. Those blanket films have been used for patterning the arrays of antidots. We have further investigated the variation in magnetization dynamics of the antidot arrays by changing various physical and material parameters as well as the strength and orientations of the bias magnetic field.

First, we fabricated high quality square arrays of antidot lattice structures by using focused ion beam lithography on square shaped 10 µm × 10 µm blanket Co thin films. The antidots have diameters of 100 nm and have varying lattice constants from 200 nm to 500 nm. The antidot structures are generally well fabricated with small deviations in the antidot diameters and lattice constants. We have excited and detected the magnetization dynamics in those antidot lattice structures by an all-optical time-resolved Kerr microscope. The dynamics shows two prominent magnonic bands for sparsely packed antidot lattices with a clear bandgap. The bandgap increases with the decrease in the lattice constant and at the lowest value of the lattice constant four distinct magnonic bands appear. Micromagnetic simulations qualitatively reproduce the observations and the mode profiles of the resonant modes are calculated and interpreted. We further demonstrate the tunability of magnonic spectra in composite antidot structures with varying geometry. These observations are important for potential applications of the antidot lattices in nanoscale magnonic crystals in the form of composite antidot structures with tunable bandgap.

Further, we have investigated the effects of the shape of the antidots on the spin waves in $Ni_{80}Fe_{20}$ antidot lattices. Significant differences in the spin wave spectra are observed with the variation in the antidot shape. We have fabricated four different shapes (circle, square, triangle and diamond) of antidots for this study. Two prominent modes with significant gaps in the spin wave spectra for the circular and square shaped antidots change into three and four closely spaced modes with narrow gaps for the triangular and diamond shaped antidot lattices, respectively. In addition, when the bias field is rotated within the sample plane by $\varphi = 45°$ from the horizontal or vertical edges of the lattices a single dominant mode is observed for three lattices except for the square shaped antidot lattice, where an additional low amplitude mode occurs at lower frequency. Micromagnetic simulations helped to identify the spin wave modes. While for the circular and square antidot lattices the higher frequency mode is a quantized mode in the BWVMS geometry with mode number $q = 5$, the lower frequency mode is an extended DE mode. In the triangular and diamond shaped

lattices an additional quantized mode with q = 3 appeared in the frequency gap observed in the other two lattices. For the diamond shaped lattice another modified DE-like mode appears at frequency below the Damon-Eshbach (DE) mode. At φ = 45° the extended DE mode disappears for the circular, triangular and diamond shaped antidot lattices and its power is reduced significantly in the square antidot lattice, while a mode localized in the region between the next nearest antidots in a direction perpendicular to the bias field becomes dominant. The observed tunability of the spin wave spectrum with the antidot shape and the bias field orientation may give rise to an enabling tool for tuning the frequency of such devices when they are used as magnonic filters, splitters and other magnonic devices.

Finally, we investigated the tunability in spin wave spectrum by varying lattice symmetry in two-dimensional $Ni_{80}Fe_{20}$ antidot lattices. For this study we used broadband ferromagnetic resonance spectroscopy to measure the spin wave spectra in those lattices by varying the bias magnetic field. An array of circular shaped antidots with 300 nm in diameter and inter-antidot separation of 330 nm between nearest neighbours arranged in square, rectangular, hexagonal, honeycomb and octagonal lattice were fabricated by using electron beam lithography and ion milling. A distinct difference in the number of modes, their frequency values, and gaps between the modes and onset of mode splitting are observed with the variation of lattice symmetry. Simulated magnetostatic field profiles showed the variation of the internal demagnetized fields within the lattices leading towards the origin of the variation of the spin wave spectra. The simulated spin wave mode profiles for the square and rectangular lattices showed extended modes in the Damon-Eshbach (DE) geometry with different wave vectors originating at the centre, middle and boundary of the first Brillouin zone. On the other hand, standing spin wave modes with varying mode quantization numbers are also observed in the backward volume (BV) geometry for those lattices. The hexagonal lattice showed a localized mode and three standing wave modes in BV geometry with varying mode quantization numbers distributed uniformly over the lattice. In contrary, the honeycomb and the octagonal lattices showed two different types of standing spin waves with varying mode quantization numbers in the BV geometry. One is confined within the honeycomb or octagonal unit and the other is confined between two such units. The observation of such wide variety of spin waves and their tunability by varying lattice symmetry opens up

exciting new possibilities in two-dimensional magnonic devices.

10.2 Future Perspectives

Ferromagnetic antidot lattices have already established themselves as a strong candidate for two-dimensional magnonic crystals. A number of important works have been done on this system, both in theoretical and experimental fronts, including those presented in this thesis. Those revealed a wealth of new information, which are essential for further progress of this field towards establishing them in magnonic and spintronic devices. However, more extensive studies are still necessary before drawing a concrete conclusion on this system.

An immediate extension of the works presented in this thesis is an extensive study of magnonic band structure (frequency vs. wave vector dispersion) using Brillouin light scattering study. Establishment of partial and complete band gaps at Briilouin zone boundaries and inside the Brillouin zone and along all symmetry axes of the lattices with varying antidot shape, size, lattice constant and lattice symmetry is necessary. Especially, hexagonal, honeycomb and octagonal lattices can reveal rich band structures with a number of band gaps.

Anisotropy of spin wave propagation is an important topic for their applications in spin wave filters, attenuators and splitters. The study of anisotropy in the nature and frequency of the spin waves may reveal very interesting properties in antidot lattices with varying antidot shapes and lattice symmetry. A thorough study towards that direction both for zero and finite wave vectors are necessary.

A large number of studies have already been done on in-plane magnetized two-dimensional antidot lattices. However, out-of-plane magnetized antidot lattices are seldom studied. Very few studies already pointed towards larger stability of spin waves in out-of-plane magnetized ferromagnetic antidot lattices. An extensive study of two-dimensional antidot lattices in ferromagnetic single and multilayered thin film materials including CoFeB, FePt, CoPd, CoPt, CoCrPt alloys and Co/Pt, Co/Pd, Co/Ni, Fe/Pt mulilayers would be important. Further, antidot lattices with exchange bias can also induce additional unidirectional anisotropy in these lattices, which may

superpose with shape anisotropy of the antidots and can reveal interesting spin wave properties.

Another important aspect is to study quasiperiodic and defective structures. Very few attempts have been made so far to develop and investigate fractal structures. Some regular fractal structures can be immediately studied to understand how the fractals lead to the quantization of spin waves. In addition, antidot quasicrystals would also be a hugely interesting system. Various generations of penrose tilings using antidots may lead to interesting new properties. The existence of long range magnetic orders but the lack of translational periodicity may lead to stochastic switching and spin wave quantization in a global field. Defect is another important aspect in two-dimensional magnonic crystals. These defects can be of two types, namely a) tailored defects and b) natural defects. While natural defects can occur due to the limitation of fabrication techniques, they need to be characterized extensively. Edge roughness and deformation can lead to undesired pinning around the antidot edges. Whereas ion implantation during focused ion beam milling may lead to a modification of the magnetic properties around the antidot edges leading towards localization of spin waves in those defect potentials. Tunneling of such localized spin waves in the unaffected material may lead to interesting interaction of modes and lead to mode mixing. On the other hand, tailored defects such as artificially created vacancies or antidots with different sizes and shapes can lead to creation of donor and acceptor type defect states in the magnonic band structures. A control of these defect states may lead towards a variation of transmission coefficients of the magnons through such structures. Reprogrammable spin wave devices based on such defect states can also be developed.

Development of richer magnonic metamaterials based on two dimensional antidot arrays is an important proposition. To that end, introduction of diatomic basis structures of different antidot sizes and shapes can play important role. Development of bi-component magnonic crystals in the form of filled antidot lattices is already explored but there are still a lot of scopes in that field where different material combination may lead to a broader tunability of band gap properties.

Finally, fabrication and characterization of magnonic devices based on the knowledge gained and database created on this topic would be important. Magnetic antidot

waveguides have received theoretical attentions and a number of important results can be found in literature. However, no conclusive experimental works have been reported so far. Development of this field would be important. Improvement of fabrication methods towards development of antidot structures in the deep sub-100nm scale would lead towards exploring the higher frequency dipole-exchange spin wave regime with better prospects of devices.